University of Trento
Department of Physics

Thesis submitted to the
Doctoral School in Physics – XXVIII cycle
by

Simone Donadello

for the degree of

Doctor of Philosophy – Dottore di Ricerca

Observation of the Kibble–Zurek mechanism in a bosonic gas

Supervisor: Gabriele Ferrari

Trento – Italy

April 2016

Simone Donadello

Observation of the Kibble–Zurek mechanism in a bosonic gas

Ph.D. Thesis in Physics

University of Trento
April 2016

A chi c'è sempre stato,
a chi ho perso e a chi ho trovato

ABSTRACT

When a second-order phase transition is crossed at finite speed, domains with independent order parameters can appear in the system, with the consequent formation of defects at the domain boundaries. The Kibble–Zurek theory provides a description for this universal phenomenon, which applies to many different systems in nature, and it predicts a power-law dependence of the defect density on the quench rate. This thesis reports on the results of the experimental study of the Kibble–Zurek mechanism in elongated Bose–Einstein condensates of atomic sodium gases, following the observations on the spontaneous formation of defects after temperature quenches across the BEC transition. The power-law scaling of the defect number with the quench speed was observed and characterized for the first time in ultracold gases. The characterization of the density and phase profiles of the defects allowed their identification as solitonic vortices, representing the first direct experimental evidence for this kind of long living excitation, which sets a link between solitons and vortices. The measurements reported in this thesis provide a novel approach to the study of the critical phenomena happening at phase transitions, and introduce to the possibility of exploring the turbulent dynamics of quenched systems through the spontaneous production of solitonic vortices.

CONTENTS

ACRONYMS

1D one-dimensional

2D two-dimensional

3D three-dimensional

AOM acousto-optic modulator

BEC Bose–Einstein condensate

CCD charge-coupled device

DAC digital-to-analog converter

DDS direct digital synthesizer

ECDL external-cavity diode laser

EOM electro-optic modulator

FFT fast Fourier transform

FPGA field-programmable gate array

GPE Gross–Pitaevskii equation

GUI graphical user interface

HF high frequency

HV high vacuum

IGBT insulated-gate bipolar transistor

KZ Kibble–Zurek

KZM Kibble–Zurek mechanism

LUT lookup table

MOT magneto-optical trap

MT magnetic trap

RF radio frequency

SV solitonic vortex

TOF time of flight

TTL transistor-transistor logic

UHF ultra-high frequency

UHV ultra-high vacuum

USB Universal Serial Bus

ZS Zeeman slower

INTRODUCTION

Second-order phase transitions are ubiquitous phenomena in nature, and are intrinsically linked with the universal laws of physics. They occur with continuous changes of the fundamental properties of systems, whose description can be made in terms of transformations from disordered phases to ordered ones. Below the transition point of a second-order phase transition the system can be described by means of an order parameter, whose phase is randomly chosen through spontaneous symmetry breaking. The fact that the order parameter becomes finite in the whole system at the transition crossing reflects in long-range fluctuations characterized by a divergence of the correlation length, hence demonstrating the criticality of the system at the phase transition. The study of second-order phase transitions acquires a fundamental importance in many fields of physics, since the description of the singularities in many thermodynamic quantities at the critical point can be done in terms of universal power laws and critical exponents, which are common to different systems sharing the same universality class.

Analogously to the correlation length, the relaxation time diverges at the transition. This implies that, when the critical point is crossed at a finite rate, the transition happens in a nonadiabatic regime, and consequently the dynamical properties of the system freeze in an interval around the transition point. This, in combination with the causality principle that sets the limit for the velocity at which information can travel in the system, can lead to the formation of independent phase domains, reflecting the local choice of the phase of the order parameter. Then, when the system relaxes and the phase domains merge, defects can appear at the domain boundaries. A model of this universal phenomenon is provided by the Kibble–Zurek theory (Kibble, 1976; Zurek, 1985), which was initially introduced in the context of cosmology, but subsequently generalized to systems quenched across a generic second-order phase transition.

The Kibble–Zurek theory provides quantitative predictions for the defect number scaling with the quench speed (del Campo et al., 2014), whose measurement is particularly intriguing since it represents an experimentally accessible way to test the universal theories on phase transitions and critical exponents. The results of the Kibble–Zurek theory apply both to homogeneous and inhomogeneous systems (del Campo et al., 2013), and both to classical and quantum phase transitions (Zurek et al., 2005). So far experimental evidences of the Kibble–Zurek mechanism were reported in experiments with many different systems, such as superfluid helium-3 (Bäuerle et al., 1996; Ruutu et

al., 1996), nonlinear optical systems (Ducci et al., 1999), thin-film superconductors (Carmi et al., 1999; Kirtley et al., 2003), annular Josephson junctions (Carmi et al., 2000; Monaco et al., 2006), ferromagnetic spinor BECs (Sadler et al., 2006), multiferroic crystals (Chae et al., 2012), atomic Mott insulators (Chen et al., 2011; Braun et al., 2015), and ion chains (Pyka et al., 2013; Ulm et al., 2013).

Other systems which were predicted to be ideal for the study of the Kibble–Zurek mechanism are ultracold gases undergoing Bose–Einstein condensation (Kibble, 2007; Zurek, 2009; del Campo et al., 2011). In fact experiments with dilute atomic gases are typically performed in clean environments, with a high control over the experimental parameters at the transition. Moreover Bose–Einstein condensates support different kinds of phase defects, such as solitons and vortices, which can be directly detected with imaging techniques. Within this framework, the spontaneous formation of vortices after fast temperature quenches was already observed in oblate condensates (Weiler et al., 2008), but the defect number scaling versus the quench time was never reported before using atomic gases.

In this thesis I present the most important results obtained during my doctorate at the laboratory of ultracold gases of the University of Trento, mainly related to the study of the spontaneous formation of defects in elongated Bose–Einstein condensates of sodium. In our inhomogeneous system we have characterized the defect number at different quench speeds, measuring a power-law scaling as predicted by the Kibble–Zurek mechanism. This measurement, the first one in ultracold gases, was performed by varying the evaporation cooling rate over a wide interval, and by directly observing the defects with absorption imaging after long ballistic expansion. Our results confirm that atomic Bose–Einstein condensates represent a powerful testbed for exploring the critical phenomena occurring at phase transitions, and they inspired other intriguing studies on the Kibble–Zurek mechanism, such as recent experiments with three-dimensional (Navon et al., 2015) and quasi-two-dimensional homogeneous systems (Chomaz et al., 2015).

The thesis is organized as follows.

- In the *first chapter* I will introduce the main results of the Kibble–Zurek theory, in particular regarding the predictions about the defect number scaling with the quench parameters. I will also provide a theoretical background for the phase transition that is object of study in our case, which is Bose–Einstein condensation.

- In the *second chapter* I will describe our experimental apparatus for the production of Bose–Einstein condensates of sodium that I contributed to build, as well as the techniques for the real-

ization of the experiments presented in the following chapters (Lamporesi et al., 2013a).

- In the *third chapter* I will present the results of our first observations on the spontaneous formation of defects in condensates after fast temperature quenches (Lamporesi et al., 2013b). The measurement of a power-law scaling for the defect number as a function of the quench speed represents one of the first tests for the Kibble–Zurek mechanism in ultracold gases.

- In the *fourth chapter* I will present the experimental and numerical characterization of the long living defects forming in our system, which allowed their identification as solitonic vortices (Donadello et al., 2014; Tylutki et al., 2015). These represent the first direct observations of solitonic vortices in Bose–Einstein condensates, the defects which set a link between vortices and solitons in elongated systems.

- Finally, in the *fifth chapter* I will present the additional measurements of the defect number scaling that we performed with the aim of studying the Kibble–Zurek mechanism in different confinement regimes. I will also discuss the role of the post-quench dynamics of defects, as suggested by the observation of different evolution paths for solitonic vortices (Serafini et al., 2015). The latter may play a key role to determine the departure from a simple power-law scaling as we observe for very fast quenches.

1 THEORETICAL BACKGROUND

Phase transitions are intriguing phenomena of nature, occurring with important transformations in the properties of physical systems. In section 1.1 I will introduce the particular class of continuous phase transitions. In general an adiabatic description of the system is not valid if this kind of transition is crossed at a finite speed: independent phase domains can form in the system, with the possible consequent creation of topological defects. A universal treatment of this phenomenon is given within the Kibble–Zurek theory, whose predictions will be presented in section 1.2.

A phase transition which is ideal for the study of the Kibble–Zurek mechanism is Bose–Einstein condensation in dilute atomic gases. This phenomenon, whose main characteristics will be discussed in section 1.3, leads to a fascinating state of matter where quantum mechanics manifests itself on a macroscopic scale, and where phase defects can take different forms such as solitons or quantized vortices.

1.1 CONTINUOUS PHASE TRANSITIONS

A *phase transition* is the transformation of the equilibrium state of a system from one phase to another, occurring with significant changes in several of its physical properties. Phase transitions can be divided into two classes, depending on the thermodynamic characteristics of the considered system during the transformation (Huang, 1987).

FIRST ORDER A transition is of *first order* when it shows a discontinuity for one of the first partial derivatives of the Gibbs free energy. A typical example is the transition from liquid to gas phases, where the discontinuity is manifested as latent heat.

SECOND ORDER A transition is of *second order*, also called *continuous*, when all the first partial derivatives of the free energy are continuous during the transition. Examples are the paramagnetic to ferromagnetic and the normal to superfluid transitions. A particular subset of this class of phenomena, not considered here, are the infinite-order phase transitions, such as the BKT transition (Berezinskii, 1971; Kosterlitz et al., 1973).

In this discussion we focus on continuous phase transitions, where the transformation is driven by the variation of a thermodynamic variable, called *control parameter*, through a particular value, called

critical point. Let us consider as an example the ferromagnetic transition, where the control parameter is the temperature T and the critical point is the Curie temperature T_c. Above T_c there is no net magnetization in the system, which therefore results to be magnetically isotropic. On the contrary, at low temperatures spontaneous magnetization occurs: the original symmetry is broken, since a preferred direction, given by the magnetization vector, is chosen.

An additional parameter, called *order parameter*, can be introduced in order to describe the state with lower symmetry below the critical point. The order parameter is zero in the symmetric state above the transition, while it takes a finite value in the ordered state. Concerning the example of the ferromagnetic transition, the natural choice for the order parameter is the magnetization, which represents a measure of the magnetic order of the system.

Statistical fluctuations of the order parameter play a key role in second-order phase transitions. Even if for quantum transitions these fluctuations can be present also at zero temperature, here we focus on classical transitions occurring at finite temperature and characterized by thermal fluctuations. The length scale over which such fluctuations are correlated is called *correlation length*, labeled with ξ. At the transition the correlation length diverges, reflecting the fact that below the critical point the order parameter becomes finite and homogeneous in the whole system. Considering the example of the ferromagnetic transition, the behavior of the correlation length at the critical temperature is described by a power-law scaling as follows:

$$\xi \sim |T - T_c|^{-\nu} . \tag{1.1}$$

The divergence of ξ corresponds to singularities in other thermodynamic quantities, such as the specific heat C, the magnetization* M, and the susceptibility χ of the ferromagnet:

$$C \sim |T - T_c|^{-\alpha} \tag{1.2}$$

$$M \sim |T - T_c|^{\beta} \tag{1.3}$$

$$\chi \sim |T - T_c|^{-\gamma} . \tag{1.4}$$

This description can be generalized to other second-order phase transitions, and the exponents $\alpha, \beta, \gamma, \ldots$ of the power laws describing the singular thermodynamic properties at the transition point are called *critical exponents*. It must be noted that the critical value of the control parameter T_c depends on the properties of the specific system, whereas the critical exponents are determined only by the universality class of the transition, not by the microscopic details. Continuous phase transitions sharing the same universality class are described by equal scaling laws, even in very different kinds of systems.

* Note that the magnetization, i. e., the order parameter of the ferromagnetic transition, follows a power-law scaling for $T - T_c \to 0^-$, while for $T > T_c$ it is zero by definition.

So far we considered a stationary system: the transition occurs adiabatically, and the system is point-by-point at its equilibrium while varying the control parameter. However this adiabatic description is not realistic in experiments, where the transition is crossed changing the control parameter at a finite speed. In order to describe the dynamical properties of the system, one can introduce another characteristic quantity called *relaxation time*, which sets the timescale for the relaxation of the order parameter to its equilibrium value. Similarly to the correlation length, the relaxation time τ scales with the control parameter as a power law, diverging at the critical point of a second-order phase transition:

$$\tau \sim |T - T_c|^{-z\nu} . \tag{1.5}$$

As a result of the *critical slowing down*, i. e., the divergence of the relaxation time, phase transitions in experiments are always crossed in a nonadiabatic regime. Moreover it must be considered that the information about the choice of the order parameter cannot propagate faster than the limit imposed by the causality principle, which is a characteristic velocity of the specific system. Thus at the symmetry breaking the order parameter can take different random values in different regions of the system. As sketched in figure 1.1, this may cause the formation of independent phase domains, whose typical size is related to the correlation length near the transition. Topological defects may consequently form at the domain boundaries after the transition has been crossed, as a consequence of the merging of the different phases at the system relaxation.

The mechanism that we just introduced was discussed by Tom W. B. Kibble for a cosmological problem related to the theories for the unification of fundamental interactions, predicting an original symmetry between those interactions at very high energies. In particular Kibble proposed a description for the spontaneous symmetry breaking that might have occurred during the fast expansion and cooling of the universe after the Big Bang, leading to the formation of cosmic anisotropies (Kibble, 1976).

The idea of Kibble was subsequently extended by Wojciech H. Zurek to second-order phase transitions in condensed matter systems, providing an important background for testing the theories for critical phenomena on systems which are experimentally accessible (Zurek, 1985). This general description is usually referred as the *Kibble–Zurek mechanism* (KZM). It predicts the formation of smaller phase domains for faster quenches across the phase transition, and it describes the scaling with the quench speed of the number of phase defects formed after the transition crossing by means of simple analytical relations. The most important results of the Kibble–Zurek (KZ) theory will be presented in the next section.

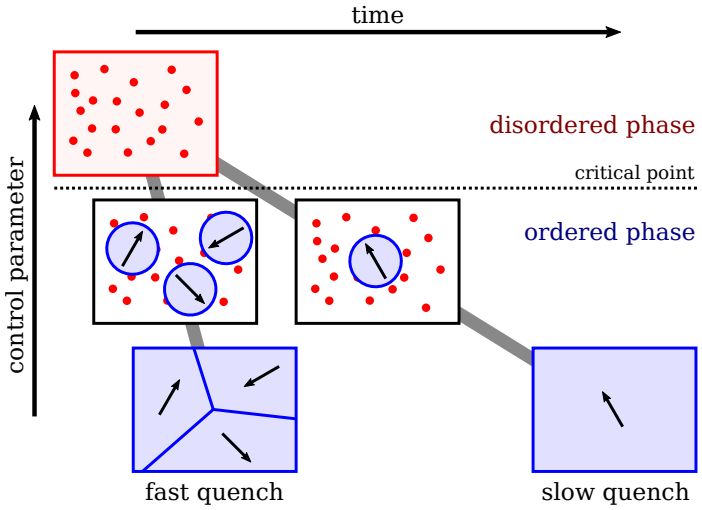

Figure 1.1: In this picture of a continuous phase transition the initial condition is a system above the transition point. When the control parameter is reduced below its critical value, spontaneous symmetry breaking causes the order parameter to pick finite random values, represented with arrows. Due to causality and to divergence of the relaxation time, for fast quenches different regions of the system can choose different values of the order parameter, hence forming independent phase domains.

1.2 KIBBLE–ZUREK MECHANISM

1.2.1 Homogeneous KZM

The KZM focuses on the spontaneous symmetry breaking occurring at the critical value λ_c of a generic control parameter λ while driving a continuous phase transition in a homogeneous system, starting from $\lambda > \lambda_c$. Following the review of del Campo et al. (2014), we can define the *reduced control parameter* as

$$\varepsilon = \frac{\lambda_c - \lambda}{\lambda_c}, \tag{1.6}$$

a dimensionless variable which is zero at the critical point.

As introduced while discussing equations (1.1) and (1.5), a second-order phase transition is characterized by the power-law divergence† in the equilibrium correlation length ξ and the equilibrium relaxation time τ, defined as

$$\xi(\varepsilon) = \frac{\xi_0}{|\varepsilon|^{\nu}} \tag{1.7}$$

$$\tau(\varepsilon) = \frac{\tau_0}{|\varepsilon|^{z\nu}}. \tag{1.8}$$

† The results of the KZ theory do not fully apply to specific cases where the relaxation time of the system does not scale as a power law with the control parameter. As an example, the infinite-order Berezinskii–Kosterlitz–Thouless transition needs a revised description for the KZM (Jelić et al., 2011; Dziarmaga et al., 2014).

Here ν and z are respectively the correlation and the dynamic critical exponents, which depend only on the universality class of the transition, while ξ_0 and τ_0 are constants determined by the microscopic properties of the specific system. From these quantities one can estimate the characteristic speed of perturbations of the order parameter in the system as

$$v = \frac{\xi}{\tau} = \frac{\xi_0}{\tau_0}|\varepsilon|^{\nu(z-1)} . \tag{1.9}$$

The phase transition is generally crossed at a variable rate, defined by the speed of the control parameter $\dot{\varepsilon}$, the *quench rate*. If we consider a quench that is *linear* in time, we can express the control parameter around the critical point at $t = 0$ as

$$\lambda(t) = \lambda_c\big(1 - \varepsilon(t)\big) , \tag{1.10}$$

where the reduced parameter becomes

$$\varepsilon(t) = \frac{t}{\tau_Q} \tag{1.11}$$

for $-\tau_Q < t < \tau_Q$, defining the *quench time* as

$$\tau_Q = \frac{1}{\dot{\varepsilon}} . \tag{1.12}$$

Therefore the quench time is the parameter characterizing the speed of the transition and one of the relevant timescales for the KZM.

Following its definition, given in equation (1.8), the relaxation time τ diverges at the critical point in $t = 0$. Starting from a high-symmetry state, i. e., when $t \ll 0$ and τ is small, the spontaneous symmetry breaking occurs while driving the system to cross the transition. Close to the critical point the relaxation time increases: due to the critical slowing down the dynamics of the transition freezes and the system is no longer able to follow the variation of the control parameter. The dynamics becomes adiabatic again for $t \gg 0$.

Within the approximation introduced by the KZM, the crossing of a continuous transition is described by the presence of three distinct regimes, as illustrated in figure 1.2. The *frozen regime* is the one during which the relaxation time τ is larger than the time distance from the transition point, expressed as $|\varepsilon/\dot{\varepsilon}|$. The time for which the distance from the transition equals the relaxation time is called *freeze-out time* and labeled with $\hat{t}$:

$$\tau(\hat{t}) \sim \left|\frac{\varepsilon(\hat{t})}{\dot{\varepsilon}(\hat{t})}\right| . \tag{1.13}$$

The system is considered frozen for $|t| < \hat{t}$, adiabatic elsewhere.

Introducing $\hat{\varepsilon} = \varepsilon(\hat{t})$, the relaxation time at the freeze-out can be expressed as

$$\hat{\tau} = \tau(\hat{\varepsilon}) = \frac{\tau_0}{|\hat{\varepsilon}|^{\nu z}} = \frac{\tau_0 \tau_Q^{\nu z}}{|\hat{t}|^{\nu z}} . \tag{1.14}$$

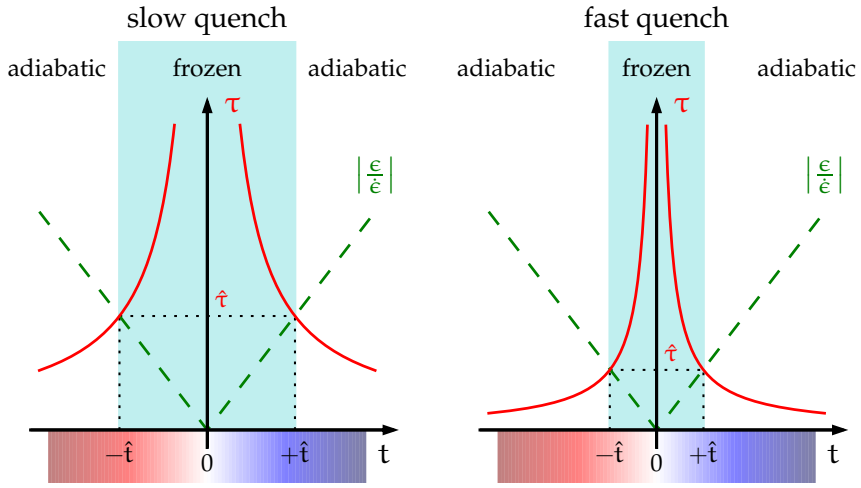

Figure 1.2: Schematic representation of the timescales around the transition at $t = 0$, where the relaxation time τ (red) diverges. In the KZ theory the crossing between the adiabatic-frozen-adiabatic regimes is approximated by the freeze-out time $\hat{t}$, corresponding to the instant where τ equals the time distance from the transition (green). For a slow quench (left) the interval around the critical point where the dynamics is frozen is wider compared to the case a fast quench (right).

From the definition $\hat{\tau} = \hat{t}$, the freeze-out time results to depend on the critical exponents ν and z, the quench time τ_Q, and the characteristic relaxation time τ_0 introduced in equation (1.8):

$$\hat{t} \sim \left(\tau_0 \tau_Q^{z\nu}\right)^{\frac{1}{1+z\nu}} . \tag{1.15}$$

As a consequence of causality and of the frozen dynamics, different regions of the system independently choose different values for the order parameter while crossing the transition. The KZM predicts the scaling with τ_Q of the average size of such domains as the correlation length ξ at the freeze-out:

$$\hat{\xi} = \xi(\hat{\epsilon}) = \xi_0 \left(\frac{\tau_Q}{\tau_0}\right)^{\frac{\nu}{1+z\nu}} . \tag{1.16}$$

After the freeze-out the presence of independent phase domains may lead to the formation of topological defects, arising from discontinuities at the domain boundaries of the order parameter. Then the *density of defects* n created in the homogeneous system would scale with the quench time τ_Q as a power law:

$$n \sim \frac{\hat{\xi}^d}{\hat{\xi}^D} = \frac{1}{\xi_0^{D-d}} \left(\frac{\tau_0}{\tau_Q}\right)^{(D-d)\frac{\nu}{1+z\nu}} , \tag{1.17}$$

where the integers d and D are the dimensions of defects and phase domains respectively‡. This prediction for n typically overestimates the density of defects observed in numerical simulations and experiments. For a better estimate a multiplicative factor f should be introduced in the definition of $\hat{\xi}$ in equation (1.16), with the value of f being of the order of unity and depending on the specific model (del Campo et al., 2014).

1.2.2 Inhomogeneous KZM

The theoretical derivations of the previous section were obtained considering a homogeneous system. A different approach is needed in presence of an *inhomogeneous* external potential, as it is for the case of many experiments with trapped gases, where the inhomogeneities play a key role in the description of the KZM and further assumptions must be introduced (Zurek, 2009; del Campo et al., 2011; del Campo et al., 2013).

Let us take the example of a bosonic gas in a harmonic trap, undergoing Bose–Einstein condensation with the temperature being the control parameter. The main properties of this kind of system will be object of section 1.3.1. Considering an elongated system with a cigar-like shape, for simplicity we can restrict our attention to the spatial dependence along the axial dimension (Ketterle et al., 1996b). In such an inhomogeneous system above the transition point, the density of the gas ρ depends on the position z along the trap axis, since at thermal equilibrium the trap potential U maps the *local gas density* as

$$\rho(z) = \rho_0 \exp\left(\frac{-U(z)}{k_B T}\right), \tag{1.18}$$

with k_B being the Boltzmann constant, T the temperature of the gas, and ρ_0 the peak density. Therefore also the critical temperature T_c for the condensation acquires a spatial dependence:

$$T_c(z) \simeq \frac{2\pi\hbar^2}{m k_B}\left(\frac{\rho(z)}{2.61}\right)^{2/3}, \tag{1.19}$$

where m is the mass of the boson and $\hbar$ is the reduced Planck constant. For a simpler theoretical derivation one can assume that the temperature T is uniform in the gas during the quench, even if this condition may not be met experimentally. Following equation (1.10), for a linear quench the temperature can be expressed as

$$T(t) = T_c(0)\left(1 - \frac{t}{\tau_Q}\right), \tag{1.20}$$

‡ Considering the case of defects in a 3D superfluid, i.e., with $D = 3$, we have $d = 1$ for vortex lines and $d = 2$ for solitonic planes. In 1D systems solitons are point-like defects, hence $D = 1$ and $d = 0$.

where τ_Q is the quench time.

Despite the assumption of a uniform temperature in the gas, as a consequence of the local nature of T_c the transition does not occur simultaneously everywhere in the system. Different points will reach the critical temperature at different instants of the quench: a *front of the transition* can be identified as the boundary of that part of the system which has undergone the transition at a given time. From the definition $\varepsilon(z_F, t) = 0$, the position transition front $z_F(t)$ can be described with the following relation, derived from equation (1.20) considering the condition for the transition $T = T_c$:

$$\frac{t}{\tau_Q} = 1 - \frac{T_c(z_F)}{T_c(0)} \,. \tag{1.21}$$

Therefore the Bose–Einstein condensate (BEC) starts to form at $z \sim 0$, where the potential is deepest, and it spreads in the system with a transition *front velocity* that can be calculated as

$$v_F(z) = \left| \frac{dz_F}{dt} \right| = \frac{T_c(0)}{\tau_Q} \left| \frac{dT_c(z)}{dz} \right|^{-1} \,. \tag{1.22}$$

We can observe that in general v_F depends on the position in the trap, and that it is proportional to the quench speed τ_Q^{-1}.

The finite value of the transition front velocity plays a key role in inhomogeneous systems. If the quench is slow the condensate will grow around the initial seed: the order parameter chosen at the beginning, i. e., the BEC wave function at $z = 0$, will be spatially uniform after that the transition has been crossed in the whole sample. On the other hand, if the quench is fast the system can undergo the transition at unconnected positions in the trap, growing independently around local seeds and choosing random values of the order parameter. The relevant quantity that must be compared with the front velocity v_F is the characteristic speed at which perturbations travel, already introduced in equation (1.9). This is the maximum speed at which the choice of the order parameter can be communicated, and at the freeze-out it can be estimated as the velocity $\hat{v}$, defined as the ratio between the correlation length $\hat{\xi}$ and the relaxation time $\hat{\tau}$ at $\hat{\varepsilon}$, previously defined in equations (1.16) and (1.14):

$$\hat{v} \simeq \frac{\hat{\xi}}{\hat{\tau}} = \frac{\xi_0}{\tau_0} \left(\frac{\tau_0}{\tau_Q} \right)^{\frac{\nu(z-1)}{1+\nu z}} \,. \tag{1.23}$$

The KZM is activated when the moving transition front locally exceeds the *causal horizon* set by $\hat{v}$.

SLOW QUENCH If $v_F < \hat{v}$ the condensate grows with a uniform order parameter in the whole trap, and topological defects do not form. Conversely it should be noted that the formation of defects is always expected in the homogeneous case.

FAST QUENCH If $\nu_F > \hat{\nu}$ symmetry breaking happens on a local scale. This implies the formation of independent phase domains: similarly to the homogeneous case, defects can appear in the system at the boundaries between these domains, with a density which depends on $\hat{\xi}$.

The theoretical derivation of the defect number for the inhomogeneous KZM is not trivial, even given the approximations that have been introduced. Here we report the result derived by Zurek (2009) for the average total number of solitons formed after a temperature quench in a cigar-shaped BEC trapped in a harmonic potential, scaling as a power law of the quench time:

$$N \sim \frac{2\Delta^2}{\xi_0^2}\left(\frac{\tau_0}{\tau_Q}\right)^{\frac{1+2\nu}{1+\nu z}} . \tag{1.24}$$

Here $\Delta^2 = \frac{3k_B T}{2m\omega_z^2}$, where $\frac{\omega_z}{2\pi}$ is the axial trapping frequency.

1.2.3 Defect number scaling

From equations (1.17) and (1.24) one can deduce that, for every second-order phase transition in a generic system, the KZM predicts a *power-law scaling* for the defect density n with the quench time τ_Q, a quantity that can be measured in many experimental cases:

$$n \propto \tau_Q^{-\alpha} . \tag{1.25}$$

The predictions for the power-law exponent α are different for the homogeneous and inhomogeneous, specifically harmonic, cases, which gives respectively

$$\alpha_{hom} = (D-d)\frac{\nu}{1+\nu z} \tag{1.26a}$$

$$\alpha_{harm} = (D-d)\frac{1+2\nu}{1+\nu z} . \tag{1.26b}$$

The power-law exponent α depends on the critical exponents ν and z, whose values are not know a priori: in principle measurements on the KZ scaling can be used to test the theories predicting their values. Within this contest, for the universality class of interacting Bose gases a first theoretical approach for the critical exponents can be a pure mean-field calculation, giving $\nu = \frac{1}{2}$ and $z = 2$. Going beyond the mean-field theory, the so-called F-model predicts $\nu = \frac{2}{3}$ and $z = \frac{3}{2}$ (Hohenberg et al., 1977).

The exponent α of equation (1.26) depends also on the dimensionality of the defects d and of the system D. For solitons in 1D systems[§] we

§ In principle solitons can be present also in 2D and 3D systems, characterized by the same dimensionality factor $(D-d) = 1$. However there are theoretical and experimental evidences of their instability in such systems.

Table 1.1: Power-law exponent α of the KZ defect number scaling, calculated with equation (1.26) in different regimes. These results are obtained considering the critical exponents predicted with the F-model, $\nu = \frac{2}{3}$ and $z = \frac{3}{2}$ (Hohenberg et al., 1977).

	$(D-d)$	α_{hom}	α_{harm}
solitons	1	1/3	7/6
vortices	2	2/3	7/3

have $(D-d) = 1$, while vortices in 2D or 3D systems give $(D-d) = 2$. The power-law exponents predicted for these cases are reported in table 1.1 for the homogeneous and harmonic cases, considering the values of ν and z from the F-model, since recent experiments with ultracold gases seem to support this approach for the universality class of a BEC (Donner et al., 2007; Navon et al., 2015; Chomaz et al., 2015). Therefore, for a comparison between the KZ theory and measurements on the defect number scaling, the confinement regime of the system and the nature of defects must be known.

1.2.4 Experiments on the KZM

In his original paper Zurek proposed a *condensed matter experiment* setting an analogy with Kibble's theory for the formation of cosmic defects (Zurek, 1985). In particular he considered the system of liquid helium-4, where the phase transition from the normal to the superfluid state is driven by a pressure quench in an annular geometry, sketched in figure 1.3. In such a system the superfluid wave function can be taken as order parameter, and the causality is driven by the speed of second sound. If the quench is fast enough independent phase domains might be created in the superfluid, having a characteristic size of the order of the correlation length. Defects in the form of vortices are expected to form at the boundaries of the phase domains. Zurek's idea inspired many experimental works aimed to demonstrate the predictions of the KZ theory (Kibble, 2007; del Campo et al., 2014).

One of the first attempts to experimentally observe the KZM was performed with nematic liquid crystals. The formation of random disclinations, which are linear defects arising from the rotation of rod-shaped molecules around an axis and directly visible as in figure 1.4, was observed after fast temperature quenches in the liquid crystal (Chuang et al., 1991). However the phase transition considered in this experiment is of first order, hence the requirements for the application of the KZ theory are not fully met.

The proposal of Zurek exploiting the superfluid transition in ^{4}He, whose phase diagram is reported in figure 1.5, was implemented in

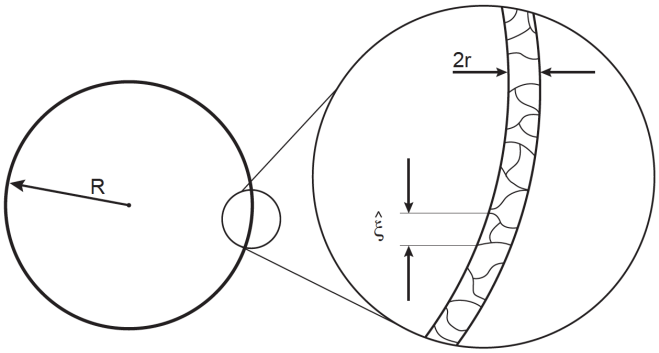

Figure 1.3: The experiment proposed by Zurek (1985) for the observation of the KZM was based on the superfluid transition in ^{4}He, considering a narrow annular geometry as sketched here (del Campo et al., 2014). After fast quenches independent phase domains are expected to form, having a typical size fixed by the correlation length $\hat{\xi}$.

Figure 1.4: Random defects formed in a nematic liquid crystal after a fast temperature quench (Chuang et al., 1991).

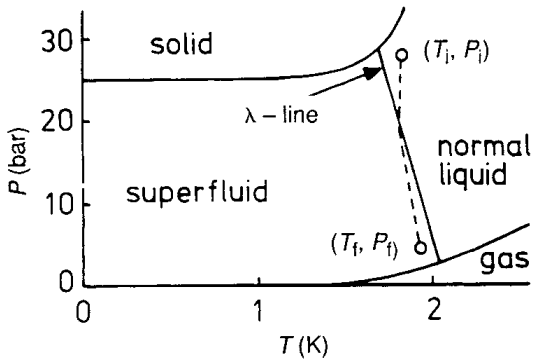

Figure 1.5: Pressure quenches across the normal to superfluid transition in helium-4 were initially considered in order to observe the KZM in experiments (Hendry et al., 1994).

an experiment described by Hendry et al. (1994). Even if the observation of vortices after rapid expansions suggested a possible agreement with the expectations for the KZM, the results were considered inconclusive because of the presence of a residual flow turbulence, which might have caused the formation of defects through other kinds of mechanisms. A later experiment with an improved experimental design was not able to reproduce such defects, supporting the idea that the first observations were in fact related to spurious artifacts (Dodd et al., 1998). The absence of vortices was attributed to their short lifetime, causing the defects to decay and disappear from the system too quickly to be observed.

Other cryogenic experiments were performed using the helium-3 isotope, whose superfluid phase supports vortices that are easier to be detected than in ^{4}He. A fast transition to the ^{3}He–B phase was triggered in two distinct experiments exploiting an exothermic nuclear reaction (Bäuerle et al., 1996; Ruutu et al., 1996). Those experiments were based on the heating of small portions of superfluid helium above the critical temperature, caused by the absorption of neutrons. These regions of helium in the normal phase are then rapidly cooled back by the surrounding superfluid, a process that can lead to the formation of random vortical filaments as represented in figure 1.6a. The indirect detection of vortices was based on a calorimetry measurement in the first experiment, and on a rotating cryostat in the second one, sketched in figure 1.6b. The observations reported in both studies were in agreement with the KZ model. However they were able to provide only indirect proofs about the defect number scaling, since the local heating associated to the nuclear reaction was almost instantaneous.

Since the first experiments on liquid helium, some of the predictions for the KZM were observed in many different systems, such as nonlinear optical systems (Ducci et al., 1999), thin-film superconductors (Carmi et al., 1999; Kirtley et al., 2003), annular Josephson junc-

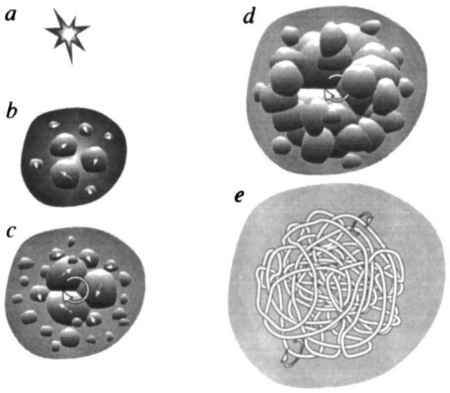

(a) Formation of vortices in ^{3}He (Bäuerle et al., 1996).

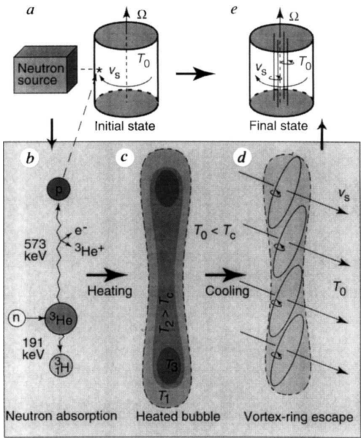

(b) Rotating cryostat in the experiment of Ruutu et al. (1996).

Figure 1.6: One of the first systems where the formation of defects predicted by the KZM was observed, was helium-3 undergoing the superfluid transition, with quenches being triggered by nuclear reactions.

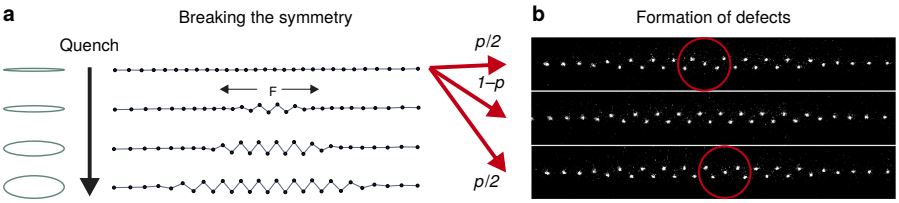

Figure 1.7: Sketch of the procedure for the quench of a Coulomb crystal through the modification of the trapping potential, which can lead to the formation of defects in the zigzag phase (Pyka et al., 2013).

tions (Carmi et al., 2000; Monaco et al., 2006), ferromagnetic spinor BECs (Sadler et al., 2006), multiferroic crystals (Chae et al., 2012), atomic Mott insulators (Chen et al., 2011; Braun et al., 2015), and others. Those observations seem to confirm the universality of the mechanism of random defect formation in systems crossing continuous phase transitions with fast quenches, a situation that in general may apply to many different physical systems. Some of the limits often encountered in experiments are set by the possibility of tuning the quench parameters and by the detection of defects.

The observation of defects formed via the KZM was reported also in Coulomb crystals made of ion chains by Pyka et al. (2013) and Ulm et al. (2013). These artificial systems show a structural phase transition of second order between the linear ion chain and the zigzag phase, driven by the variation of the trapping frequency. The formation of kinks, i. e., irregularities in the zigzag chain directly visible as in figure 1.7, has been observed for fast quenches across this transition. A good control of the quench speed allowed to measure the defect

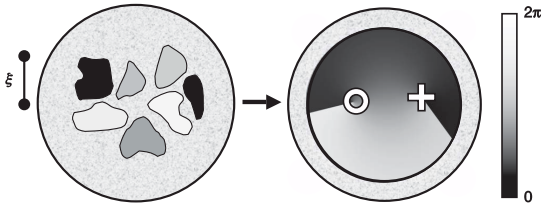

(a) Sketch of the formation of a vortex pair when different phase domains merge.

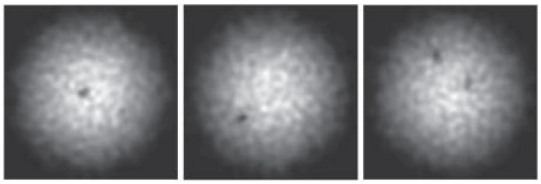

(b) Images of BECs containing one (left and center) and two (right) vortices.

Figure 1.8: Observation of vortices in a bosonic gas, spontaneously created after fast temperature quenches across the BEC transition (Weiler et al., 2008). After free expansion the defects are visible as dips in the density profile imaged along the symmetry axis of an oblate harmonic trap.

number scaling in a clear way. One possible drawback of those experiments might be that the Coulomb crystals are typically composed of a limited number of ions, with finite-size effects that cannot be ignored. Moreover those systems are affected by kink losses, decay processes that can alter the scaling measurement and that are only partially overcome by the introduction of optical dissipative mechanisms.

Dilute atomic gases undergoing *Bose–Einstein condensation* were already considered in the past as ideal candidates for testing the KZM (Kibble, 2007). They are simple systems, whose experimental parameters, such as temperature and sample size, can be finely controlled in clean environments. BECs can be produced in a variety of different experimental conditions and geometries, and direct observations of their properties are possible with several techniques such as absorption imaging. Within this framework, the creation of quantized vortices via the KZM was observed by Weiler et al. (2008) in pancake-shaped condensates, after fast temperature quenches performed with evaporative cooling across the critical point of the BEC transition. As it can be seen from figure 1.8, the randomly formed defects were directly visible in the density profile of the BEC after ballistic expansion. However in that experiment a measurement of the defect number scaling was not possible, since, due to experimental limitations, only few evaporation rates were considered.

In our laboratory we observed the spontaneous creation of defects via the KZM in a cigar-shaped BEC of sodium, and we measured for the

first time in ultracold gases a power-law scaling for the defect number with the quench time (Lamporesi et al., 2013b). As it will be described in chapter 3, this was possible thanks to the combination of imaging techniques that allowed for a good defect number counting, up to some units, and the possibility for the quench rate to be varied over a wide interval using evaporative cooling. In the next section we will introduce the principal characteristics of Bose–Einstein condensation, the phase transition considered for the measurements that will be presented in this thesis.

1.3 BOSE–EINSTEIN CONDENSATION

1.3.1 Properties of condensates

Bose–Einstein condensation is a phenomenon that was theoretically predicted by Satyendra Nath Bose and Albert Einstein between 1924 and 1925. In his work Bose introduced a new statical model explaining the black-body radiation in terms of photons, while Einstein expanded it to the case of a gas of indistinguishable atoms, applying the concepts proposed by Louis de Broglie for the wave nature of matter. A Bose–Einstein condensate (BEC) is a system where a quantum state is macroscopically occupied, showing intriguing characteristics such as superfluidity, phase coherence and the possibility to observe effects of quantum mechanics on a macroscopic scale.

The observation of the Bose–Einstein condensation in *dilute atomic gases* was reported for the first time by Anderson et al. (1995) and Davis et al. (1995), only some decades after its prediction, also thanks to the laser and evaporative cooling techniques developed in the meanwhile, which made accessible the temperature and density conditions needed for the phase transition. A variety of experimental techniques, e. g., exploiting the interaction of atoms with photons or magnetic fields, allow for the manipulation of this novel state of matter, which can be directly observed with different imaging methods. Experiments with BECs in ultracold gases are performed in clean environments, with a high control over many parameters of the system, such as temperature, occupation of internal states, confinement regime, and strength of atomic interactions (Ketterle et al., 1999; Cohen-Tannoudji et al., 2011). Indeed BECs are ideal quantum simulators for the study of problems belonging to many different fields of physics.

The phenomenon of Bose–Einstein condensation can be understood in a simplified picture as the transition from a classical to a quantum regime for a gas of bosons, i. e., indistinguishable atoms with integer spin obeying to the Bose–Einstein statistics. In general each particle can be described as a quantum wave packet, having a characteristic

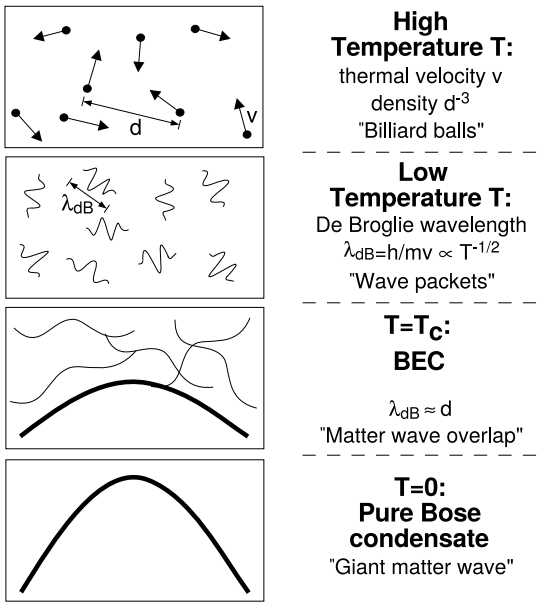

Figure 1.9: Qualitative representation of different regimes for a gas of bosons undergoing Bose–Einstein condensation (Ketterle et al., 1999). At the critical temperature the extent of the single-particle quantum wave packets becomes comparable with the average distance between atoms: a macroscopic number of atoms will condense in the ground state, forming a coherent state of matter described by the BEC wave function.

extent of the order of the thermal *de Broglie wavelength*, which is defined as

$$\lambda_{dB} = \sqrt{\frac{2\pi\hbar^2}{m k_B T}}, \tag{1.27}$$

where T is the gas temperature and m is the atomic mass. As sketched in figure 1.9, at high temperatures λ_{dB} is small compared to the interatomic distance, and the gas behaves as an ensemble of classical point-like particles. The value of λ_{dB} increases as the gas is cooled. In particular at the critical temperature T_c the thermal wavelength becomes of the order of the interatomic distance: hence a transition occurs, with a macroscopic number of atoms condensing in the same coherent quantum state at lowest energy.

Following the results derived in the book of Pitaevskii et al. (2016), for an ideal gas of N_{at} atoms at uniform density ρ the condition for Bose–Einstein condensation is

$$\rho\lambda_{dB}^3 = 2.61\,. \tag{1.28}$$

Consequently the *critical temperature* of the BEC transition can be expressed as

$$T_c = \frac{2\pi\hbar^2}{m k_B}\left(\frac{\rho}{2.61}\right)^{2/3}. \tag{1.29}$$

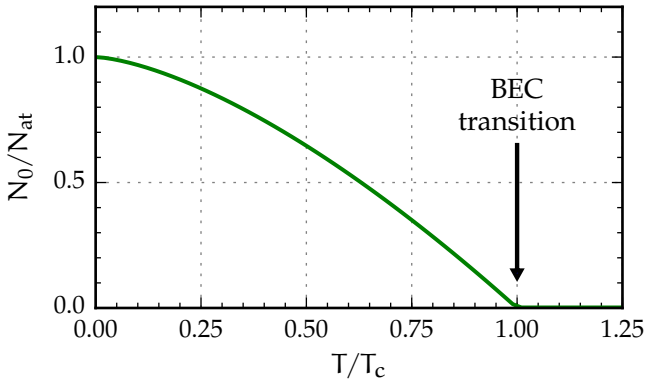

Figure 1.10: Condensed fraction of atoms as a function of temperature for a uniform ideal gas of bosons. The number of atoms in the condensate becomes macroscopic below the critical temperature of the BEC transition.

The number of atoms N_0 in the condensate becomes macroscopic below the critical temperature. As plotted in figure 1.10, in the thermodynamic limit the condensed fraction N_0/N_{at} is zero for $T > T_c$, while for $T < T_c$ it grows following the relation

$$\frac{N_0}{N_{at}} = 1 - \left(\frac{T}{T_c}\right)^{3/2} . \tag{1.30}$$

The number of atoms left in the non-condensed thermal fraction, i. e., $N_{at} - N_0$, becomes negligible as the temperature approaches zero.

Going beyond the ideal gas model, the realistic case of a gas of interacting particles confined in a trap should be treated including the particle-particle interaction potential V and the external potential U (Dalfovo et al., 1999). In terms of the second quantization formalism, such a many-body quantum system is described by the field operator

$$\hat{\Psi}(\mathbf{r}, t) = \sum_i \Phi_i(\mathbf{r}, t)\hat{a}_i , \tag{1.31}$$

where $\hat{a}_i$ is the annihilation operator for a particle in the state Φ_i. During Bose–Einstein condensation a single state, labeled with Φ_0, becomes macroscopically and coherently occupied, with an occupation number given by N_0. If the number of atoms N_{at} is big and if the non-condensed fraction is negligible, as it happens at low temperatures, the fluctuations over N_0 can be neglected and the operator $\hat{\Psi}$ can be replaced by a classical complex field Ψ_0, which is called the macroscopic *wave function of the condensate*:

$$\Psi_0(\mathbf{r}, t) = \sqrt{N_0}\Phi_0(\mathbf{r}, t) = |\Psi_0(\mathbf{r}, t)|e^{i\varphi(\mathbf{r},t)} . \tag{1.32}$$

The wave function Ψ_0 plays the role of the *order parameter* of the BEC transition. In fact, similarly to the magnetization in the ferromagnetic transition that was introduced in section 1.1, Ψ_0 is zero above

the critical point and it becomes finite as the temperature is lowered below T_c, being proportional to $\sqrt{N_0}$. The modulus squared of Ψ_0 determines the *density* of particles in the condensate:

$$\rho(\mathbf{r}) = |\Psi_0(\mathbf{r})|^2 . \tag{1.33}$$

The phase φ of the order parameter has a crucial importance for the coherence properties of the condensate. The choice of a random value of φ, happening at the transition, is linked to the phenomenon of spontaneous symmetry breaking relevant in the context of the KZM. Moreover the phase gradient contains information about the flow dynamics of the condensate, defining its velocity field, which can be expressed as

$$\boldsymbol{v}(\mathbf{r}, t) = \frac{\hbar}{m} \boldsymbol{\nabla} \varphi(\mathbf{r}, t) . \tag{1.34}$$

A further assumption can be done in the case of ultracold dilute gases, where the interaction between atoms is short ranged and atomic collisions can be described by a single real parameter, the *s*-wave scattering length a. This means that the interaction potential V can be replaced by an effective contact interaction, defined as

$$V(\mathbf{r} - \mathbf{r}') = g\delta(\mathbf{r} - \mathbf{r}') , \tag{1.35}$$

where δ is the Dirac delta function and g is the coupling constant, expressed as

$$g = \frac{4\pi\hbar^2 a}{m} , \tag{1.36}$$

whose value is positive for repulsive interactions, negative for attractive ones. Within the above hypotheses the evolution of the condensate wave function can be described with a particular case of nonlinear Schrödinger equation, known as the *Gross–Pitaevskii equation* (GPE):

$$i\hbar \frac{\partial}{\partial t} \Psi_0 = \left(-\frac{\hbar^2 \boldsymbol{\nabla}^2}{2m} + U + g|\Psi_0|^2 \right) \Psi_0 . \tag{1.37}$$

The GPE describes well BECs in the limit of low temperature $T \ll T_c$, high number of particles $N_{at} \gg 1$, and diluteness $\rho|a|^3 \ll 1$.

The balance between the kinetic energy and the effective interaction energy fixes a characteristic length scale, called *healing length*, which is defined as

$$\xi_l = \sqrt{\frac{\hbar^2}{2mg\rho}} = \frac{1}{\sqrt{8\pi\rho a}} . \tag{1.38}$$

This quantity sets the minimum length scale of density perturbations in the condensate wave function, such as defects, and it increases for weaker interactions and smaller particle densities.

For a gas confined in a *harmonic trap* the external potential at a given position $\mathbf{r}$ can be expressed as

$$U(\mathbf{r}) = \frac{1}{2} m \left(\omega_x^2 x^2 + \omega_y^2 y^2 + \omega_z^2 z^2 \right) , \tag{1.39}$$

with $\frac{\omega_i}{2\pi}$ being the trapping frequencies along the respective axes, labeled with $i = x, y, z$. Considering a trap with cylindrical symmetry the description of the potential reduces to $\omega_\perp = \omega_y = \omega_z$ in the radial plane and $\omega_\parallel = \omega_x$ along the symmetry axis. The trap can be either spherical for $\omega_\parallel = \omega_\perp$, cigar-shaped for $\omega_\parallel < \omega_\perp$, or pancake-shaped for $\omega_\parallel > \omega_\perp$. The conditions for the 1D and 2D regimes can be reached in tightly confined traps (Görlitz et al., 2001).

When the number of particles is sufficiently high the kinetic term in the GPE can be neglected. The condition for the validity of this approximation, which is referred as the *Thomas–Fermi limit*, is given by

$$\frac{N_0 a}{a_{ho}} \gg 1 , \tag{1.40}$$

where a_{ho} is the harmonic oscillator length defined as

$$a_{ho} = \sqrt{\frac{\hbar}{m\omega_{ho}}} , \tag{1.41}$$

introducing the geometric mean of the trapping frequencies as

$$\omega_{ho} = \sqrt[3]{\omega_x \omega_y \omega_z} . \tag{1.42}$$

In the Thomas–Fermi limit the *atomic density* of the condensate in the ground state maps the harmonic potential, hence taking the shape of an inverted parabola:

$$\rho(\mathbf{r}) = \max\left(\frac{\mu - U(\mathbf{r})}{g}, 0 \right) . \tag{1.43}$$

Here μ is the chemical potential, which represents the variation of the total energy of the system when a single particle is added or removed. The radii of the ellipsoid corresponding to the atomic cloud are called *Thomas–Fermi radii*, defined as

$$R_i = \sqrt{\frac{2\mu}{m\omega_i^2}} \tag{1.44}$$

for each axis i. Following the condition of normalization for equation (1.43) over the spatial extent of the condensate given by R_i, the *chemical potential* can be expressed as

$$\mu = \frac{\hbar\omega_{ho}}{2} \left(\frac{15 N_0 a}{a_{ho}} \right)^{2/5} . \tag{1.45}$$

1.3.2 Defects in condensates

Bose–Einstein condensates in dilute gases at low temperatures are described by the GPE, which was introduced in equation (1.37). Its ground state solution is characterized by a uniform phase of the condensate wave function, and by a regular density profile mapping the external potential. However the GPE also admits different stationary solutions at higher energies, whose phase and density profiles are more intricate. In particular we can talk about a *defect* of the condensate when the many-body excitation results in a wave function with a localized deviation from the ground state.

A special class of solutions of the GPE is represented by *solitons* (Frantzeskakis, 2010). Considering the 1D solutions for systems with repulsive interactions, a soliton is a localized density depletion, moving as a solitary wave at a constant velocity v while maintaining its shape. Solitons are called *dark* when they are characterized by a compete depletion in the density profile, corresponding to a discontinuity in the phase equal to π: they appear as stationary defects with a typical size of the order of the healing length ξ_1. Conversely solitons are called *gray* when they move at a finite velocity v, with a partial density suppression and a shallower phase jump, as plotted in figure 1.11. In fact, the minimum density in the solitonic plane and the phase jump between the two sides of the system are respectively

$$\rho(0) = \rho_0 \frac{v^2}{v_s^2} \tag{1.46}$$

$$\Delta\varphi = 2 \arccos\left(\frac{v}{v_s}\right) , \tag{1.47}$$

with v_s being the speed of sound in the system and ρ_0 the bulk atomic density (Pitaevskii et al., 2016). The respective energy per unit of surface of a soliton can be expressed as

$$\varepsilon_{sol} = \frac{4}{3}\hbar v_s \rho_0 \left(1 - \frac{v^2}{v_s^2}\right)^{3/2} . \tag{1.48}$$

In experiments solitons can be artificially created in BECs by means of phase imprinting techniques, where the phase jump is imprinted using optical potentials with sharp profiles (Burger et al., 1999; Denschlag et al., 2000).

Solitons in 1D systems behave as stable point-like defects. The description of solitons can be extended to 2D and 3D systems, where they appear as linear or planar defects respectively. In particular in 3D cigar-shaped systems the depleted solitonic plane minimizes its surface taking an orientation perpendicular to the long axis in order to reduce its total energy, calculated as the integral of the expression in equation (1.48) in the transverse plane. However, in the cases

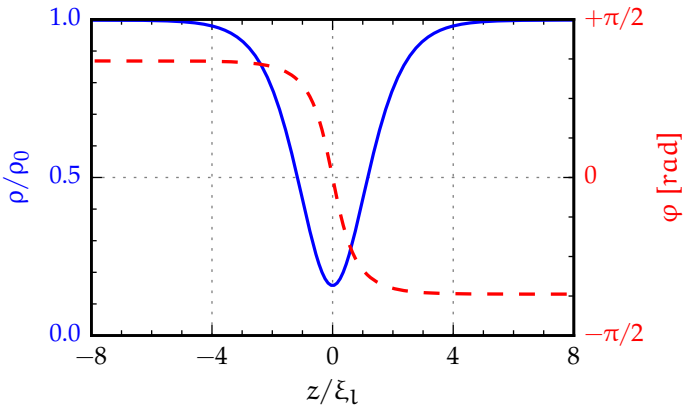

Figure 1.11: Profiles of normalized density (solid blue, left scale) and phase (dashed red, right scale) for a gray soliton, plotted as a function of the relative spatial coordinate in a 1D system. Here we consider a soliton moving at $v = 0.4v_s$, where v_s is the speed of sound.

with dimensionality higher than one, solitons are unstable: both experimental and theoretical studies show that solitons suffer from dynamical instabilities, which cause their bending and evolution into more stable structures, such as vortices or vortex rings, through a decay phenomenon also known as snaking instability (Anderson et al., 2001; Cetoli et al., 2013).

Quantized *vortices* are excited solutions of the GPE showing phase circulation, which can be defined in 2D and 3D systems (Kasamastu et al., 2009). The wave function of a vortex shows a local cylindrical symmetry, with a phase profile displaying a continuous variation form $-\pi$ to $+\pi$ while winding around the vortex axis, as represented in figure 1.12. Following the definition of the velocity field given in equation (1.34), this means that the gas rotates around the vortex core, with a tangential velocity that decreases with the distance from the axis. The density of the gas goes to zero at the singularity of the vortex core, which in a 3D system appears as a linear depletion with a radial size of the order of the healing length ξ_l. In an axially symmetric system of radius R the excitation energy of the vortex scales as the length of the nodal line L (Pitaevskii et al., 2016):

$$E_{vor} = L\pi\rho\frac{\hbar^2}{m}\ln\left(\frac{1.46\,R}{\xi_l}\right). \tag{1.49}$$

The description of vortices can be extended to even more complex structures, such as vortex rings, i. e., defects where the nodal line is closed in a circular configuration (Anderson et al., 2001).

The first experimental observations of quantized vortices in BECs were reported in oblate systems with cylindrical symmetry. A vortex can take a stable configuration in the center of the trap when its

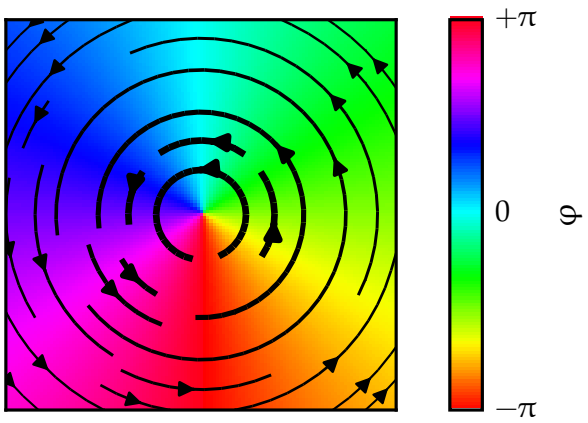

Figure 1.12: Phase profile of a vortex. The arrows represent the velocity field circulating around the vortex core, with thicker arrows for higher velocities.

axis is oriented along the short axial direction, hence minimizing its energy expressed in equation (1.49) and exhibiting an isotropic circulation. Vortices can be created in a BEC using several different techniques. Among them a vortex can be imprinted in a deterministic way using two-photon Raman processes, which couple different internal states of atoms with a transfer of angular momentum (Matthews et al., 1999), or by means of stirring optical potentials, hence inducing a circulating flow in the condensate (Madison et al., 2000). A completely different approach for the creation of vortices relies on the KZM: as introduced in section 1.2.4 while discussing figure 1.8, the spontaneous formation of vortices after fast temperature quenches was observed by Weiler et al. (2008), resulting from the relaxation of a random pattern of independent phase domains created at the BEC transition.

Whereas solitons and vortices were studied in theory and experiments considering axially symmetric systems, numerical simulations of the GPE showed that different kinds of stationary states can be obtained by breaking the cylindrical symmetry (Brand et al., 2001, 2002; Komineas et al., 2003). In the simplest case these excitations are called *solitonic vortices*, defects setting a link between solitons and vortices: as it can be seen from the calculated density and phase profiles of figure 1.13, a solitonic vortex (SV) in a cigar-shaped trap appears as a deformed vortex, with a phase gradient concentrated in the transverse region corresponding to a shallow solitonic plane.

For condensates trapped in elongated harmonic potentials with cylindrical symmetry, the nature of stable defects depends on the dimensionless *confinement parameter* γ, defined as the ratio between the chemical potential μ and the transverse harmonic oscillator energy $\hbar\omega_\perp$, or equivalently between the Thomas–Fermi radius in the

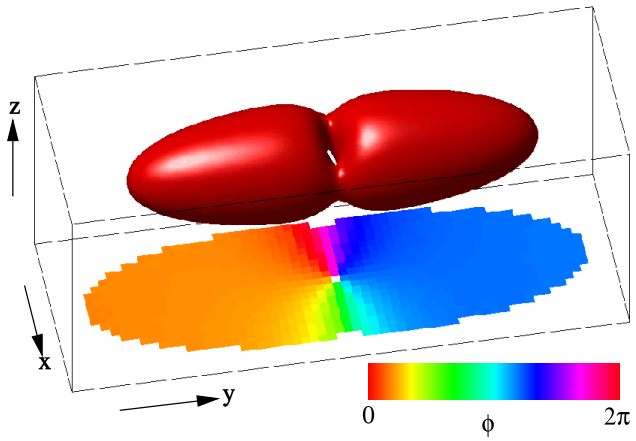

Figure 1.13: Phase profile (color scale plane) and equi-density surface (red) for a solitonic vortex simulated in a 3D harmonic trap (Brand et al., 2002).

transverse direction $R_\perp$ and the healing length ξ_l (Brand et al., 2002; Komineas et al., 2003):

$$\gamma = \frac{\mu}{\hbar\omega_\perp} = \frac{R_\perp}{2\xi_l}\,. \tag{1.50}$$

The energy spectrum calculated for a continuous variation of γ, reported in figure 1.14, shows that when $\gamma \ll 1$ solitons are the only possible stable structures. Conversely additional kinds of defects characterized by lower excitation energies are possible at larger values of γ, hence introducing the possibility of a decay channel of solitons into more stable states via snake instability (Becker et al., 2013). This possibility sets in when γ is of the order of unity, which corresponds to the crossover from the effective 1D regime to the 3D regime in the limit of $T = 0$. In particular for $\gamma \gg 1$ the least energetic state is the SV, whereas vortex rings or defects with more complex geometries exhibits higher energies (Mateo et al., 2014).

The spontaneous formation of defects in cigar-shaped BECs of sodium has been studied in our laboratory in Trento. Our first observations of defects in the condensate were done while optimizing the procedure of evaporative cooling. Initially we identified those defects as solitons, randomly produced via the KZM after fast temperature quenches across the BEC transition. As I will describe in chapter 3, we characterized this phenomenon as a function of the quench speed, measuring a power-law scaling for the average number of defects with the quench time (Lamporesi et al., 2013b). However, the contextual observation of a long defect lifetime appeared in contrast with our knowledge about the stability of solitons in 3D systems. This observation suggested us to study more in detail the nature of defects produced in our system. In chapter 4 I will discuss how the characterization of phase and density profiles of defects allowed us to identify them as solitonic vortices (Donadello et al., 2014; Tylutki et

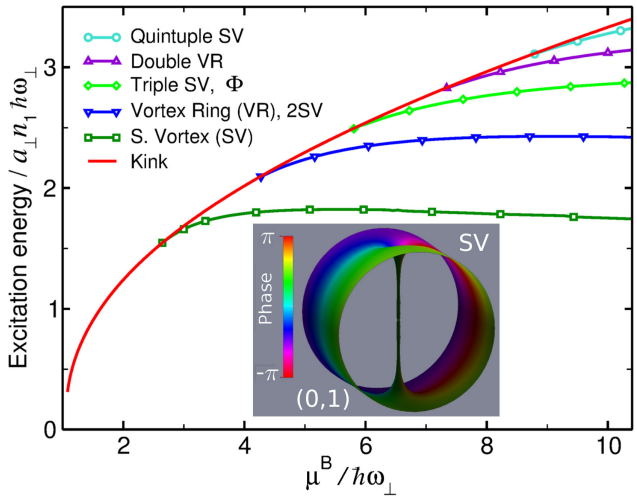

Figure 1.14: Excitation energy of defects calculated as a function of the confinement parameter defined in equation (1.50) for solitonic kinks, vortex rings, solitonic vortices, and more complex defects in a cylindrical trap (Mateo et al., 2014).

al., 2015). Finally, as I will present in chapter 5, the dependence of the predictions of KZ theory on the defect dimensionality suggested us to explore the defect number scaling in different confinement conditions, also studying the possible effects of defect evolution on those measurements.

2 PRODUCTION AND OBSERVATION OF A BEC

Experiments with ultracold gases require efficient atomic sources and stable experimental conditions in terms of many physical parameters, such as vacuum quality, laser stability and timing precision. In order to fulfill these requirements a reliable control over many instruments is typically needed. In this chapter I will introduce our experimental setup and the main techniques that we use for the realization of experiments with Bose–Einstein condensates.

The main parts of our experimental apparatus will be described in section 2.1. There I will present the high-flux atomic source based on laser cooling techniques that provides samples of cold sodium atoms, which are subsequently transferred in the magnetic trap where, using evaporative cooling, we reach quantum degeneracy. In section 2.2 I will describe the imaging techniques and the image analysis procedures implemented in the laboratory for probing the atoms. Finally in section 2.3 I will present the digital system and the relative software used to control the experimental sequence and the various instruments.

2.1 EXPERIMENTAL APPARATUS

2.1.1 Atomic source

The conditions for quantum degeneracy in dilute atomic gases were made accessible also thanks to the progress in laser and evaporative cooling techniques, which are particularly efficient for alkali atoms and that led to the first observations of the Bose–Einstein condensation in gases of rubidium and sodium (Anderson et al., 1995; Davis et al., 1995). The growing interest in this new kind of systems inspired the development of specific and efficient *atomic sources* in order to expand the possibilities of experiments with ultracold atoms, hence opening to new and promising options.

Atomic sources based on *laser cooling* can be divided into two main classes.

- The first one uses dissipative light forces and inhomogeneous magnetic fields to slow down a thermal flux of atoms coming from an oven. A typical implementation of this type of sources is the Zeeman slower (ZS), a stage where fast atoms are slowed down with a counter-propagating laser beam in a specifically

designed magnetic field. The slowed atoms can be subsequently trapped and cooled in magneto-optical traps (MOTs) (Phillips et al., 1982).

- The second class of atomic sources exploits atomic vapors directly loaded and cooled in a MOT: these kinds of setups have a simpler design, but they provide significant performances only for sufficiently heavy atoms, such as potassium, rubidium and cesium (Catani et al., 2006; Dieckmann et al., 1998; Yu et al., 1994). In fact, in general a MOT can capture only atoms moving below a certain critical velocity: considering equal temperatures, the fraction of the thermal distribution that stays below a given capture velocity is smaller for lighter atomic masses.

Experiments involving high atom numbers of light alkali species, such as lithium and sodium, typically need the implementation of atomic sources based on very efficient ZS stages (van der Stam et al., 2007). However these kinds of systems exhibit some drawbacks: the long ZS stages can suffer of significant flux losses due to the atomic beam divergence, and often the experimental setups result big and complex to be operated, hence possibly reducing the vacuum quality by the presence of hot background atoms.

Recently a different type of atomic source based on a 2D MOT was developed for lithium by Tiecke et al. (2009), being able to combine compactness with the possibility of a high atomic yield. In our laboratory we extended this alternative approach to *sodium*, implementing a hybrid solution based on a 2D MOT and a compact ZS. Moreover we took advantage of the progresses in the field of diode laser sources: as a matter of fact, the wavelengths suitable for laser cooling of sodium became accessible also with solid state lasers, without the need of more complex dye lasers as previously required.

In our atomic source the 2D MOT is loaded transversely with a flux of atoms coming from an oven containing metallic sodium, which is heated by about 140 °C above its melting point at 97.8 °C. A resonant laser beam aligned with the unconfined direction can be used to push atoms from the 2D MOT, hence producing a beam of atoms moving horizontally. The atomic flux is increased by about an order of magnitude exploiting a laser beam that, in combination with the residual magnetic field of the 2D MOT, acts like a very short ZS stage which slows down the thermal atoms coming from the oven. Finally we obtain a collimated atomic beam with a flux of more than 4×10^9 atoms per second.

The *vacuum setup* is sketched in figure 2.1. It is divided into two parts: the high vacuum (HV) chamber where the sodium oven and the 2D MOT are present, and the ultra-high vacuum (UHV) chamber where the experiments are performed in a clean environment. The two parts are connected with a differential pumping channel, which allows for a differential pressure between the HV and UHV chambers up to 10^3.

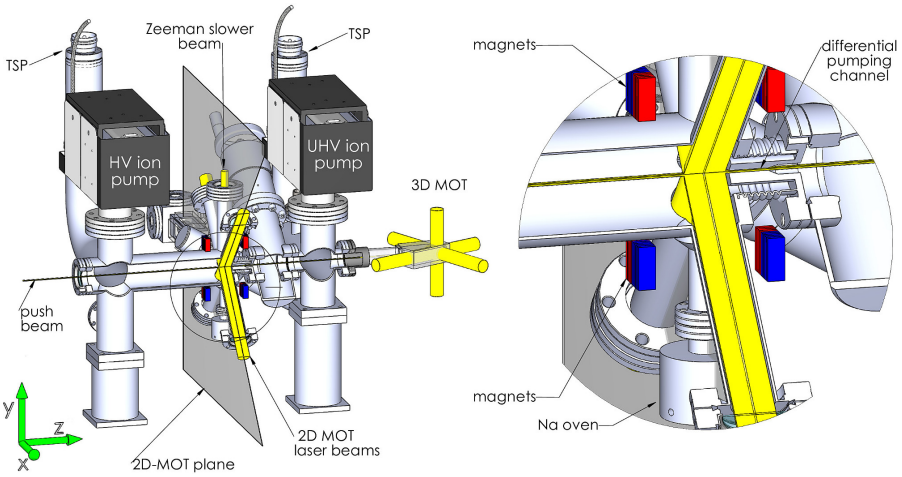

Figure 2.1: View of our atomic source of sodium. The atoms are transferred from the 2D MOT to the 3D MOT with a horizontal push light beam. The MOT light beams are drawn in yellow. The magnification of the 2D MOT region and of the differential pumping channel connecting the HV and the UHV parts is reported on the right.

Two ion pumps (Varian Starcell, with nominal pumping speed of $55\,\mathrm{L\,s^{-1}}$) and two titanium sublimation pumps allow to reach a pressure which is below the instrumental resolution of 10^{-10} mbar in the UHV part.

The atoms of the atomic source are transferred by the push light beam through the differential pumping channel in the UHV chamber, where a 3D MOT captures them. The system results more compact and simple than similar setups for sodium. As a consequence of compactness, the vertical path of atoms from the oven to the 2D MOT and the horizontal one during the transfer to the UHV chamber are short: this allows for higher atomic fluxes available for capture in the 3D MOT, since the losses caused by the atomic beam divergence are reduced. As it can be seen from figure 2.2, it is possible to use different atomic species simultaneously, since the 2D MOT can be loaded from different radial directions. A mixture of cold gases of sodium and potassium in the 3D MOT and in an optical dipole trap has been realized with this apparatus (Toffali, 2013).

The magnetic fields required to operate the 2D MOT and the ZS are obtained with permanent magnets, whereas the quadrupole field of the 3D MOT is produced with the same coils used for the magnetic trap (MT), as it will be described in section 2.1.3. In order to allow for a good optical access and to minimize uncontrolled magnetic fields, the 3D MOT is realized in a quartz cell, which can be seen from the photo in figure 2.3. A detailed description and characterization of the atomic source can be found in my master thesis (Donadello, 2012) and in the article published on the topic (Lamporesi et al., 2013a).

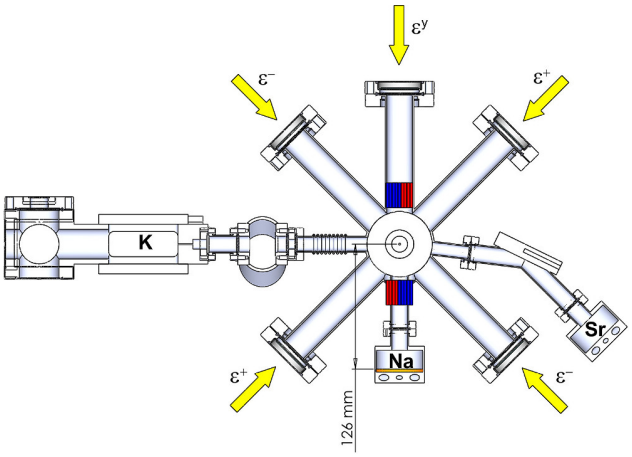

Figure 2.2: Radial section of the apparatus in the 2D MOT plane. Each light beam reports its polarization ε. In addition to sodium a flux of potassium atoms can be obtained from the left side. Even a strontium oven is present on the right, not yet activated.

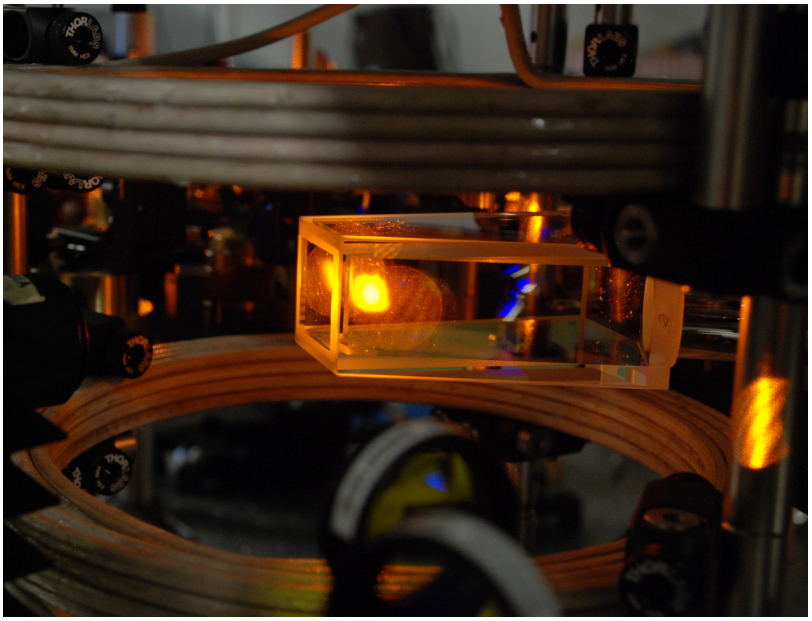

Figure 2.3: Cloud of sodium atoms trapped in the 3D MOT, emitting yellow light due to the fluorescence induced by the laser cooling beams. The photo was taken before the MT was mounted around the quartz cell.

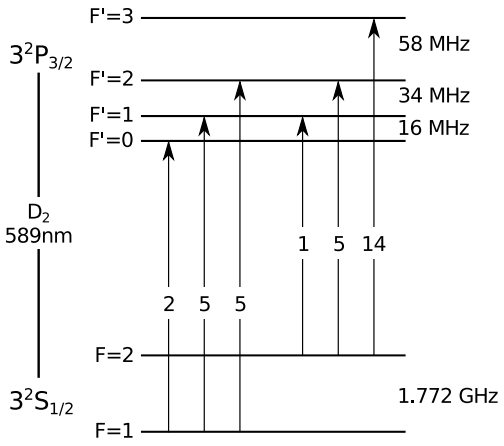

Figure 2.4: Hyperfine level structure of the sodium D_2 line, with the energy spacing between different levels given in frequency units. Each transition is reported with its relative strength.

2.1.2 Optical system

Laser cooling is a required first step in essentially all experiments with ultracold gases. The combination of dissipative light forces with magnetic fields allows to pre-cool hot atomic samples from hundreds of K down to some tens of µK in a few ms, representing a fundamental prerequisite for the subsequent experimental steps in conservative traps (Cohen-Tannoudji et al., 2011). The laser light used in laser cooling techniques must have suitable properties in terms of spectral linewidth and polarization definition, and it must be stably tuned in resonance with a closed atomic transition.

Sodium is an alkali atom, with the valence electron determining its principal electronic properties. In our case the laser cooling transition corresponds to the D_2 line, which in spectroscopic notation* is expressed as $3^2S_{1/2} \rightarrow 3^2P_{3/2}$. The atomic transitions of main interest here are sketched in figure 2.4. The wavelength in vacuum associated to the D_2 transition of sodium is 589.16 nm, which is not directly accessible with diode lasers. However, the recent developments in the quantum dot laser technology made accessible also the near-infrared region of the spectrum around 1100–1200 nm. This means that with a frequency doubling process we are able to use a *solid state laser* system also for sodium, which has a simpler design compared to other kinds of laser sources based on dye lasers.

The master source is a home-made external-cavity diode laser (ECDL) in Littrow configuration (Ricci et al., 1995). The active medium is a diode based on InAs quantum dots (INNOLUME GC-1178-TO-200), emitting in the infrared region around 1178 nm. The light of the diode is collimated using an aspheric lens (THORLABS C340TME-B). The ex-

* In atomic physics the quantum numbers associated to an atomic state are commonly labeled as $n^{2s+1}L_j$, where n is the principal quantum number, s the total spin, L the orbital angular momentum, and j the total angular momentum.

ternal cavity output coupler and wavelength discriminator is realized with a holographic grating with 1200 lines per mm (THORLABS GH13-12V), such that the cavity free-spectral-range is about 10 GHz. The temperature of the diode is stabilized with a controller driving a Peltier-cell. The ECDL configuration allows for a good tunability of the output wavelength, which can be changed with the orientation of the grating. Fine tuning can be obtained by applying a voltage to a piezoelectric crystal fixed to the holder of the grating.

The master laser is optically amplified with a Raman fiber amplifier (MPB RFA-SF-SERIES), pumped with a Ytterbium fiber laser. The input power of 20 m*W* is amplified to about 7 *W*, while maintaining the polarization and spectral properties of the master laser. Then the infrared light is doubled in frequency with a LiB_3O_5 non-linear crystal placed within a resonant cavity, obtaining about 3.5 *W* of yellow light at 589 nm.

The wavelength of the master laser is stabilized by performing frequency modulation saturated spectroscopy on a sodium vapor-cell. The dispersive signal of the saturated absorption is used as error signal to a feedback loop controller, acting on the voltage applied to the piezoelectric crystal of the ECDL. The emission frequency of the master laser is locked directly on the D_2 transition of sodium, hence obtaining a stable and reliable frequency reference.

The frequency-stabilized light is split into several secondary beams using polarizing beam splitters. The intensity and frequency of each beam are independently controlled with radio frequency (RF) signals driving acousto-optic modulators (AOMs) and electro-optic modulators (EOMs), which are placed on the beam paths. Each beam is then injected into polarization-maintaining optical fibers and transported to the main optical table which hosts the atomic source. The laser system and the optical beams used in experiments are sketched in figure 2.5.

Besides the resonant laser source just described, in the laboratory we also have a Nd:YAG laser, which can be used for the creation of optical dipole potentials (Grimm et al., 2000). For this aim we use a commercial source (INNOLIGHT MEPHISTO MOPA), which provides up to 42 *W* at 1064 nm. This infrared light is red-detuned considering the D_2 atomic transition of sodium, hence it can be directly used for the creation of attractive potentials. Alternatively we can create repulsive potentials with blue-detuned light obtained by frequency doubling the infrared light. In this case a 30 *W* beam is sent through a PP-SLT non-linear crystal†, and with just a single pass we can obtain more than 6 *W* of green light at the wavelength of 532 nm.

† The condition of quasi-phase matching can be obtained with Periodically Polled Stoichiometric Lithium Tantalate crystals without the need of resonant cavities.

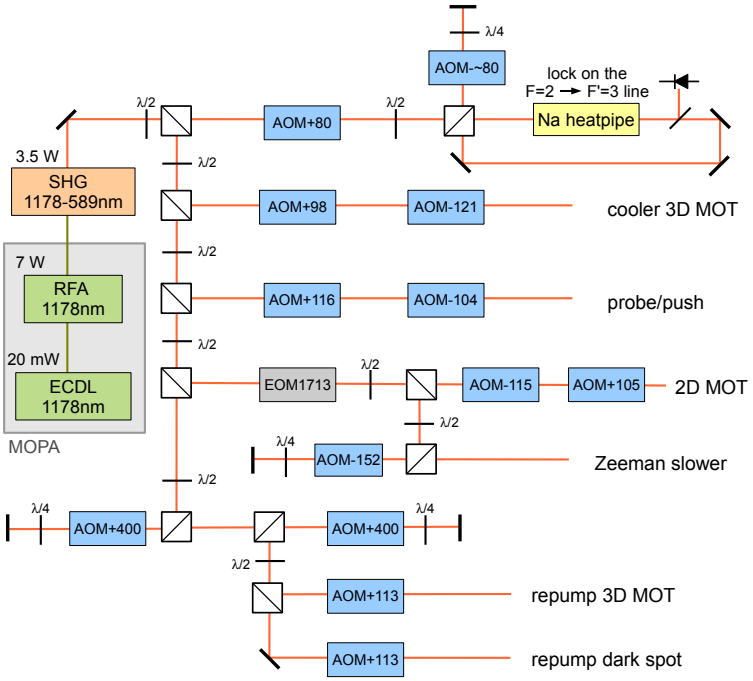

Figure 2.5: Scheme of the optical setup used for the production of the light beams needed for the laser cooling of sodium. The laser source is based on a ECDL, whose light is amplified and frequency doubled. The master laser wavelength is stabilized performing saturated spectroscopy on a sodium vapor-cell. The laser beams are split with polarizing beam splitters, and the light polarization is modified with $\lambda/2$ and $\lambda/4$ wave-plates. Each AOM and EOM reports its working frequency. The lenses for the focusing and collimation of beams are omitted.

2.1.3 Magnetic trap

The manipulation of neutral atoms with magnetic fields has been proven to be particularly effective in experiments with cold gases. In particular magnetic gradients and potentials with specifically designed profiles are used during most of the laser cooling techniques and for the realization of conservative traps (Ketterle et al., 1999).

In our experiments the first laser cooling stages need a simple magnetic configuration. In fact for the atomic source we use 4 stacks of 9 neodymium *permanent magnets* (ECLIPSE N750-RB) each, placed around the HV chamber to obtain a quasi-2D magnetic quadrupole configuration, suitable for the 2D MOT: the magnetic field is zero along the unconfined axis, while it varies linearly in the capture region along the transverse plane. Far from the 2D MOT the magnetic field reaches its maximum and decays with the distance: the tails of this vanishing magnetic field are exploited for the realization of the compact ZS stage.

Once the atoms are transferred from the atomic source to the quartz cell, we must be able to dynamically change the magnetic field configuration during the experimental sequence, and eventually to turn all fields off. A typical experimental procedure includes the following steps.

MAGNETO–OPTICAL TRAP At the beginning of experiments the atomic samples are trapped and cooled in a *dark-spot* 3D MOT (Ketterle et al., 1993). This is obtained with the combination of a quadrupole magnetic field, of three orthogonal pairs of counterpropagating laser cooling beams, and of a single dark-spot repumping beam, obtained by imaging on the atomic cloud an 8 mm diameter black dot. Before the transfer in the MT a sub-Doppler cooling stage based on optical molasses is performed in absence of magnetic fields (Lett et al., 1988), obtaining about 3×10^9 atoms at 50 µK.

MAGNETIC TRAP After the atomic samples have been pre-cooled with laser cooling they are transferred into a Ioffe–Pritchard *conservative* MT (Pritchard, 1983). Its non-vanishing magnetic field produces a cigar-shaped harmonic potential that confines atoms, which can be further evaporatively cooled or manipulated with other techniques. In the MT the conditions for Bose–Einstein condensation are typically reached with 30×10^6 atoms at 800 nK, with a peak atomic density of the order of 10^{13} atoms per cm^3.

MAGNETIC LEVITATION A vertical magnetic field gradient of about $8\,G\,cm^{-1}$ can be used to produce a force that compensates the *gravity*, hence levitating the atoms while letting them to expand for long time of flights (TOFs) without falling.

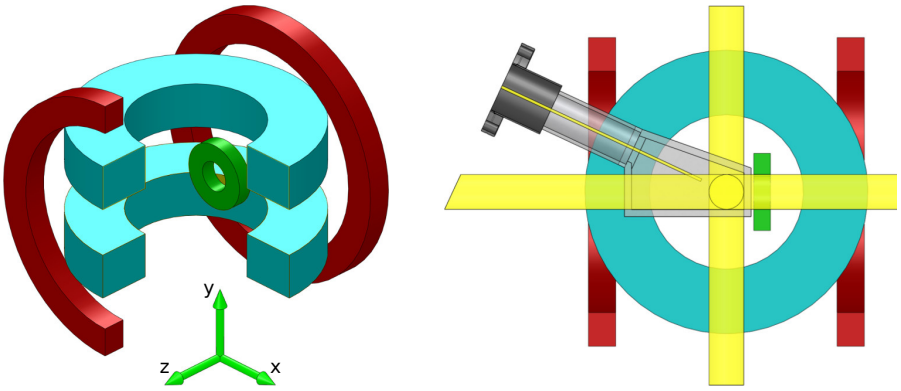

Figure 2.6: Views of the coils of the MT: quadrupole coils (cyan), compensation coils (red), and pinch coil (green). In the top view (on the right) the quartz cell and the 3D MOT laser beams (yellow) are also reported.

In our laboratory the magnetic field configurations just described are obtained with different combinations for the *current* flowing in the *coils* represented in figure 2.6.

- The quadrupole field is produced with a pair of twin coils with the same current flowing in opposite directions in anti-Helmholtz configuration. Each quadrupole coil is composed of 72 windings around an internal radius of 5.5 cm, placed at ± 2 cm along the vertical direction relative to the center of the trap.
- The levitating magnetic field gradient is obtained with the current flowing only in one of two quadrupole coils.
- A pinch coil is added in the MT configuration to provide a non-zero field minimum. This is composed of 12 windings around an internal radius of 1.3 cm, and it is placed at 2 cm of distance from the trap center along the horizontal symmetry axis.
- Another pair of coils can be used to compensate the bias field. These are composed of 16 windings around an internal radius of 8.7 cm, and are placed at ± 7.5 cm along the symmetry axis.

The magnetic field minimum of the 3D MOT and of the MT share the same spatial position: therefore we can switch between the different magnetic configurations without changing the location of atoms, exploiting the electric circuit based on relays switches and insulated-gate bipolar transistors (IGBTs) that is sketched in figure 2.7. The IGBTs (SEMIKRON SKM400GAL12E4) can be used either as fast switches, characterized by a response time of about 1 µs, or as variable resistors if driven with an analog voltage.

The continuous current flowing in the coils is generated with power supplies (DELTA ELEKTRONICA SM30-200) which can be programmed to output up to 200 A, characterized by a maximum rms-ripple noise

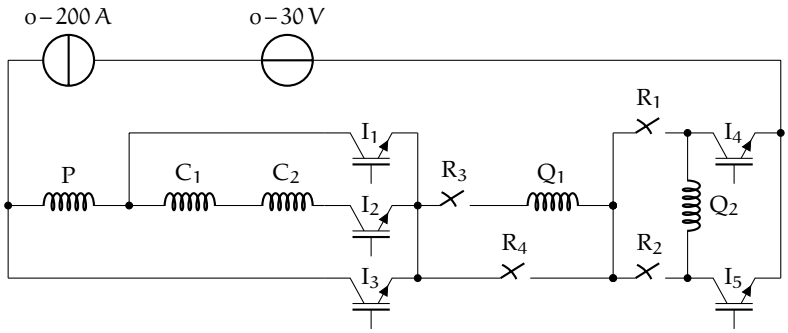

Figure 2.7: Electrical scheme of the magnetic field control system, composed of the quadrupole coils (Q), the compensation coils (C) and the pinch coil (P). The required magnetic fields are obtained with different combinations for the current flowing in the coils, programmed with IGBTs (I) and relay switches (R).

of the order of 20 mA. Further smaller coils with fixed currents are used to compensate static magnetic fields of the laboratory environment. The typical working conditions at the BEC transition point are reached with a current of 100 A, where the magnetic trap is characterized by a bottom field $B_0 \simeq 2\,G$, a field gradient $B' \simeq 106\,G\,cm^{-1}$, and a field curvature $B'' \simeq 59\,G\,cm^{-2}$. Under these conditions the axial and radial trapping frequencies are $\frac{\omega_\parallel}{2\pi} \simeq 13\,Hz$ and $\frac{\omega_\perp}{2\pi} \simeq 131\,Hz$ respectively, with an aspect ratio of about 10. A detailed characterization of the MT can be found in the master thesis of Serafini (2013).

2.1.4 Evaporative cooling

The sodium atoms are trapped in the conservative MT in the low-field seeking state $|F, m_F\rangle = |1, -1\rangle$. The trapped atomic samples are characterized by a lifetime of about 5 minutes, limited by background pressure. They are cooled down with forced RF *evaporative cooling*, a technique that consists in continuously removing the atoms belonging to the high energy tail of the thermal distribution of a gas (Ketterle et al., 1996a). This cooling step allows us to reach the conditions for the BEC transition, obtaining about 10×10^6 atoms in the final condensate.

In the presence of a weak magnetic field, the Zeeman splitting between adjacent magnetic sub-levels in frequency units is $\mu_B g_F h^{-1} = -0.70\,MHz\,G^{-1}$. Here h is the Plank constant, μ_B the Bohr magneton, and g_F the Landé g-factor, equal to $-\frac{1}{2}$ for the ground state hyperfine level $F = 1$. Following the scheme of figure 2.8, the Zeeman sub-levels with $m_F = -1$ and $m_F = 0$ are coupled by a RF field on the surface where the magnetic potential equals the photon energy $h\nu$, with ν being the radiation frequency. This means that the spin-flip to the untrapped state $|F, m_F\rangle = |1, 0\rangle$ is induced by RF for atoms having a total energy larger than $h(\nu - \nu_0)$, where ν_0 is the frequency at the

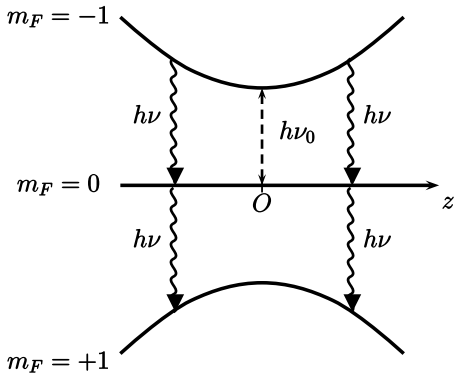

Figure 2.8: Energies of the Zeeman sub-levels m_F relative to the $F = 1$ hyperfine level for an atom in a magnetic potential, plotted as a function of the position in the trap (Cohen-Tannoudji et al., 2011). The atoms coupled by the radiation of frequency ν are transferred in the untrapped state $m_F = 0$.

bottom of the trap. Such an energy-selective removal process causes the atoms remaining in the trapped gas to thermalize at a lower temperature. A continuous variation to lower values of ν allows to reach the temperatures required to achieve quantum degeneracy.

The *temperature quench* across the BEC transition is the procedure used to study the KZM in the measurements that will be presented in the following chapters, with the speed of the quench being the main parameter that will be varied while measuring the defect number scaling. Therefore a precise control of the evaporative cooling is crucial in our experiments. Typical RF generators do not meet the requirements of precise frequency timing and fast programming, as we need during the evaporation ramps. In order to overcome these limits we use a system based on a direct digital synthesizer (DDS) and a lookup table (LUT) managed by a microcontroller. The 1024-lines LUT is programmed with the frequencies required for the quench, with the execution timing being managed by the digital system controlling the experiment, which will be described in section 2.3. This configuration allows for flexibility both in time and frequency resolutions.

An example of evaporation frequency ramp is plotted in figure 2.9. The ramp is started just after the transfer of atoms in the MT, with an initial frequency of about 40 MHz. Then the RF is ramped down in a time of 40-60 s to the values where the BEC transition occurs, i. e., just above the trap bottom, whose typical value in our experiments is $\nu_0 \simeq 1.2$ MHz. The speed of the transition crossing can be varied over two orders of magnitude, with a maximum achievable evaporation rate of about 2 MHz s^{-1}. We program the LUT of the DDS in order to have a higher density of frequency values around the transition point, where a continuous-like control of the evaporation is particularly important.

The RF field is irradiated on atoms using an *antenna* driven by the DDS signal after amplification. This antenna is composed of a single

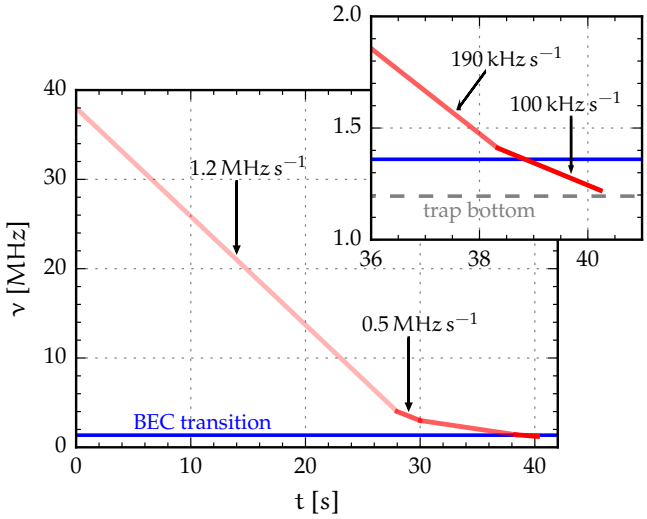

Figure 2.9: Typical frequency ramp used for RF evaporative cooling. The color intensity (red) is proportional to the density of frequency points programmed on the DDS, with each value corresponding to one of the 1024 lines of the LUT. A higher point density is crucial around the BEC transition (solid blue) for a precise control of the quench. The evaporation ramp ends just above the trap bottom (dashed gray).

wire loop, with a radius of 1.3 cm and a wire section diameter of 1 mm. It is placed horizontally above the quartz cell, at a distance of 1.75 cm from atoms. Such an antenna is used for frequencies below 50 MHz, i. e., in the high frequency (HF) band of the spectrum: the antenna relies in the so-called small loop regime, being its circumference much smaller than the RF wavelength. Concerning the near-field regime of our interest for evaporative cooling, these conditions are ideal for producing a sufficiently uniform and strong magnetic field, linearly polarized along the vertical direction‡. Figure 2.10a reports the magnetic component of the radiation pattern, calculated using the NEC2c software considering the geometry of the loop antenna. These numerical simulations also indicate an almost flat antenna response in the frequency range considered for evaporative cooling, being far from any resonance.

The use of RF radiation is not limited to evaporative cooling, but it can be exploited as a general technique for the manipulation of the atomic internal states, and for extracting fractions of atoms from the trapped samples. As an example of this latter possibility, in the experiment reported in the article on the solitonic vortex dynamics (Serafini et al., 2015), we were able to acquire a sequence of images

‡ The transition $|m_F = -1\rangle \rightarrow |m_F = 0\rangle$ exploited during evaporative cooling is coupled by radiation with σ^+ polarization. Considering that the atoms are polarized in the horizontal direction by the magnetic field of the trap, the vertically polarized RF magnetic field can be decomposed into σ^- and σ^+ polarizations.

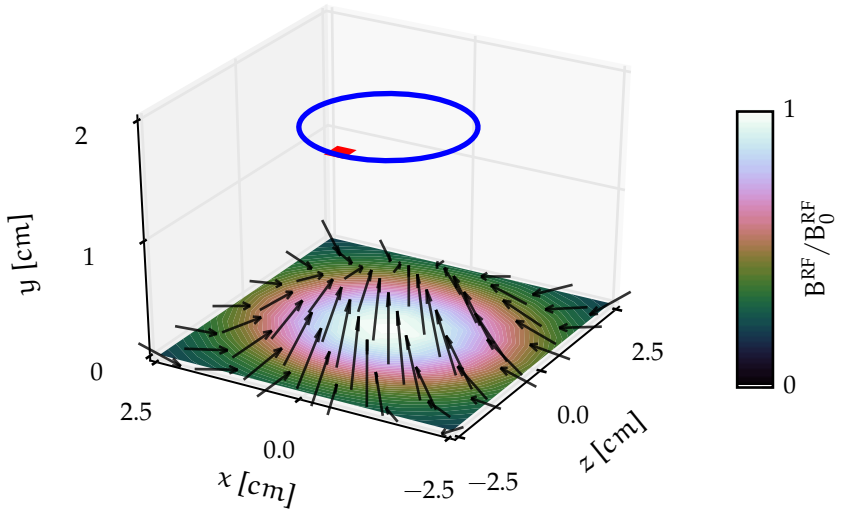

(a) HF loop antenna at 10 MHz.

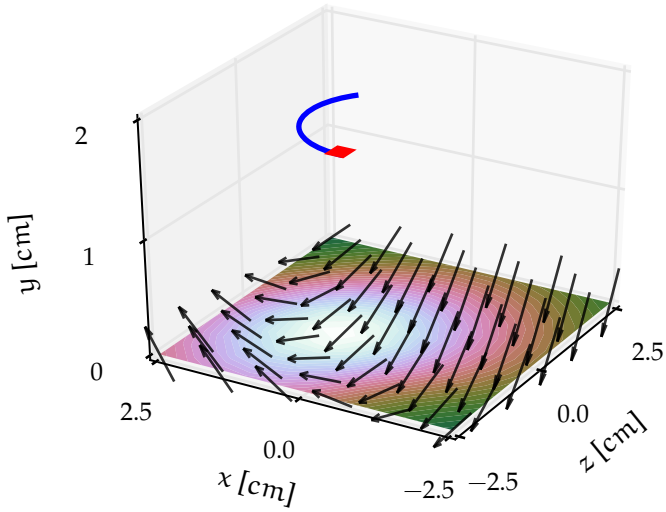

(b) UHF monopole antenna at 1.77 GHz.

Figure 2.10: Magnitude (normalized color scale) and direction (arrows) of the magnetic component of the near-field RF radiation, generated by the antennas used for evaporative cooling and outcoupling at the respective operating frequencies. The pattern is simulated in the horizontal plane, with atoms being trapped in the origin. The antenna (blue) is placed in the horizontal plane at $y = +1.75\,\mathrm{cm}$, and its feed point is indicated in red.

for each condensate performing coherent splitting of the atomic cloud induced by RF radiation. This *outcoupling* technique transfers fractions of atoms in the condensate from the $|F, m_F\rangle = |1, -1\rangle$ trapped state to the $|F, m_F\rangle = |2, -2\rangle$ untrapped state, coupled by a RF field. As it can be seen from the sketch of the atomic levels in figure 2.4, this transition corresponds to a frequency of about 1.77 GHz, i. e., in the ultra-high frequency (UHF) band of the RF spectrum.

Experimentally we found that the loop antenna exploited for evaporative cooling is not suitable for the outcoupling technique just described. The simulations with NEC2c indicate the presence of a resonance phenomenon with phase inversion in the frequency range between 1.5 and 2.0 GHz, where the electrical size of the antenna becomes comparable with the RF half-wavelength, hence possibly explaining its reduced outcoupling efficiency at 1.77 GHz.

Empirically we found that a monopole-like antenna, obtained with a wire forming an arc of circumference over an angle of about 130° and with the same diameter of the original loop antenna, is more efficient in the UHF band of our interest. The numerical simulations confirm that resonances with this geometry occur at higher frequencies, hence not interfering with the near-field pattern that interacts with atoms, whose magnetic component is plotted in figure 2.10b. Since the frequencies in the UHF band are not accessible with the DDSs used in our laboratory, whose maximum operative frequency is about 140 MHz, we drive the UHF antenna with a commercial signal generator (Marconi Instruments 2024), triggered with a transistor-transistor logic (TTL) signal integrated with the system controlling the other instruments.

2.2 PROBING THE ATOMS

2.2.1 Imaging system

The atomic samples are probed using resonant *absorption imaging* (Ketterle et al., 1999). The sequence of the image acquisition begins when the magnetic trapping potential is suddenly switched off, and the atomic cloud starts a ballistic expansion. The consequent free fall of atoms would limit the expansion time to about 50 ms, due to the finite distance of 1.7 cm between the center of the trap and the bottom of the quartz cell. In order to circumvent this limit we set the magnetic trap coils in a levitation configuration. In fact, as introduced in section 2.1.3, we can obtain a vertical magnetic gradient with a suitable current flowing in a single horizontal coil, which produces a force that compensates the gravity allowing very long TOFs, up to hundreds of ms.

The atomic sample is shined with a probe laser beam, and its absorption signal is acquired with a digital camera. The acquisition process is triggered with a TTL signal, which defines the integration time interval. Since the probe light is resonant with the $|F = 2\rangle \rightarrow |F' = 3\rangle$ transition, before the acquisition the atoms in $|F = 1\rangle$ are transferred in the $|F = 2\rangle$ state with optical pumping. A second image acquisition is performed without atoms in order to get a reference, allowing to reconstruct the net optical density profile of the atomic cloud. Using different cameras we can take pictures simultaneously along different directions.

We use charge-coupled device (CCD) cameras (STINGRAY F-201B) having a resolution of 1624×1234 pixels, with a single pixel size of $4.4\,\mu m \times 4.4\,\mu m$. The acquisition rate at full resolution is of 14 frames per second, with the images being transferred to a computer with a FIREWIRE connection. The atoms are imaged on the camera sensor with a set of lenses ensuring a magnification up to 2, hence allowing to resolve structures of about $2\,\mu m$. Essentially this also corresponds to the limit imposed by diffraction in the conditions of our imaging system. Reducing the camera resolution to 300×250 pixels we are able to take faster sequences of images, up to about 50 frames per second. The properties of the atomic sample, specifically the size of the cloud and its optical density, as well as other derived quantities such as temperature and atom number, are extracted from the images using a software written in PYTHON by Gregor Thalhammer, that I partially adapted to our needs.

2.2.2 Image processing

In the following chapters we will present the results of measurements which mainly rely on the observation and characterization of defects in the density profiles of BECs after expansion. Considering the experiments on the KZ scaling, the defects are counted by eye directly in the absorption images, which typically show a high signal-to-noise ratio for bulk condensates in standard conditions.

The situation is different for the real-time imaging technique that we used for studying the defect dynamics (Serafini et al., 2015). In this case the images are taken in a rapid succession for coherent copies of the same condensate, being composed of small fractions of outcoupled atoms, about the 4 % of the trapped sample. These pictures exhibit a much smaller signal-to-noise ratio, as it can be seen from the example in figure 2.11a, which shows a noisy profile containing a defect that is hardly distinguishable. In fact, the presence of thermal noise in the atomic signal and of fringes, caused either by optical or electrical interferences, partially hides the information that can be of our interest. Moreover the limited dynamic range of the image suppresses the visibility of small signals.

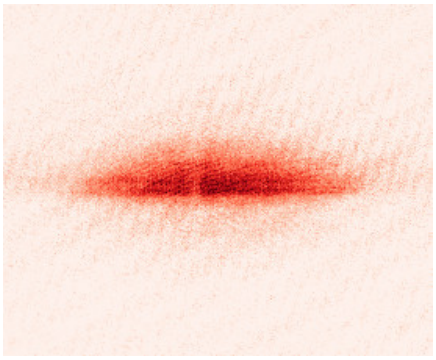

(a) Raw image taken with CCD camera.

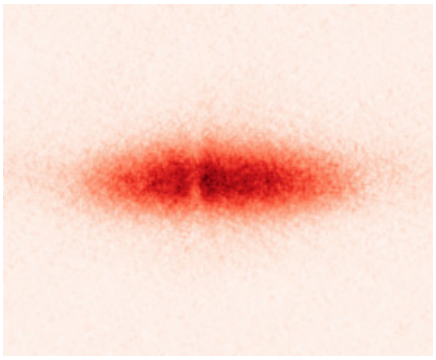

(b) Image filtered from interferences.

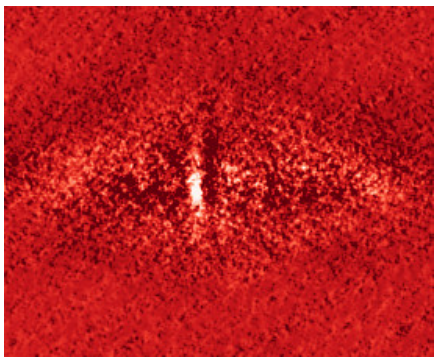

(c) Residuals of Gaussian-parabolic fit.

Figure 2.11: Sample experimental image for a fraction of atoms outcoupled from a condensate, which contains a defect visible as a shallow depletion in the density profile. The image, taken after an expansion of 13 ms, is processed with the FFT filtering software described in the text in order to magnify the defect visibility. The respective FFT space is reported in figure 2.12.

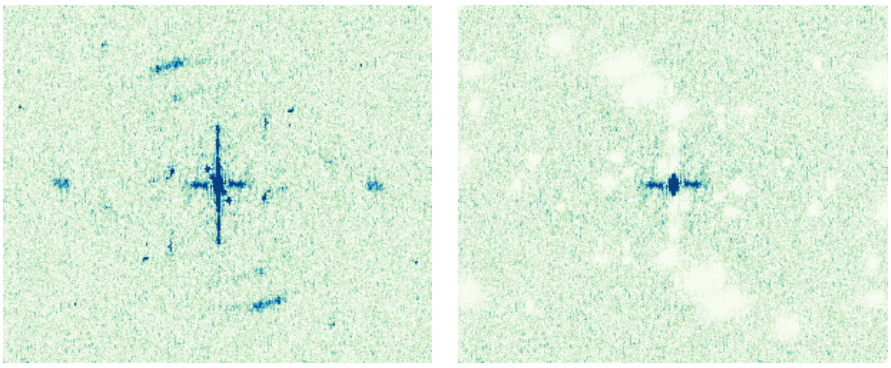

(a) Original FFT of figure 2.11a.

(b) Masked FFT spectrum relative to figure 2.11b.

Figure 2.12: Example of FFT filtering aimed to the removal of the interference fringes and other spurious signals, referring to the experimental image of figure 2.11.

In order to overcome the limitations set by the imaging acquisition system just described, I wrote a software in PYTHON 2.7 which helps in the extraction of defect signals in BECs with *digital filtering* techniques. It relies on the SCYPY package for the numerical analysis and image rendering, performed with NUMPY and MATPLOTLIB respectively. The PYQT library is used for the realization of the graphical user interface (GUI), which allows to easily analyze sequences of experimental images.

The first step of the image processing is aimed to the removal of the *interference fringes*. The image is transformed to the Fourier space with a 2D FFT algorithm. Being the fringes periodical signals, they appear as peaks in the FFT space, as it can be seen from figure 2.12: once identified, a mask for these peaks can be created using the mouse in order to filter out the correspondent signals. A screenshot of the interface is reported in figure 2.13. The software plots interactively the result of the inversion of the masked FFT, hence creating a clearer image in the real space. A Gaussian filter can also be applied for the reduction of the high-frequency noise. Since defects represent nonperiodic signals, in general the removal of single FFT peaks does not affect the strength of defect signals, which conversely appear with better signal-to-noise ratios.

As a further step we can fit the atomic profile with a suitable 2D function, e. g., a Gaussian or an inverted parabola. The software can plot the residual image of the fit: since defects represent deviations from a smooth atomic distribution, their visibility is highly improved in the residuals. The fit residuals of the filtered image in figure 2.11b are reported in figure 2.11c. It is evident how a defect, hardly visible in the original image of figure 2.11a, is clearly distinguishable in the final processed image, with the dynamic range of the image being enhanced by a factor of about 4.

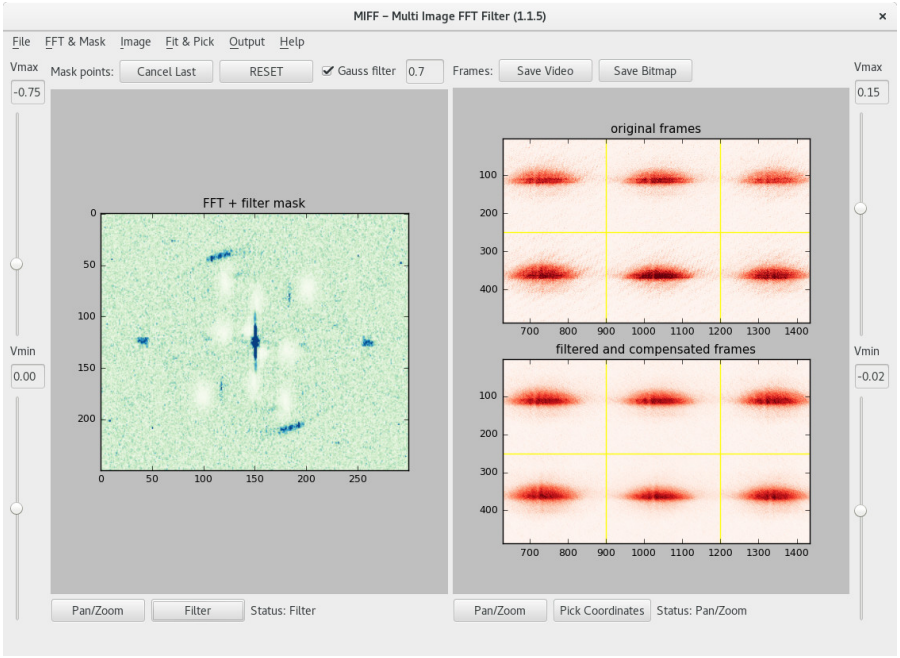

Figure 2.13: Screenshot of the software GUI used to filter and render sequences of experimental images. The original frames (top right) are transformed in the FFT space (left). Masks can be applied to the FFT in order to filter out the fringes. The results of FFT inversion are rendered interactively (bottom right). Other features include color scale adjustments, residuals of fitting functions, and filtering of shot noise.

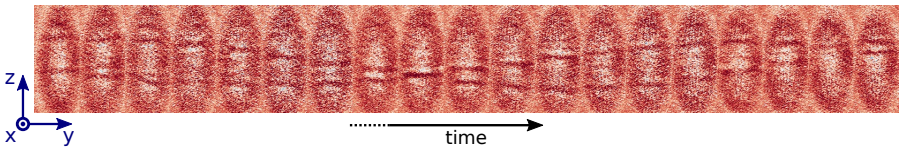

Figure 2.14: Series of filtered images of the same BEC taken every 28 ms with non-destructive imaging (Serafini et al., 2015). The sequence allows to follow the motion of two defects in the condensate.

As previously introduced, the CCD cameras can be configured for taking sequences of several images in a rapid temporal succession. In order to simplify the application of the filtering procedure to series of pictures acquired in similar experimental conditions, the image analysis software allows to automatically process all the images of the sequence using the same parameters, adjusting the color palettes and compensating for variations in the atomic signals in order to obtain an optimal and uniform visibility, as in figure 2.14. Other functions of the software are also present, such as the possibility to track the positions of defects in the condensate and to render the sequence of images as a smooth video, useful for a qualitative comprehension of the defect dynamics.

2.3 CONTROL OF THE EXPERIMENT

2.3.1 Digital control system

The experiments performed with the apparatus described so far require a high degree of control over many different instruments. The experimental procedure for the production of a condensate, from laser cooling to imaging, can be composed of thousands of instructions that must be executed with a timing precision better than 1 µs in some cases, and that must be reproducible with reliability.

Most of the instruments in our laboratory are controlled with a unified *digital control system* based on a field-programmable gate array (FPGA), which was developed by Marco Prevedelli and successively adapted to our needs. The central FPGA (XILINX SPARTAN XC3S250E, clocked at 10 MHz) receives the temporal sequence of instructions to be executed from a computer software, which will be described in section 2.3.2, through a Universal Serial Bus (USB) connection. Each instruction has a target slave board, identified by a univocal address. The FPGA writes the instructions on a 24-bit bus with a resolution in time of 100 ns and with a maximum instruction rate of 2.5 MHz. All the slave boards are connected to a common bus, and each board reads and executes only the instructions corresponding to its address.

In order to control all the parts of our experimental setup we need about 50 digital lines, 30 RF sources and 15 analog sources, which are provided by three kinds of dedicated slave boards.

DIGITAL BOARDS Each digital board can output 16 independent TTL channels. The digital lines are used mainly for setting the magnetic field configuration, by opening or closing the IGBTs and relay switches, and to trigger the image acquisition. The digital outputs are also exploited for moving mirrors and mechanical shutters for the optical beams, using a system that I developed during my master thesis based on microcontrollers and servo motors (Donadello, 2012).

ANALOG BOARDS These boards mount two 16-bit digital-to-analog converter (DAC) chips. The output analog voltages can be either referred to ground or floating. They are used to program the power supplies which provide the currents flowing in the coils for the generation of magnetic fields, and for a smooth control of the IGBT switches.

RF BOARDS The programmable RF signals are generated with boards equipped with a DDS chip (Analog Devices AD9958), based on a 10-bit DAC with two output channels. Each channel can have independent settings for frequency (ranging from about 200 kHz to 140 MHz with a 32-bit resolution), amplitude (up to +13 dBm) and phase. A microcontroller (PIC18F2550) programs the DDS reading the parameters from a LUT. The signals of the DDS boards are amplified and used to drive the AOMs for the optical beams and the antenna for the RF evaporative cooling.

The number of slave boards exploited in our experiments grew with the development of the setup, with the need of always longer bus connections between the boards. This created some problems in the reliability of the communication between the parts of the control system. In fact the bus is composed of 64 parallel unshielded wires: when the length increases over a couple of meters, effects of cross-talk between adjacent channels, of noise pick-up, and of too big capacitive load become evident. In order to circumvent these problems the control system is divided into different parts, each one with an independent FPGA and bus placed in different locations of the laboratory, hence keeping the cable connections short.

However, since the communication via USB between the computer and the FPGA does not happen in real time, without further refinements this solution would introduce a time jitter of many tens of ms between the different parts. This would be incompatible for an experiment in atomic physics. The solution was found by using a single clock source distributed to all the FPGAs, triggering their startup with a single signal emitted once the USB communication is entirely completed. This is done with a system that I developed with a ATmega328

microcontroller. With this approach we are able to keep the nominal resolution of 100 ns with negligible jitter, even in such a distributed system.

2.3.2 Software for the control system

The FPGAs of the system controlling the several slave boards must be programmed using a computer software. During the experiments the experimentalists have to define series of instructions, which must be translated into the specific format of the FPGA firmware and subsequently sent to the hardware via a USB serial connection. For this purpose we initially used a LabVIEW software that was already available at the beginning of our experience in the laboratory, but which showed some limits during the development of the setup. As an example, that software did not allowed for a stable communication with the different FPGAs, and it was not able to manage the execution of repetitive series of instructions as required in many experiments.

Since the implementation of new features in the original software was not easy due to the complexity of its structure, I wrote a new *control software* meeting the requirements of usability, flexibility and stability, hence facilitating the interaction with the instruments of the laboratory independently of their technical implementation. In particular this new software allows to manage complex experimental sequences, introducing the possibility to perform automatic iterations of parametrized procedures over different experimental variables.

The control software currently used in the laboratory is entirely written in Python 2.7. It is composed of more than 3000 lines of code and, even if it was developed under Linux, it is platform independent. It relies on open-source libraries such as NumPy for numerical calculations and Matplotlib for plotting. The PyQt library is used for the realization of the GUI, while the library Libftdi ensures a stable communication with the FPGAs. The software can be divided into two main parts.

KERNEL The core of the software translates the user instructions into the binary format that can be interpreted by the FPGA. This kernel is implemented following a object-oriented scheme in pure Python language. This approach allows for a simple and clear definition of abstract structures for boards (e. g., digital, RF and analog boards) and actions (e. g., variations in the states of TTL channels, DDS frequencies and amplitudes, or DAC voltages).

INTERFACE Typically the users do not interact directly with the kernel, but with a GUI which allows for an easier access to the various functions of the software. As it can be seen from the screenshot in figure 2.15, the interface allows to manage lists of actions, called programs, using a tabular form where the exe-

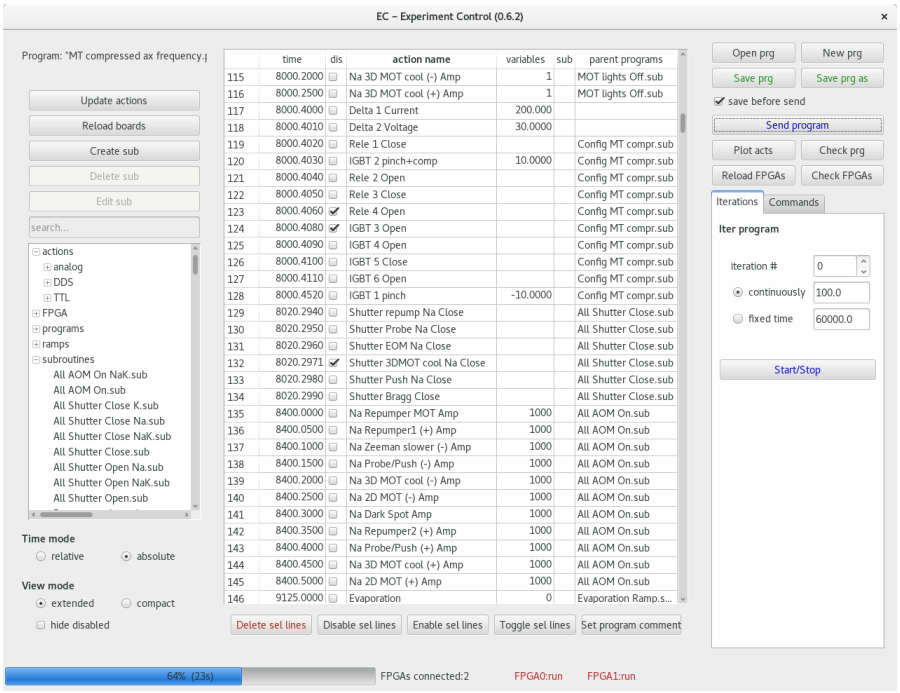

Figure 2.15: Screenshot of the GUI for the experiment control software written in PYTHON, running a sample program of experimental instructions. Each line of the central table corresponds to an instruction or to a nested sub-program, and if needed it can be temporarily disabled and excluded from the execution flow. The columns report the execution time, the action name, and other eventual parameters.

cution time of actions and other parameters can be directly set. The programs are subsequently translated and stored into standard PYTHON files.

Thanks to its implementation the kernel results to be both robust and flexible, while keeping the possibility to be easily maintained and expanded in future. In fact it works independently of the specific hardware, and if required it can be adapted to new boards or instruments. The kernel checks for possible user errors and conflicts, e. g., producing warnings when different actions overlap in time or when the parameters are incompatible with the hardware specifications. This possibility also takes into account the response time of some slave boards, such as the DDS boards, whose microcontroller takes about 35 µs to load the parameters from a line of the LUT. The kernel is able to start sequences in less than 100 ms, and it can be set to run continuously the same program for hours.

The instructions managed by the control software can be either simple actions, ramps of values, or even nested programs containing other instructions. The implementation of sub-programs allows to interlace several sequences of actions by using positive or negative relative execution times. More advanced features are also present.

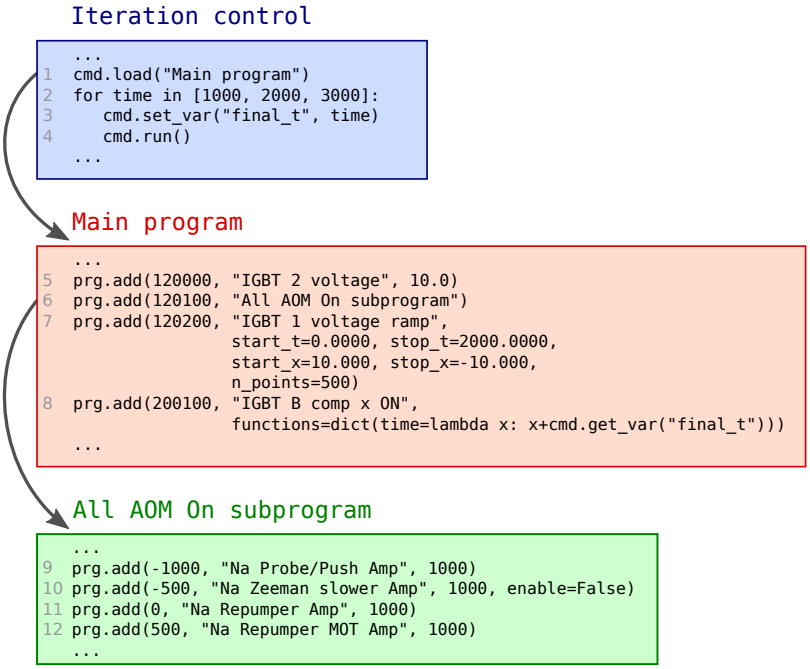

Figure 2.16: Demo code of the control software for some parts of an hypothetical experimental sequence. Line 1 in the iteration control block (top) loads the main program (middle). Each program instruction takes as arguments the execution time (in FPGA clock units), the action name, and eventual parameters (as in instruction 5). Instruction 6 loads a sub-program composed of other instructions (bottom), whose execution times are relative to the absolute time of the main program. Instruction 7 executes a sequence of actions, performing a linear ramp for the parameter of the considered action. Lines 2, 3 and 4 iterate the launch of the main program setting different values of a variable, which specifically applies to the execution time of instruction 8. Instruction 10 is not executed.

These include the possibility to automatize the scan of experimental parameters using variables and conditional statements while iterating parametrized programs, hence allowing to perform long and repetitive data acquisitions without requiring any user interaction. Figure 2.16 sketches the native PYTHON code interpreted by the control software for a demo experimental sequence, containing a nested program and being iterated over different values of a given variable.

The software performs automatic incremental backups of programs and settings, allowing to reconstruct the history of experiments if needed. In order to debug the experimental procedure, the temporal sequence of the instructions of a program can also be visualized in a graphical way, as it can be seen from figure 2.17. Finally the kernel and the interface are designed in such a way that they can be executed independently, even on different computers, possibly expanding the applications of the software. As an example, this allows for the inte-

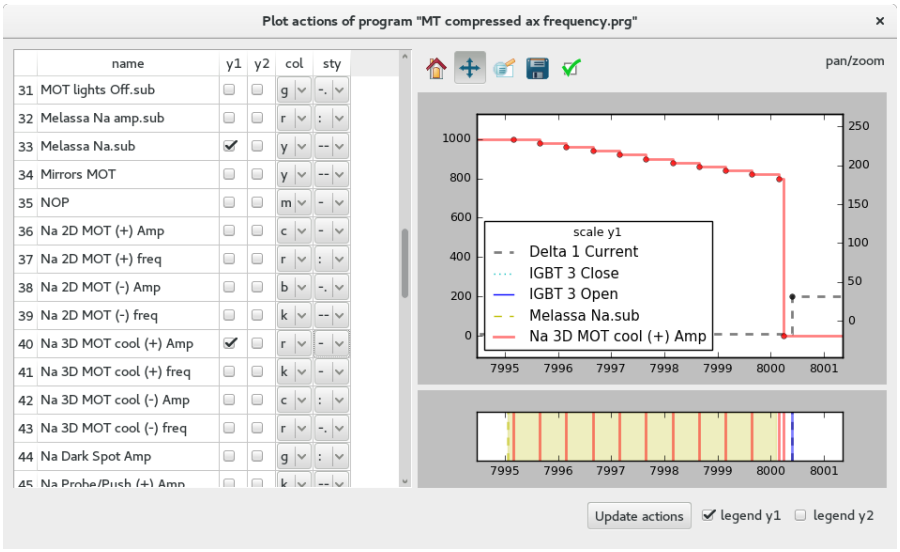

Figure 2.17: Graphical visualization of a demo sequence of actions plotted by the control software as a function of time. In this example the plot reports the variations of a DDS amplitude, of an analog voltage, of a TTL line, and the execution of a sub-program (shadowed in the lower plot).

gration of the kernel in standalone scripts or other programs. Another possibility is to leave the kernel running on a computer directly connected to the FPGAs in the laboratory, while executing the GUI from somewhere else, hence accessing remotely to the experimental apparatus via a standard network connection.

3 SPONTANEOUS DEFECT CREATION IN A BEC

The Kibble–Zurek theory describes the universal phenomenon of formation of phase defects occurring when a system is quenched across a second-order phase transition. This mechanism has been observed in many different systems, from condensed matter to ultracold dilute gases. In this chapter I will report the measurement in BECs of the defect number scaling with the temperature quench rate, the first ever done in such kinds of systems, and realized in the laboratory of ultracold gases in Trento.

The observation of defects spontaneously created in condensates via the KZM after temperature quenches is reported in section 3.1. In section 3.2 I will describe how we image our BECs of sodium for the detection of defects. The characterization of the number of defects as a function of the quench parameters will be reported in section 3.3. In section 3.4 I will present a toy model that deals with the KZM in the presence of inhomogeneities related to the trapping potential. Finally in section 3.5 I will talk about the observation of a finite defect lifetime, which inspired the subsequent studies that will be presented in chapters 4 and 5.

3.1 OBSERVATION OF DEFECTS

Following a phase of laser trapping and cooling in the MOT, we transfer the atoms in an axially symmetric harmonic magnetic trap. Subsequently the atomic samples are cooled down with forced RF evaporative cooling. During the evaporation we decompress the trap potential by a factor of $\sqrt{2}$ to the final axial and radial trapping frequencies, $\frac{\omega_\parallel}{2\pi} = 13\,\mathrm{Hz}$ and $\frac{\omega_\perp}{2\pi} = 131\,\mathrm{Hz}$ respectively, hence with an aspect ratio of about 10. Just above the BEC transition point, which typically occurs around 800 nK, we have about 25×10^6 atoms. At the end of the evaporation ramp we obtain about 10×10^6 atoms in the final cigar-shaped condensate.

While we were optimizing the evaporative cooling parameters for the condensation, we occasionally observed unexpected structures in the density profiles of the BECs after free expansion: some depletion lines were visible in the experimental pictures taken along the horizontal radial direction, as in the examples of figure 3.1. The number of those lines was random, ranging from zero for regular condensates, up to a few units. They seemed to be oriented mostly perpendicular to the trap axis, and showed random positions in the BEC. As a

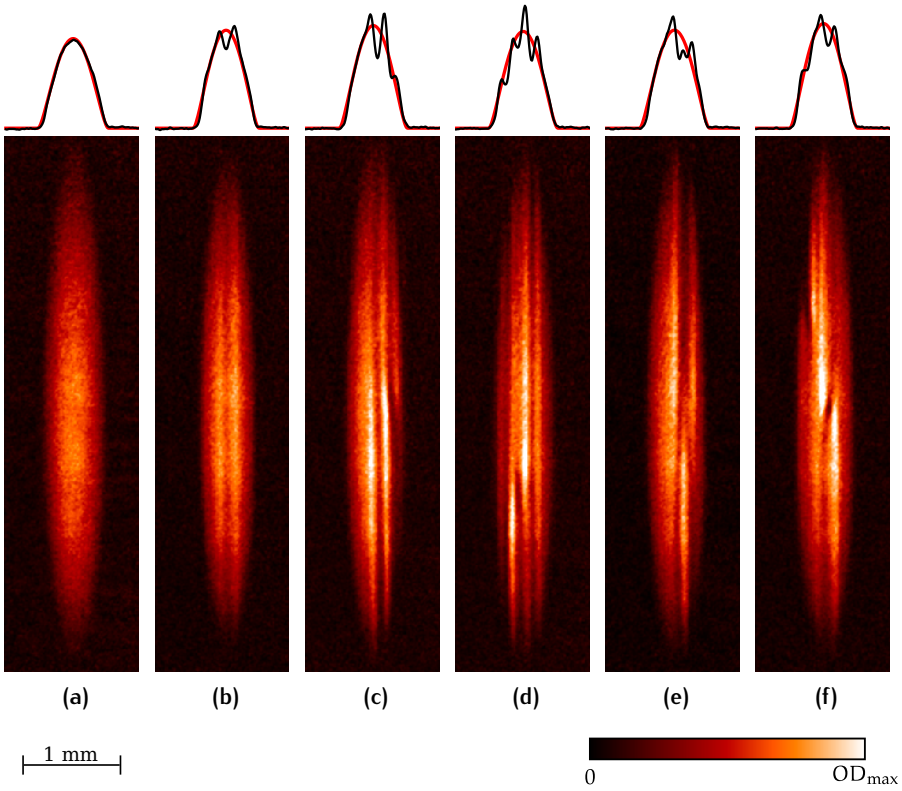

Figure 3.1: Absorption images of condensates observed along the horizontal radial direction, containing a variable number of linear defects. In order we count from 0 to 3 defects (a-d), while the last two pictures (e-f) show more intricate structures. These images are taken after 180 ms of free expansion with the tomographic technique described in the text. On the top of each picture the density profile integrated along the vertical direction (black) is compared with the respective parabolic fit (red), highlighting the density dips of defects. The color scale is normalized to the maximum optical density, which is of the order of 1.

first step we checked if those irregularities were just technical artifacts of the imaging acquisition or if they were the sign of some kind of physical phenomenon happening in the condensate. As it will be described in section 3.2, the simultaneous observation of those structures in the condensates along different directions supported the idea that we were looking at *defects* actually present in the atomic density distribution.

Another important observation was that the presence of defects was more probable when the BEC transition was crossed with faster evaporative cooling ramps. This link between the defect probability and the cooling speed suggested us that our observations might be interpreted in the context of the Kibble–Zurek mechanism (KZM), which predicts the creation of phase defects after fast quenches while crossing a second-order phase transition. This possibility was particularly

interesting since Bose–Einstein condensation in dilute gases was previously considered as an ideal environment for the study of the KZ theory (Kibble, 2007; Zurek, 2009; del Campo et al., 2011), thanks to the high degree of experimental control available with ultracold atoms. Moreover the spontaneous formation of vortices in oblate BECs after fast temperature quenches was already described by Weiler et al. (2008), but a similar observation in elongated systems, as well as the power-law scaling of the defect number as predicted for the KZM, was never reported before.

3.2 IMAGING OF PLANAR DEFECTS

In order to study and characterize the defects appearing in the condensate we adapted the image acquisition for the optimization of the defect visibility. The imaging procedure starts when the trap is suddenly switched off. As illustrated in figure 3.2, the released condensate mainly expands along the tightly confined radial direction, and the cigar-shaped cloud inverts its aspect ratio and turns into a pancake-shaped distribution (Castin et al., 1996; Ernst et al., 1998). During the free expansion we compensate the gravity force with a vertical magnetic field gradient. As introduced in section 2.2.1, thanks to this *levitation technique* we can overcome the limit of about 50 ms that would be imposed by the physical size of the quartz cell of the vacuum chamber during the free fall starting from the center of the trap, hence allowing expansions much longer than ordinary TOFs.

We found that an optimal visibility of defects is achievable with an expansion of 180 ms. For such a long TOF the optical density of the condensate is always below 2, thus the images acquired with the CCD camera are not affected by saturation and we are able to appreciate smaller density variations. The observation of the condensate along a single radial direction gives only a partial knowledge about the geometry of defects: the 3D structure of a defect cannot be fully reconstructed from the atomic density integrated along the direction of observation. More information can be deduced if the condensate is imaged simultaneously along different directions: in our configuration we take pictures along the vertical and horizontal *radial axes* of the trap, as represented in figure 3.3a.

One interesting observation is that in most cases each linear defect is observed along the two orthogonal radial directions, implying that it can be related to a single structure with a planar geometry perpendicular to the trap symmetry axis: this suggested the initial identification of the depletion lines in images as the nodal planes of *solitons*, seen along a direction parallel to their surface (Lamporesi et al., 2013b). This possibility was also supported by the fact that, in order to minimize their surface and consequently their energy as sug-

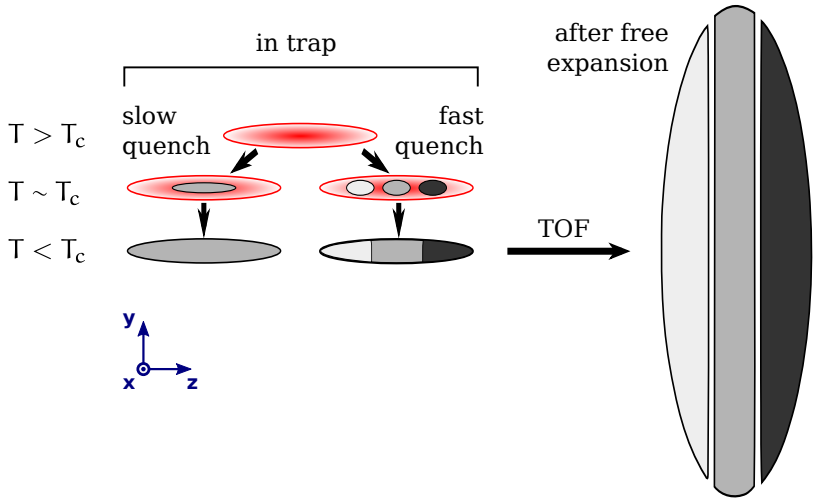

Figure 3.2: On the left the trapped gas is sketched while crossing the BEC transition occurring at the critical temperature T_c. According to the KZM, if the quench is fast enough different independent condensates (gray) can nucleate in the thermal gas (red). When the condensate is released from the trap it expands mainly along the radial directions, i. e., x and y, acquiring a pancake-like shape after long expansion times as represented on the right.

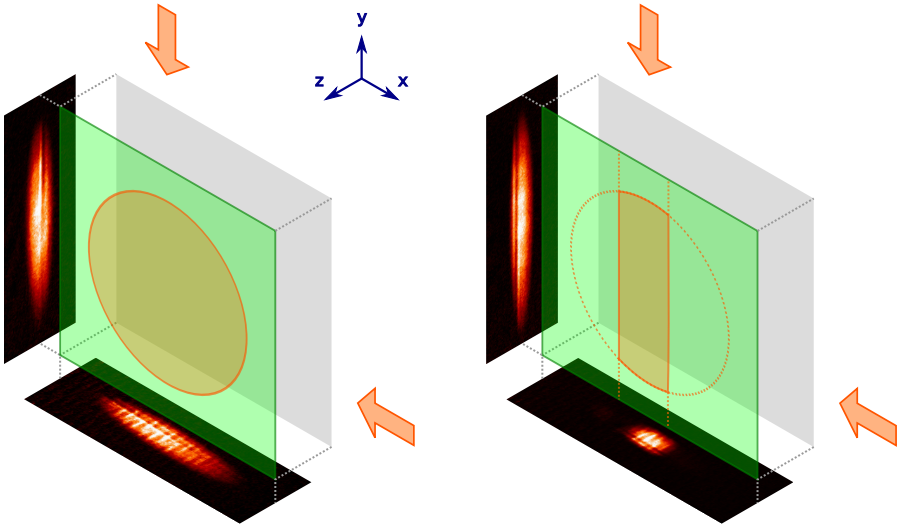

(a) Radial imaging. **(b)** Tomographic imaging.

Figure 3.3: Sketch of our configuration for absorption imaging (left), where pictures of the expanded condensate are taken along two orthogonal radial directions. The orange arrows indicate the directions of the probe light beams, aligned with the plane of main expansion of the condensate (green plane). Possible planar structures perpendicular to the axial direction are seen as depletion lines in both the radial pictures. For the tomographic imaging configuration (right) just a central slice of the condensate is optically pumped in the correct hyperfine state for the absorption imaging, while the rest remains off-resonance and does not contribute to the integrated pictures.

gested by equation (1.48), in elongated BECs solitons tend to assume the favored configuration with their plane perpendicular to the long axis of the cloud, therefore being visible as linear dips in the density profile along any radial direction after expansion. Moreover the creation of gray solitons from independent phase domains formed along the symmetry axis of a cigar-shaped condensate was predicted by Zurek (2009) while studying the KZM in inhomogeneous systems.

As introduced in section 1.3.2, solitons are localized collective excitations of the condensate, characterized by a density depletion whose size is of the order of the healing length, defined in (1.38) as $\xi_l = (8\pi a\rho)^{-1/2}$, where a is the scattering length and ρ is the atomic density. For sodium atoms in the $|F, m_F\rangle = |1, -1\rangle$ state we have $a = 55a_0$, where a_0 is the Bohr radius. In our experimental conditions we expect that the in-trap healing length is of the order of 200 nm. Assuming that ξ_l adiabatically follows the density reduction occurring during the free expansion in the radial plane, after a TOF of 180 ms we expect the healing length to be much larger, of the order of 100 µm, and well above the imaging resolution of about 10 µm. These considerations are in agreement with the experimentally observed defect width. Moreover we can justify why the visibility of defects increases for longer TOFs: after the expansion solitons become bigger and easier to be observed.

Defects have a maximum visibility when the solitonic planes are straight and perpendicular to the trap axis, therefore appearing as sharp lines in the integrated radial images. For this reason the imaging directions have been precisely aligned along the transverse plane of the trap, an important requirement for the observation of planar structures. However, as it can be seen from figure 3.1, we often observe depletion lines that are bent or curved, sometimes crossing and overlapping each other when more defects are present. A tilted plane can appear with a lower contrast in an image taken along a radial direction: in order to increase the visibility of defects, we implemented a *tomographic technique* that allows to reduce the integration interval along the direction of observation.

To explain the working principle of this tomography of the condensate, we recall that absorption imaging is performed using light resonant with the $|F = 2\rangle \rightarrow |F' = 3\rangle$ hyperfine atomic transition. Since the atoms in the magnetic trap are in the $|F = 1\rangle$ state, which is a dark state to the imaging light, before taking the picture we need to transfer the population to the bright state $|F = 2\rangle$, for instance by optical pumping, which in general is performed on the whole sample. We can perform this repumping just on a narrow slice of the expanded atomic cloud, while leaving the rest of the atoms in the dark state that is invisible in images. As illustrated in figure 3.3b, we shine the central part of the condensate, that after an expansion of 180 ms takes the shape of a disk with a radius of about 2.5 mm, using a vertical narrow

repumping light sheet with a waist of 600 µm. Thanks to this tomographic technique the contrast of the depletion lines results higher, and we can identify and count the defects with a better confidence.

3.3 DEFECT NUMBER SCALING

3.3.1 Temperature quenches

The KZM gives a quantitative prediction for the scaling of the number of defects formed after crossing a second-order phase transition with a given quench rate, i. e., the velocity at which the control parameter is varied. In our system the control parameter for the BEC transition is the temperature of the gas, which is indirectly controlled through the RF threshold during the *evaporative cooling* phase. Even if we exploit evaporative cooling to reduce the temperature by about three orders of magnitude during the preparation of the atomic samples and the production of BECs, in the framework of the KZM only the interval around the transition point is relevant.

In order to quantitatively characterize the *defect number scaling* we need to define a procedure which guarantees that the transition is crossed with a given cooling rate $\partial T/\partial t$. By measuring the temperature T as a function of the evaporation frequency ν around the transition point, we found that T scales as ν with a proportionality factor of about $5\,nK\,kHz^{-1}$, which is almost constant with the quench rate. We can therefore assume that the quenches performed with linear evaporation ramps are effectively *linear temperature quenches*, and that $\partial T/\partial t$ at the transition is proportional to the evaporation speed $\partial\nu/\partial t$, which can be controlled in a precise and flexible way with the digital control system of the experiment described in section 2.1.4.

The transition point is experimentally determined by imaging the atomic cloud at different RF values: we find the frequency ν_c that sets the threshold for the presence of a minimal condensed fraction, and we measure the correspondent critical temperature T_c from the Gaussian width of the thermal fraction after ballistic expansion. The critical point ν_c depends on many parameters, such as the quench rate $\partial\nu/\partial t$ and the number of atoms at the transition N_c. We choose to keep N_c as constant as possible, within the shot-to-shot fluctuations of about 20 %, by controlling the number of atoms that are loaded in the MOT at the beginning of each experimental sequence. This allows us to apply the predictions of the KZ theory for the scaling of the defect density directly to the number of defects counted in the BEC. In fact, if the in-trap dimensions of the atomic sample at T_c, fixed by N_c, remain the same, defect density and their absolute number are linked by a constant multiplicative factor which can be neglected in the subsequent analysis on the defect number scaling.

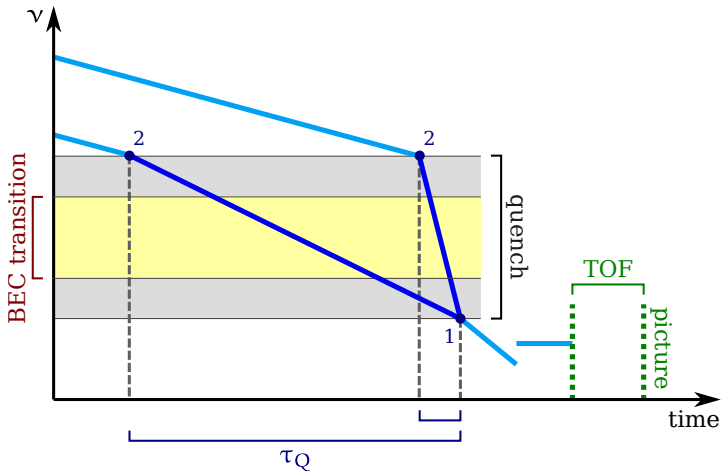

Figure 3.4: We use a common RF evaporative cooling procedure to prepare all the cold atomic samples above the critical temperature T_c (point 2). The transition occurs in a frequency interval depending on the experimental parameters (yellow). The transition point is crossed with a linear frequency ramp that ends below T_c, performed in a time τ_Q depending on the variable frequency rate (from point 2 to 1). After the quench an additional cooling ramp increases the condensed atomic fraction in 100 ms. A fixed waiting time of 100 ms is waited keeping a RF shield, before the atoms are released from the trap and imaged after 180 ms of TOF.

We define the quench as a linear evaporation ramp with variable slope $\partial\nu/\partial t$ between the fixed RF limits $\nu_2 = 1.39\,\mathrm{MHz}$ and $\nu_1 = 1.25\,\mathrm{MHz}$, since we observed that the transition frequency ν_c lies within this range for every quench rate that has been experimentally explored. Following these considerations, we can define the *quench time* τ_Q, that was introduced in equation (1.12), as the duration of the linear quench ramp over the frequency interval $\Delta\nu = \nu_2 - \nu_1 = 140\,\mathrm{kHz}$ around the transition*:

$$\tau_Q = \frac{\Delta\nu}{\partial\nu/\partial t} \propto \left(\frac{\partial T}{\partial t}\right)^{-1} . \tag{3.1}$$

As it can be seen also from figure 3.4, smaller values of τ_Q correspond to faster quenches and vice versa.

At the end of the quench ramp, i. e., at ν_1, the condensate is not pure and a sizable fraction of atoms remains in the non-condensed state. In absorption images the thermal fraction is visible as a broad background signal, which overlaps with the density profiles of defects in the condensate, reducing their contrast. In order to maximize the visibility of defects, after the quench we reduce the thermal fraction with an additional ramp of 100 ms at a constant slope of $300\,\mathrm{kHz\,s^{-1}}$, hence obtaining for every τ_Q almost pure condensates at 1.22 MHz, which is 25 kHz above the trap bottom at $\nu_0 = 1.195\,\mathrm{MHz}$.

* Note that this definition of τ_Q is partially different from the one that will be presented in section 5.1.1.

After the completion of the evaporation we wait an additional time of 100 ms before taking the picture. This is done in order to allow the stabilization of defects and the thermalization of the condensate also for the fastest ramps: in fact we note that the temperature stabilizes some tens of ms after the quench. During this waiting time we also observe that the temperature of the atomic sample rises by more than 100 nK from its final value of about 200 nK: in order avoid this heating process, during the waiting time we keep the evaporation frequency at the constant value of 1.24 MHz, hence introducing a RF shield and continuously removing from the sample the thermal atoms with higher energies.

3.3.2 Defect number counting

After the quench procedure is completed we probe the condensate with tomographic absorption imaging along the horizontal radial direction, as described in section 3.2. Then we count by eye the number of depletion lines that are visible in the density profile of the BEC, as in the examples of figure 3.1, hence associating a number of defects N to each experimental run. We expect N to follow a *Poisson statistics*:

- for each shot we measure an integer number of defects N, typically ranging from 0 to 5;
- the number N is random and independent shot-to-shot, as we expect from the stochastic nature of the KZM;
- due to the low density of defects, it is unlikely to find more than one defect at the same position;
- since the dimensions of the atomic cloud at the transition are almost constant, the probability to find N defects is simply proportional to the defect density, which is fixed by the KZM.

As it can be seen from figure 3.5, the probability distribution of N is characterized by a higher average when the quench time is smaller, and, in addition, it is well fitted with a Poisson distribution, as it will be discussed also in section 5.3.1.

The meaningful quantity of our interest for the KZM is the *average defect number* $\langle N \rangle$, which is extracted by repeating the experiment M times for each condition of the experimental parameters:

$$\langle N \rangle = \frac{1}{M} \sum_{i=1}^{M} N_i \,. \tag{3.2}$$

The uncertainty over $\langle N \rangle$ is calculated as the sum in quadrature of the standard error of the mean

$$\delta N = \sqrt{\sum_{i=1}^{M} \frac{(N_i - \langle N \rangle)^2}{M(M-1)}} \tag{3.3}$$

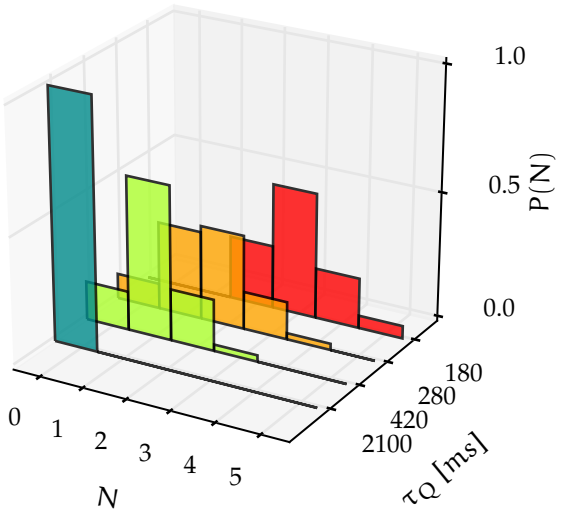

Figure 3.5: Occurrence probability for the number of defects counted in the single experimental runs, considering different values of the quench time: the distribution moves to higher defect numbers for smaller values of τ_Q. The statistics refers to the data set with $N_c = 25 \times 10^6$ atoms of the measurements on defect number scaling reported in figure 3.6.

and of a resolution term estimated as M^{-1}, hence giving a total error bar† of

$$\Delta N = \sqrt{\delta N^2 + \frac{1}{M^2}}\,. \tag{3.4}$$

The number of experimental realizations M is varied between 20 and 40, depending on the resulting average defect number in order to minimize the error bars.

3.3.3 Power-law scaling

We measured the average defect number $\langle N \rangle$ over more than one order of magnitude of the quench time τ_Q, which has been varied between 140 ms (1 MHz s^{-1}) and 2.5 s (60 kHz s^{-1}). The measurement has been repeated for two values of the atom number at the transition, respectively $N_c = 25(5) \times 10^6$ and $N_c = 4(1) \times 10^6$ atoms. The results are reported in figure 3.6. For each series the number of defects decreases with the quench time, and can we identify a threshold value of τ_Q for the detection of defects, shown in the plot with a vertical arrow: above this value of τ_Q we never observe defects. Considering the series with higher N_c, from the plot in logarithmic scale

† In this chapter we report the uncertainties as in our first article on the KZM (Lamporesi et al., 2013b). However the resolution term M^{-1} is underestimated here, as it will be discussed in section 5.1.4.

along both vertical and horizontal axes, it is evident that the average defect number $\langle N \rangle$ scales with the quench time τ_Q as a *power law*, as predicted by the KZM. This strongly supports our hypothesis about the origin of defects in our system.

For fast quenches our measurements are limited by atom loss at the end of the evaporation ramp, caused by the reduced evaporative cooling efficiency. In fact, considering the series with $N_c = 25 \times 10^6$ atoms at the transition, for $\tau_Q \lesssim 140\,\mathrm{ms}$ the number of atoms in the final condensate significantly drops compared to its average value of 10×10^6 atoms. We discard these experimental data, since a significant variation of the condensate size may alter the number of defects that are visible. For the same reason the series with $N_c = 4 \times 10^6$ atoms was performed on a reduced interval of the quench time: the atom loss becomes important already for values of τ_Q smaller than about 1 s.

The average defect number as a function of the quench time has been fitted with a power law, following the expression in equation (1.25) introduced for the KZ scaling:

$$N(\tau_Q) \propto \tau_Q^{-\alpha}\,. \tag{3.5}$$

For the series with higher atom number we measure an exponent $\alpha = 1.38(6)$‡. A similar power-law fit has not been possible for the series with $N_c = 4 \times 10^6$ atoms, because of the reduced set of data points. Moreover we observe an unexpected abrupt change in the power-law slope at large τ_Q values, which further limits the available interval. However a qualitative comparison between the points at smaller τ_Q seems to indicate a similar power-law behavior between the two series. If confirmed, this would suggest a universal behavior for the defect number scaling, independent on the properties of the system and in accordance with the KZM.

A comparison of these experimental results with the KZ theory is not straightforward for several reasons that can be evinced from the discussion done for equation (1.26). First of all the power-law exponent α depends on the critical exponents ν and z: different theories predict different values of ν and z, and the topic is still debated (Donner et al., 2007; Chomaz et al., 2015; Navon et al., 2015). Moreover α depends on the defect dimensionality: as described in section 3.2, a preliminary identification of our defects was made in terms of solitons. However, as it will be presented in chapter 4, subsequent studies led us to identify these defects as solitonic vortices, which may have a different dimensionality: according to the KZ theory the power-law exponent α changes by a factor of 2 between solitons and vortices in 3D systems, and therefore a clear knowledge of the defect nature plays a crucial role in this kind of measurements.

‡ The uncertainty over α reported here is the asymptotic standard error. It neglects possible systematic and resolution errors.

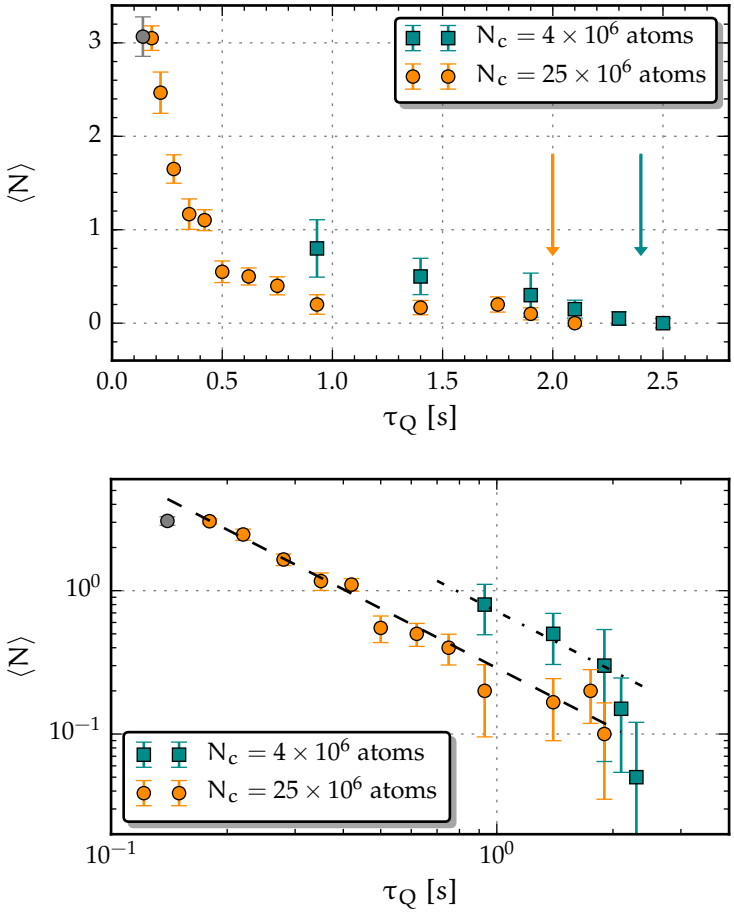

Figure 3.6: Average number of defects as a function of the quench time for two series taken with different atom numbers at the BEC transition, reported in linear (top) and log-log (bottom) scales. For each data set the arrow indicates the value of τ_Q setting the threshold for the detection of defects. The set with $N_c = 25 \times 10^6$ atoms is fitted with a power law (dashed line) as defined in equation (3.5), excluding the fastest point where the number of condensed atoms is significantly smaller. The best fit to the data provides an exponent $\alpha = 1.38(6)$. The dot-dashed line is not a fit: it is a power law with the same exponent α, shifted upward in order to overlap the series with $N_c = 4 \times 10^6$ atoms, and it is plotted only for comparison.

Within the limits discussed above, the calculations for gray solitons produced via the KZM in a cigar-shaped condensate give a power-law exponent of $\alpha = 7/6 \simeq 1.2$ (Zurek, 2009), considering the critical exponents from the F-model (Hohenberg et al., 1977) and assuming the BEC transition to be in the same universality class of the superfluid transition in ^{4}He. Even if the measured exponent $\alpha \simeq 1.4$ is of the same order of magnitude, a direct comparison cannot be done since the theory assumes a constant temperature in the condensate, while this condition may not be met in our system as it will be discussed in the following section.

3.4 ROLE OF THE INHOMOGENEITY

3.4.1 Model for the inhomogeneous BEC

In section 1.2.2 we discussed the condition for the formation of independent phase domains in inhomogeneous systems, which translates into the comparison between the velocity of the transition front v_F and the speed setting the causal horizon $\hat{v}$, introduced in equations (1.22) and (1.23) respectively: phase defects can form when $v_F > \hat{v}$, hence when the transition is so fast that the order parameter must be chosen locally. Here we present a simple model that was proposed in order to check if this condition can apply to our system (Lamporesi et al., 2013b), eventually supporting the interpretation of our experimental results within the KZM framework.

The atoms are confined in an axially symmetric harmonic potential that, following equation (1.39), can be expressed in cylindrical coordinates as

$$U(r,z) = \frac{1}{2}m\left(\omega_\perp^2 r^2 + \omega_\parallel^2 z^2\right), \tag{3.6}$$

where $r^2 = x^2 + y^2$. The elongated profile of the trapping potential is sketched in figure 3.7. As previously described, we perform temperature quenches through the BEC transition using RF evaporative cooling: the frequency ν sets the evaporation threshold at a given potential energy from the trap bottom in $r = z = 0$, thus mapping the potential depth as

$$E_{ev} = h\nu - U(r,z)\,. \tag{3.7}$$

The thermalization properties of the gas depend both on the confinement regime and on the elastic collisional time, which, in our experimental conditions at the BEC transition, in the center of the trap is of the order of

$$\tau_{coll} = \frac{1}{\rho_0 \sigma_{coll} v_T} \simeq 10\,\text{ms}\,. \tag{3.8}$$

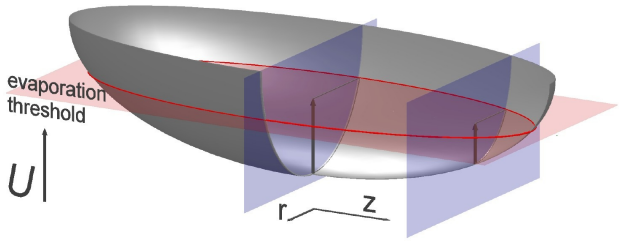

Figure 3.7: Sketch of the elongated trapping potential (gray), with the RF setting the evaporation threshold (horizontal red plane). During the quench the threshold is linearly reduced at a given quench rate. We assume the thermal equilibrium along the radial direction, with an inhomogeneous temperature depending on the axial position z.

Here ρ_0 is the peak atomic density, $\sigma_{coll} = 8\pi a^2$ is the elastic collisional cross section with a being the scattering length, and v_T is the thermal velocity of the gas at $T = T_c$ (Arndt et al., 1997). From the comparison of τ_{coll} with the radial and axial oscillation periods, respectively $\frac{2\pi}{\omega_\perp} \simeq 8\,ms$ and $\frac{2\pi}{\omega_\parallel} \simeq 80\,ms$, in first approximation we can assume to be in an axial collisional regime (Ketterle et al., 1999): around the transition we expect a local thermal equilibrium in the gas, with a temperature gradient along the axial direction.

It follows that, for a given radio frequency ν, during the evaporation quench the *local temperature* of the gas can be expressed as a function of the axial position z, neglecting the radial dependence:

$$T(z) \simeq \frac{E_{ev}}{\eta k_B} = \frac{h\nu - U(r=0,z)}{\eta k_B}. \tag{3.9}$$

Here η is the evaporation truncation parameter, i. e., the factor setting the proportionality between the trap depth and the gas temperature (Ketterle et al., 1996a). In our case $\eta \simeq 11$, as it will be discussed in section 5.1.3.

Along the trap axis, at thermal equilibrium the local atomic density above the critical point can be expressed as

$$\rho(z) = \rho_0 \exp\left(\frac{-U(r=0,z)}{k_B T}\right), \tag{3.10}$$

where T is the equilibrium temperature and ρ_0 the peak density in the center. The *critical temperature* of the BEC transition can be estimated by inserting $\rho(z)$ in the expression for non-interacting particles, introduced in equation (1.29):

$$T_c(z) \simeq \frac{2\pi\hbar^2}{m k_B}\left(\frac{\rho(z)}{2.61}\right)^{2/3}. \tag{3.11}$$

The profiles of the transition evaporation frequency $\nu_c(z)$ and of the critical temperature $T_c(z)$, estimated for our experimental conditions with $N_c = 25 \times 10^6$ atoms, are reported respectively in the

upper and middle plots of figure 3.8. The same plots report also the temperature profiles of $T(z)$ calculated for three sample values of the evaporation threshold ν. From the comparison between $T(z)$ and $T_c(z)$ we can identify the *transition front*, located at the position that satisfies $T(z) = T_c(z)$. Considering a linear variation of the evaporation frequency ν, the transition front will propagate starting from the center of the trap, with a velocity v_F that depends on the axial position z and on the quench time τ_Q.

The front velocity v_F has to be compared with the speed $\hat{v}$ that sets the causality limit, i. e., the maximum velocity at which the information about the choice of the order parameter travels across the gas. In first approximation, within the two-fluid model we can consider the speed of first sound for the causal horizon of the gas undergoing the condensation. A precise calculation of this quantity at the transition is highly nontrivial. However, for a weakly interacting gas, we can roughly estimate the speed of first sound at T_c with the ordinary *speed of sound* in an ideal gas (Pitaevskii et al., 2016), which scales as

$$v_s(z) \propto \sqrt{\frac{k_B T_c(z)}{m}}\,. \tag{3.12}$$

From the comparison between v_F and v_s in the lower plot of figure 3.8, we can see that within the trapped inhomogeneous gas there are regions where the transition front moves faster than sound, i. e., where the nucleation of independent phase domains may occur. We can also observe that these regions where the KZM should be active are wider for faster quenches, in accordance with the observation of higher defect numbers for smaller τ_Q values.

Even if the strong assumptions that we have done here should be treated deeper, this simple model supports the interpretation of our observations with the KZM. However, it also puts some concerns about a quantitative comparison between our experimental results and the predictions of the KZ theory for inhomogeneous systems. In fact, the power law and respective exponent α reported in equations (1.25) and (1.26b) refer to calculations done by Zurek (2009) in the assumption of a uniform temperature in the gas, whereas, as just discussed, in our experimental conditions we expect a non-uniform temperature during the quench. The difference can be appreciated from figure 3.8, where the speed of the transition front at a given τ_Q is plotted considering both uniform and inhomogeneous gas temperatures. If we neglect the outer part of the atomic cloud where the density is vanishingly small, for a uniform temperature the condition $v_F > v_s$ is verified only within a narrow region near the center of the trap. This means that the calculations with an inhomogeneous temperature may lead to a different number of defects, and in particular to a different power-law exponent α.

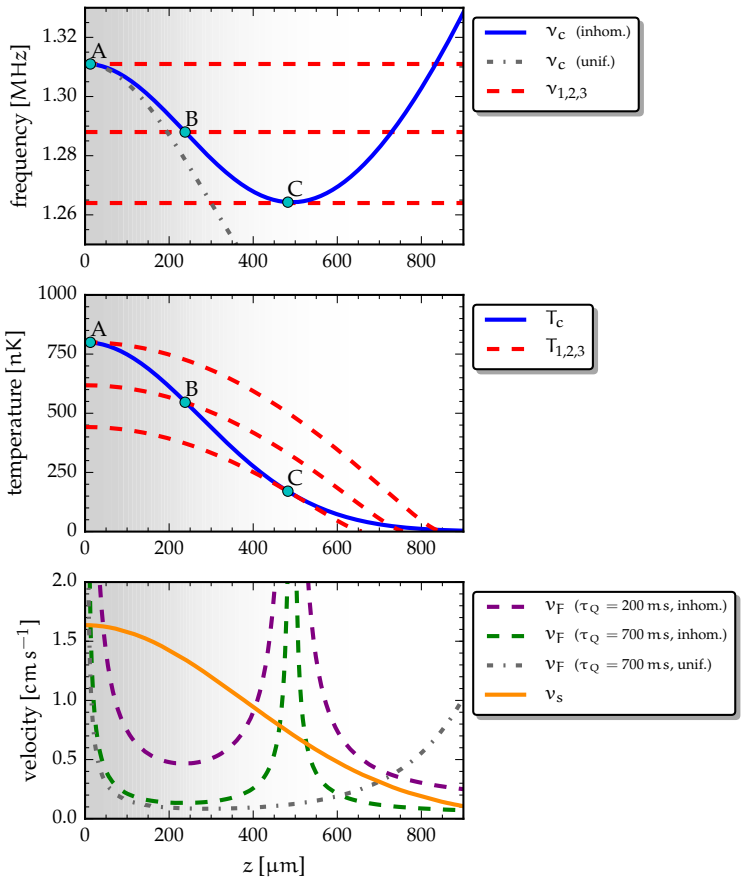

Figure 3.8: Results of our toy model for the local properties of the gas at the BEC transition, plotted as a function of the axial position z in the trap. In the upper plot we consider three evaporation thresholds $\nu_{1,2,3}$ (dashed red), to be compared with the RF critical profile ν_c (solid blue). The corresponding temperature profiles $T_{1,2,3}$ and T_c are plotted in the middle, calculated considering a truncation parameter $\eta \simeq 5$. During the evaporation ramp the transition front (defined by $\nu = \nu_c$, or equivalently by $T = T_c$) moves from the center (A) to outer positions (B,C). In the bottom plot the front velocity v_F for fast (dashed purple) and slow (dashed green) linear quenches is compared with the sound velocity v_s (solid orange). The KZM should be activated in the regions where $v_F > v_s$. For comparison v_F is calculated also assuming a uniform temperature T in the gas during the slower quench (dot-dashed gray). The atomic density (background gray scale) is maximum in the center of the trap at $z = 0$, and it vanishes at the borders.

3.4.2 Effects of the inhomogeneous temperature

We tried to find an experimental support for the hypothesis of an axially dependent temperature $T(z)$ set by the evaporative frequency ν during the quench, as discussed for equation (3.9), which is the basis of the model previously presented for the inhomogeneities in our system. In general the temperature of a trapped thermal gas can be measured with absorption imaging from the Gaussian width σ_i of the expanded density distribution along the axis i, which after a ballistic expansion of t_{TOF} scales as

$$\sigma_i = \sigma_{i_0}\sqrt{1+\omega_i^2 t_{TOF}^2}\,, \tag{3.13}$$

where

$$\sigma_{i_0} = \sqrt{\frac{k_B T}{m\omega_i^2}} \tag{3.14}$$

is the cloud size in the trap along the respective axis (Ketterle et al., 1999). If the expansion is long compared to the trap oscillation period, i. e., if the condition $t_{TOF} \gg \omega_i^{-1}$ is verified, the atomic density distribution after free expansion reflects the in-trap *momentum distribution* and σ_{i_0} can be neglected. However, since we want to maintain the information about the in-trap *spatial distribution* along the axial direction, we can consider an intermediate regime by choosing an expansion time which is longer than the radial oscillation period ($t_{TOF} > \omega_\perp^{-1}$) while being at the same time shorter than the axial period ($t_{TOF} < \omega_\parallel^{-1}$).

We prepare the atomic sample with a fast temperature quench with $\tau_Q = 280\,ms$, stopping the ramp at the frequency $\nu = 1.31\,MHz$, just above the transition occurring at $\nu = 1.29\,MHz$. In order to access the intermediate expansion regime just discussed, the cloud is imaged after a time $t_{TOF} = 5\,ms$. Then we divide the picture into narrow slices at different axial positions in the atomic distribution, and we fit each slice with a 1D Gaussian function along the radial direction, thus measuring the local Gaussian radial width $\sigma_\perp$ as a function of z. We repeat this measurement of $\sigma_\perp(z)$ for different values of the time t_w waited after the end of the quench and before taking the picture. The results are reported in figure 3.9.

In first approximation we can neglect the in-trap radial width $\sigma_{\perp_0}$, hence supposing that $\sigma_\perp(z) \propto \sqrt{T(z)}$. Under this assumption the temperature trend just after the quench, i. e., the series with $t_w = 0\,ms$, seems to qualitatively agree with the behavior that can be extrapolated from equation (3.9). In fact the radial Gaussian width is higher in the center of the cloud, while it decreases at the borders. For higher values of t_w the axial inhomogeneity of $\sigma_\perp$ looks less pronounced, suggesting that the axial thermalization actually happens on a longer timescale, of the order of few hundreds of ms.

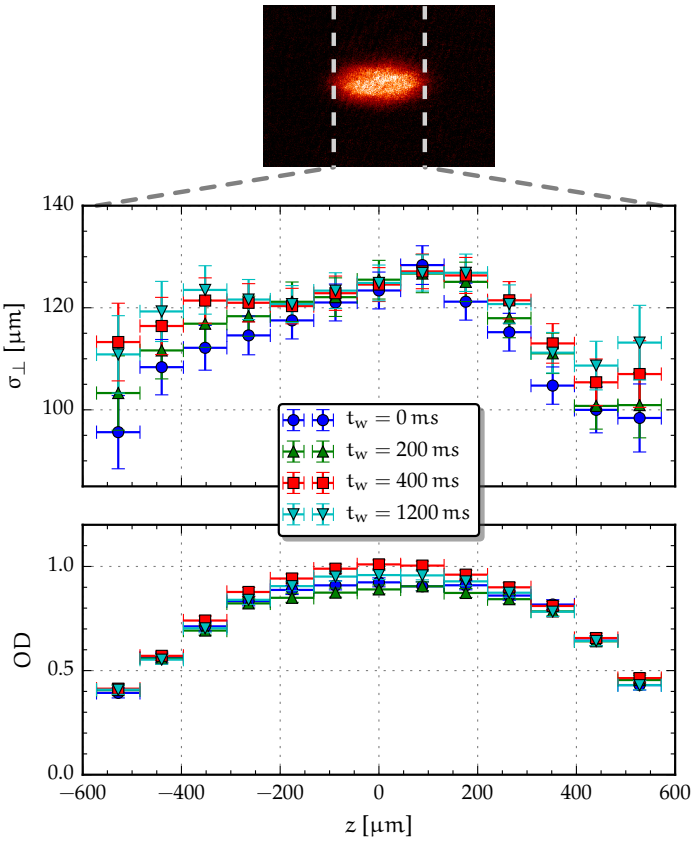

Figure 3.9: Radial Gaussian width (first plot) and peak optical density (second plot) of thermal atomic clouds after a TOF of 5 ms. The results are plotted as a function of the axial position for different values of the time waited after a fast quench with $\tau_Q = 280$ ms. A sample picture of thermal cloud considered for this measurement is reported in the upper part.

Even if these observations go in the right direction, we should take them with care. In fact the measurements could be affected by spurious effects, such as the vanishing atomic density in the outer part of the cloud, as it can be seen from the optical density plotted in figure 3.9. In particular we did not try to extract a quantitative value of the temperature since this would require the knowledge of $\sigma_{\perp_0}$, which is not directly measurable with our imaging system. Moreover we observed a dependence of the measured $\sigma_\perp$ on the intensity of the repumping light used during the imaging sequence, hence putting a strong concern on the validity of any quantitative analysis.

3.4.3 Role of the atom number

Some indications about the validity of the model previously presented for our inhomogeneous gas can be extracted from the comparison between the two series of figure 3.6, reporting the defect number scaling with different atom numbers at the transition N_c. The quench time setting the threshold for the observation of defects, highlighted with a arrow in the plot, is shifted to higher values of τ_Q for the series with lower N_c. This means that defects are created even for slower quenches relative to the case with higher N_c. This is consistent with a lower speed of sound for a lower atomic density, which we roughly considered for the causal horizon. In fact the critical temperature for an ideal gas in a harmonic potential (Pitaevskii et al., 2016) can be expressed as

$$T_c = \frac{0.94\,\hbar\omega_{ho}}{k_B} N_c^{1/3}\,, \tag{3.15}$$

where ω_{ho} the geometric mean of the trapping frequencies:

$$\omega_{ho} = \sqrt[3]{\omega_\perp^2\,\omega_\parallel}\,. \tag{3.16}$$

Therefore the speed of sound around T_c introduced in equation (3.12) would scale as

$$v_s \propto \sqrt{T_c} \propto N_c^{1/6}\,. \tag{3.17}$$

Even if a quantitative comparison would require a deeper theoretical understanding of the threshold phenomena for the KZM in inhomogeneous systems, we observe that, considering the experimental data with $N_c = 25\times10^6$ and $N_c = 4\times10^6$ atoms, we expect v_s to be smaller by a factor of $0.74(6)$. This is consistent with the measured factor of $0.84(8)$ for the relative shift in τ_Q of the defect detection threshold. A slower sound velocity would also explain why in the data set with $N_c = 4\times10^6$ atoms we observe more defects compared to the series with $N_c = 25\times10^6$ atoms for the same values of τ_Q. In fact, since the speed of sound is slower, with fewer atoms we expect a wider region of the condensate where $v_F > v_s$, hence leading to a higher number of defects.

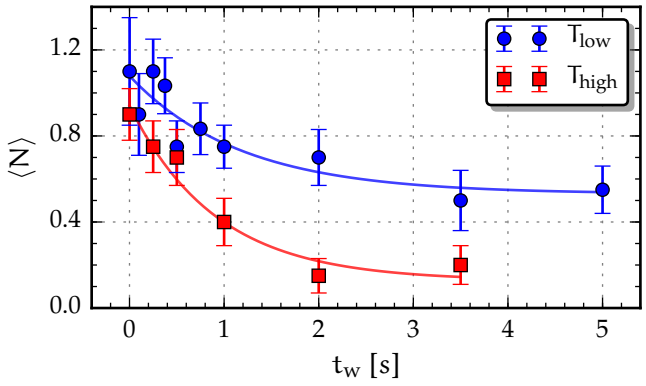

Figure 3.10: Average defect number as a function of the time waited after a quench ramp with $\tau_Q = 467\,\mathrm{ms}$. Two series are reported: one for an almost pure condensate with a temperature $T_{low} \simeq 200\,\mathrm{nK}$, the other leaving a sizable fraction of atoms in the non-condensed state with a higher temperature $T_{high} \simeq 600\,\mathrm{nK}$, near to $T_c \simeq 800\,\mathrm{nK}$. For each data set the solid line is the exponential decay curve fitting the experimental points with an offset. From our observation we find that the final temperature does not show a dependence on the waiting time.

3.5 DEFECT LIFETIME

As discussed in section 3.2, we initially interpreted the defects observed in our condensates as solitons, mislead by their apparent planar 2D shape. However solitons are not expected to be stable in 3D systems with a finite temperature (Brand et al., 2002; Komineas et al., 2003), and in experiments they are typically observed on timescales short as compared to the harmonic oscillator period (Burger et al., 1999; Denschlag et al., 2000; Anderson et al., 2001). The *defect lifetime* should be taken into consideration in measurements based on defect counting such ours. In fact, if a soliton decays on a timescale that is shorter or comparable with the experimental quench procedure, i. e., on the order of τ_Q, the number of counts will be lower than the original defect number. A direct study of this possibility would require a non-destructive imaging technique, not implemented here. Therefore, in order to clarify this possibility, we measure the average number of defects as a function of the wait time t_w spent in the trap at the end of the quench ramp for a given τ_Q.

The results for the defect lifetime are reported in figure 3.10 for two sets of measurements with different temperatures T_{low} and T_{high}, the latter controlled by changing the final frequency of the evaporation ramp. The average defect number as a function of t_w is fitted to an exponential decay curve with offset. For the series at a temperature that is well below T_c we measure a defect lifetime $\tau_{low} = 1.2(5)\,\mathrm{s}$, while for the series at higher temperature we measure a slightly faster

decay with a time constant $\tau_{high} = 0.9(3)\,s$. This is consistent with a temperature-dependent decay mechanism for solitons.

The lifetime τ is long compared to the experimental procedure following the quench, therefore in first approximation we can assume that, during the finalization ramp and the time waited before the imaging as described in section 3.3.1, the decay does not alter the scaling behavior measured for the defect number. However, since the decay time is comparable with the quench time τ_Q, our measurements of the defect number scaling might be slightly affected, in particular for the slower quenches. The role of the defect decay on the defect counts will be discussed in detail in chapter 5.

As a final remark, from figure 3.10 we observe that an important fraction of defects survives for more than 5 s, measured as an offset of about 0.5 defects in the exponential decay for the series at lower temperature. Regarding this unexpectedly long lifetime, in our first article on the KZM (Lamporesi et al., 2013b) we speculated the creation of long living solitons generated with a small initial velocity and a reduced energy dissipation, even if this mechanism remained unclear. This point suggested us to better investigate the nature of the defects forming in our system, that, following the study that will be reported in the next chapter 4, we finally identified as solitonic vortices instead of solitons (Donadello et al., 2014).

4 SOLITONIC VORTICES

The ground state of a Bose–Einstein condensate is characterized by a well-defined order parameter, with a uniform phase and a smooth density profile related to the confining potential. Excited states can exhibit stable phase defects, such as solitons or vortices. In the previous chapter I discussed the spontaneous creation of defects in our elongated gas, occurring after fast quenches across the BEC transition via the KZM. In the present chapter I will describe the studies that allowed us to identify those defects as solitonic vortices.

The peculiar properties of solitonic vortices will be presented in section 4.1, following our first experimental observations. The direct observation of the nodal line of solitonic vortices, as well as the demonstration of phase circulation with matter interferometry, will be reported in section 4.2. In section 4.3 I will present the results of numerical calculations supporting our experimental conclusions. Finally in section 4.4 I will discuss the possible temporal evolution of solitonic vortices.

4.1 OBSERVATION OF VORTICES IN AN ELONGATED BEC

In the previous chapter 3 we reported the experimental observation of defects spontaneously created via the KZM after rapid temperature quenches across the BEC transition. In our article on the KZ scaling we identified those defects as gray *solitons* (Lamporesi et al., 2013b). This was mainly motivated by the elongated shape of the sample and by the planar geometry of defects, as they appeared by imaging the condensate along two orthogonal radial directions after a long TOF. However, the observation of a long defect lifetime of the order of 1 s was unexpected for this kind of defects, since several numerical and experimental studies showed that solitons are unstable in 3D systems (Burger et al., 1999; Feder et al., 2000; Denschlag et al., 2000; Anderson et al., 2001). Long living solitonic structures were similarly observed by Yefsah et al. (2013) in an elongated unitary Fermi gas.

Another point that drew our attention was the observation of defects with a particular and recurring shape in many of the experimental images taken while studying the KZM. Considering the examples of figure 4.1, the density depletion associated to the defect is not straight as one would expect while looking at a regular planar

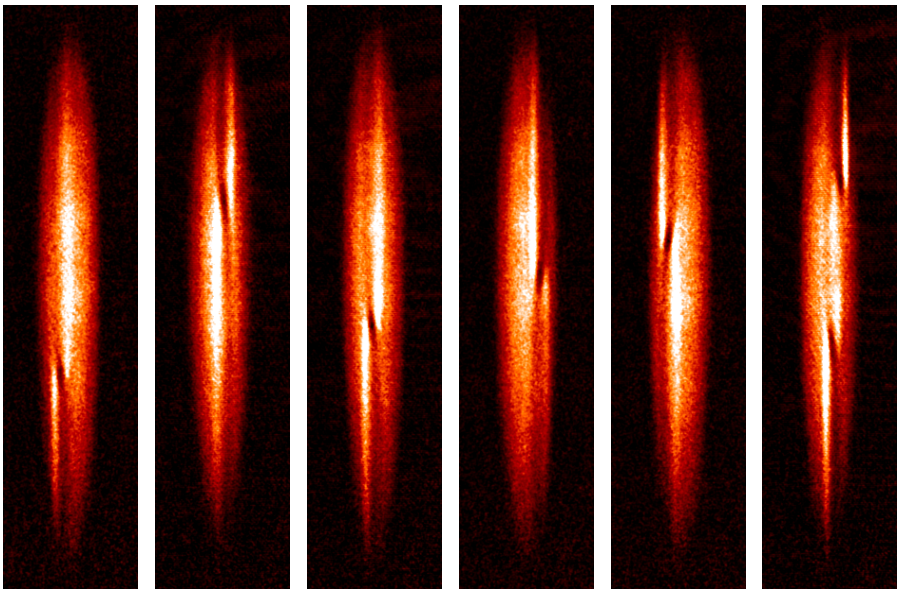

Figure 4.1: Examples of condensates containing defects twisting around a hollow core, observed during the KZM measurements reported in chapter 3. The absorption images are taken along the horizontal radial direction after an expansion time of 180 ms. We observe both clockwise and counterclockwise twists for these defects that we identified as solitonic vortices. Two solitonic vortices are visible in the last picture.

structure, but it *twists* around a density dip. This bended shape of the solitonic plane intuitively suggested us that some kind of circulation was present in the superfluid around a line aligned with the direction of observation, similarly to what happens for a vortex.

The identification of our defects as *vortices* was intriguing since, whereas these structures have been extensively studied in oblate or spherical traps, stable vortices in elongated condensates such ours were never observed before in a direct way, although being predicted by Brand et al. (2002) and Komineas et al. (2003). Following those theoretical studies, the relevant parameter to address the stability of defects in axially symmetric systems is the dimensionless *confinement parameter* γ, defined in equation (1.50) as

$$\gamma = \frac{\mu}{\hbar\omega_\perp} = \frac{R_\perp}{2\xi_l}, \tag{4.1}$$

where μ is the chemical potential, $\frac{\omega_\perp}{2\pi}$ the radial trapping frequency, $R_\perp$ the in-trap radius of the condensate in the transverse direction, and ξ_l the healing length. As previously introduced in section 1.3.2, in tightly confined systems with $\gamma \ll 1$ solitons are stable, whereas states with lower excitation energy become accessible for bigger values of γ. In particular, structures called *solitonic vortices*, which can

be described as vortices with anisotropic phase and density profiles, represent the least energetic states in elongated systems with $\gamma \gg 1$. The crossover between the two regimes sets in when $\gamma \sim 1$, i. e., when the defect size, fixed by ξ_ι, becomes of the order of the transverse size of the condensate, fixed by Thomas–Fermi radius $R_\perp$.

In our system defects are spontaneously created while crossing the BEC transition with forced evaporative cooling, with the confining potential being characterized by axial and radial trapping frequencies of respectively $\frac{\omega_\parallel}{2\pi} = 13\,\text{Hz}$ and $\frac{\omega_\perp}{2\pi} = 131\,\text{Hz}$. Starting from 25×10^6 atoms at the transition point, after the temperature quench we obtain almost pure condensates of about 10×10^6 atoms. Under these experimental conditions at the end of the evaporation we have a confinement parameter $\gamma \simeq 27$, and thus we expect to be in the regime where the solitonic vortex (SV) is the most stable topological excitation (Brand et al., 2002; Komineas et al., 2003). In our articles on the topic we reported experimental and numerical arguments supporting this interpretation (Donadello et al., 2014; Tylutki et al., 2015). The observation of solitonic vortices in cigar-shaped unitary Fermi gases was simultaneously reported by Ku et al. (2014), while indirect evidences of this kind of defect in BECs were previously described by Becker et al. (2013).

Considering axially symmetric systems, figure 4.2 reports the density distribution and phase pattern calculated for a vortex in an isotropic geometry, a SV, and a dark soliton. The equilibrium configuration of vortices in trapped condensates with different aspect ratios can be understood observing the expression for the vortex excitation energy reported in equation (1.49), which is proportional to the length of the nodal line.

- In *oblate* systems vortices are less energetic when they are aligned parallel to the symmetry axis. If a vortex is placed in the center of such a system, the phase of the order parameter winds linearly with angle by 2π while rotating around the vortex core. Therefore the phase gradient maintains the cylindrical symmetry around the principal axis, with an *isotropic circulation* in the velocity field defined by the relation of equation (1.34).

- In *prolate* systems vortices minimize their energy taking an orientation which is orthogonal to the symmetry axis. The equiphase surfaces of the vortex phase pattern must be orthogonal to the outer surface of the cigar-shaped condensate, resulting therefore bended and squeezed along the short radial direction. The result is vortex where the phase variation is concentrated in a narrow region around the radial plane of the vortex core. Consequently the system reduces its energy by depleting the atomic density in the transverse surface where the phase gradient and the velocity field are higher, a configuration that is called *solitonic vortex*.

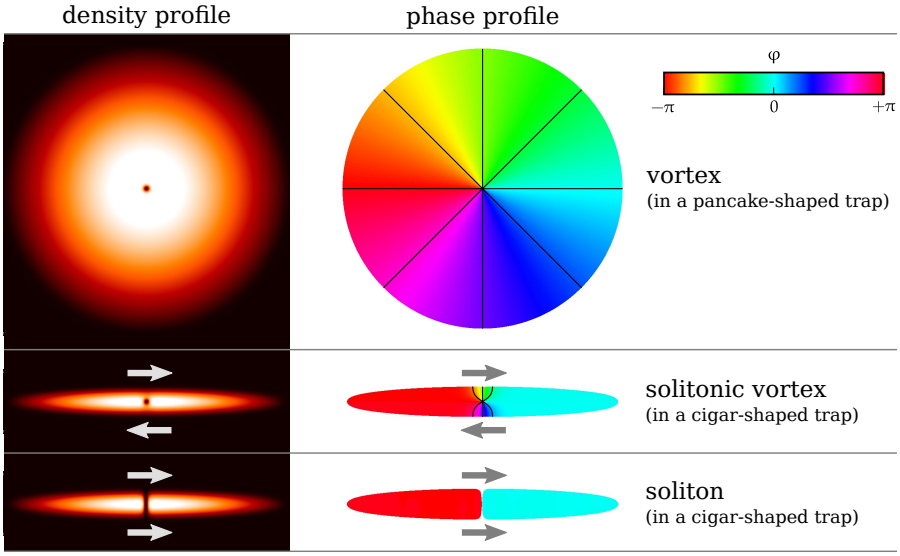

Figure 4.2: Phase and density profiles calculated for different configurations of defects in BECs trapped in axially symmetric potentials: a vortex aligned with the symmetry axis, a SV with its core along the transverse direction, a soliton with the nodal plane perpendicular to the symmetry axis. The atomic flow, indicated with arrows, is uniformly oriented across the plane of the soliton. Conversely, in the case of the SV, the velocity field exhibits opposite relative directions above and below the vortex core.

From figure 4.2 it can also be observed that, far from the depleted region, the phase pattern looks similar for a SV and a soliton, with the two sides of the condensate showing a phase difference of about π. However, whereas for a soliton the phase gradient is constant on the nodal plane, for a SV it has opposite signs in the two half-planes separated by the vortex core. For this reason one may expect that, during the free expansion of a condensate containing a SV, the two sides of the depleted plane twist around the vortex core. This qualitative picture can explain the geometry of the defects in figure 4.1, and it suggests that the rotation sign of a SV can be extracted directly from the observation of the depletion twist around the hollow core, whose direction can be either clockwise or counterclockwise.

4.2 CHARACTERIZATION OF SOLITONIC VORTICES

4.2.1 Triaxial imaging of vortex lines

In order to demonstrate our hypothesis about solitonic vortices we wanted to figure out if the defects that we observe in condensates have a *non-planar geometry*. The observation of the system only along radial directions, as we have done in the measurements presented in chapter 3, cannot give us an ultimate answer. In fact the twists ob-

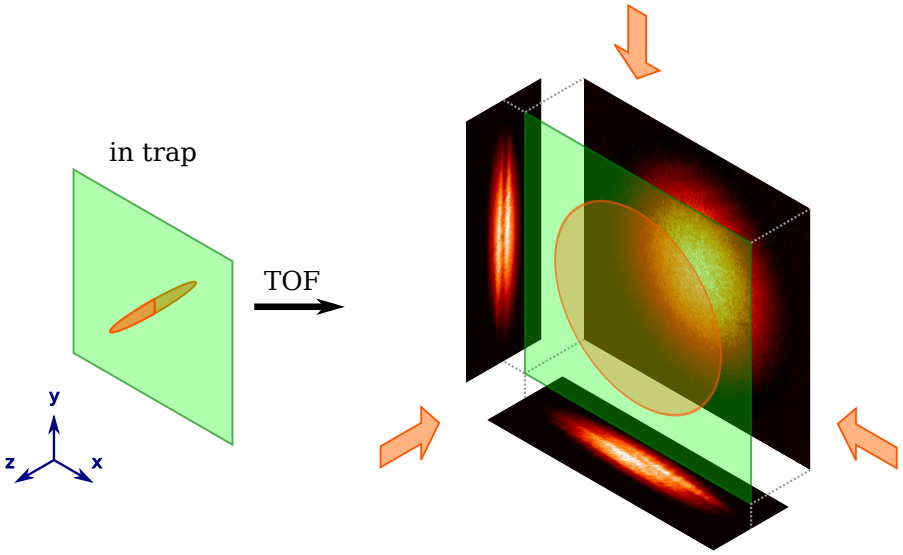

Figure 4.3: Sketch of our imaging configuration, where after a long free expansion the pancake-shaped condensate is probed along the symmetry axis and two orthogonal radial directions. The directions of the probe light beams are indicated with orange arrows. Possible non-planar structures might be observed along the axial direction.

servable in the radial images of figure 4.1 might be also interpreted as solitons having bended planes. As a natural extension of our imaging we added a CCD camera along the direction of the trap symmetry axis, thus being able to take pictures of the condensate simultaneously along three orthogonal axes, as sketched in figure 4.3.

We perform temperature quenches with an evaporation rate of $300\,\mathrm{kHz\,s^{-1}}$. Then we leave the condensate to expand for a TOF of $120\,\mathrm{ms}$ with magnetic levitation, and we probe the atoms with *triaxial imaging*. After such a long expansion time the condensate takes a pancake-like shape (Castin et al., 1996; Ernst et al., 1998). The Thomas–Fermi radii of the expanded condensate are about $1.5\,\mathrm{mm}$ in the radial direction and $0.3\,\mathrm{mm}$ along the symmetry axis. Due to the oblate shape of the atomic cloud, the peak optical density in axial pictures is less than $1/4$ respectively to radial ones, resulting in a significantly reduced signal-to-noise ratio. For this reason the small depletion signals that we observed in some axial images were hardly distinguishable from background shot noise and other spurious signals such as optical interference fringes, as it can be seen from the example of figure 4.4a.

In order to enhance the visibility of possible defects in axial pictures we implemented the following *digital filtering* procedure.

1. Firstly we fit the axial image with a 2D parabolic function, which describes well a smooth condensate during free expansion.

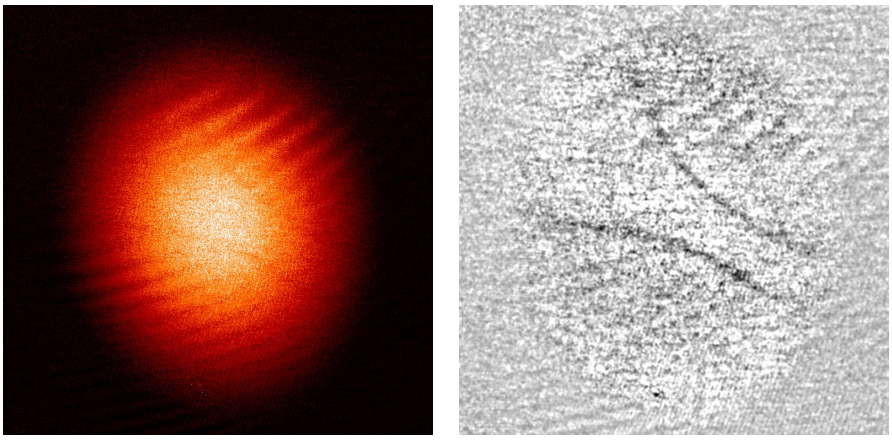

(a) Raw absorption image. **(b)** Processed fit residuals.

Figure 4.4: Example of image filtering applied to the axial image of an expanded condensate. Two linear defects are clearly visible in the final processed image, obtained from the residuals of the parabolic fit performed on the original image. The optical fringes and the shot noise are attenuated respectively by subtracting a reference matrix and by applying a Gaussian filter.

2. Then we consider the matrix of the fit residuals, i. e., the difference between the experimental image and the fitting parabola. Any irregularity in the density profile results to be amplified in the residuals, indistinguishably for spurious signals or possible interesting structures in the condensate.

3. We create a reference matrix by averaging the fit residuals of many different axial images. The optical fringes give rise to signals which remain almost constant shot-to-shot, whereas spontaneous defects are created with random orientations and positions, hence giving a negligible contribution to the final average.

4. We selectively remove the optical fringes by subtracting the reference matrix to the fit residuals for each axial image, hence being able to discriminate real irregularities in the atomic distribution.

5. Finally we apply a Gaussian filter in order to reduce the shot noise, with a filter width of about 1 pixel.

The result of this processing sequence applied to the picture in figure 4.4a is reported in figure 4.4b. In the final axial image two linear structures are observable with enhanced contrast and visibility, whereas in the raw picture they represent a depletion of less than 5 % in the density profile.

The comparison between axial and radial images gives us a clear picture of defects inside the condensate, supporting their identification as solitonic vortices. In fact, a twisting plane observed along one

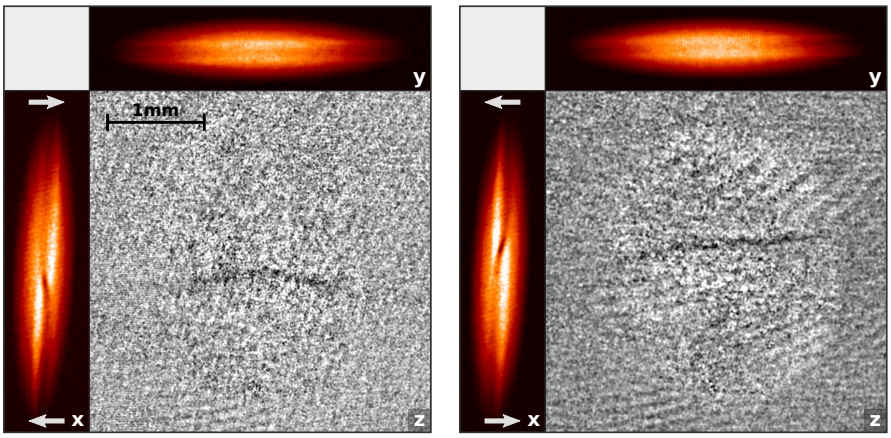

(a) Solitonic vortex. **(b)** Solitonic anti-vortex.

Figure 4.5: Triaxial absorption images of condensates taken after 120 ms of expansion with levitation. A SV is present in each sample, with the vortex core being aligned horizontally. The direction of the atomic flow is indicated with arrows in the respective horizontal radial images: the atomic circulation is clockwise in the first condensate, opposite in the second one, which we arbitrarily refer as vortex and anti-vortex. Each radial image reports the integrated atomic density, whereas each axial image presents the filtered residuals of the parabolic fit.

radial direction in general can be associated to a linear structure in the axial image, that we consequently identify as the *core* of a SV. Let us take the two examples of figure 4.5, where the *nodal lines* are aligned horizontally: in each respective radial picture along the horizontal direction we observe that the solitonic plane twists around the density dip of the vortex core, whereas just a linear stripe is visible in the vertical radial image.

As introduced in previous section 4.1, the twist of the solitonic plane observed in an expanding condensate along a radial direction can be the effect of the atomic flow, circulating around the vortex core as defined by the phase gradient. Specifically the velocity field causes a deformation in the depleted plane, that seems to twist in the opposite direction. Therefore the *sign of vorticity* can be determined directly from absorption images. In particular we can arbitrarily define the solitonic *vortex* when the circulation is clockwise in our frame, i. e., with a *s*-shaped twist, and the solitonic *anti-vortex* when the circulation is counterclockwise, i. e., with a *z*-shaped twist. The experimental images of a solitonic vortex and anti-vortex are reported in figures 4.5a and 4.5b respectively.

We do not observe any preferred orientation for solitonic vortices, as we expect for defects randomly created via the KZM in an isotropic radial confinement. We quantify the negligible radial anisotropy to be $\lesssim 10^{-4}$, estimated by measuring with high accuracy the radial

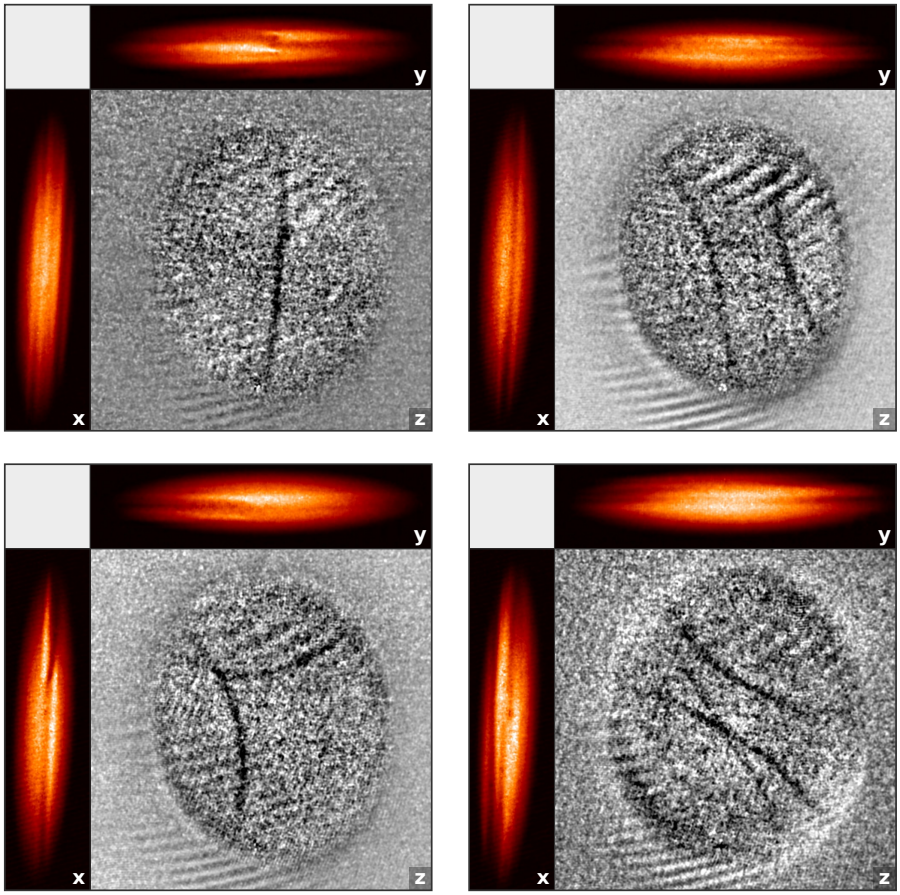

Figure 4.6: Triaxial images of condensates containing one ore more solitonic vortices with random orientations and shapes. The geometry of defects can be identified from the comparison of radial and axial images.

trapping frequency along horizontal and vertical directions. This was done by exciting the respective dipole oscillatory modes of a trapped condensate, after applying a pulsed homogeneous magnetic field.

As it can be seen from the examples in figure 4.6, the interpretation of images can be more complicated in the presence of more than one solitonic vortex in the same condensate. Anyway the triaxial imaging allows us to identify and count defects with enough confidence from the comparison of pictures taken from different point of views. Further observations can explain why often we do not observe any twist in radial images: only when at least one end of the vortex core is aligned with the direction of observation it is visible as a twist in the respective integrated radial image. Conversely, the twist can have a reduced contrast when the vortex line is tilted or bended, being completely hidden in some cases where just the solitonic plane can be distinguished, a possibility that can lead to a misleading interpretation in terms of solitons.

4.2.2 Interferometric detection of phase circulation

The triaxial imaging clearly demonstrates the non-planar geometry of our defects and strongly supports the solitonic vortex hypothesis. In order to provide a direct experimental proof for *phase circulation* we implemented a *matter-wave interferometer*, which exploits the coherence properties of BECs. The mechanism behind this technique can be understood in analogy with optics: since a BEC is a quantum system with a well-defined macroscopic wave function, condensates with different phases will interfere producing matter interference fringes in a similar way as light in classical optical interferometers.

The possibility of identifying vortices in BECs with interferometry was theoretically proposed by Bolda et al. (1998): whereas systems with uniform phase gradients produce interference fringes with regular patterns, the presence of phase circulation causes the appearance of *fringe dislocations* in correspondence of the vortex core, with one or more fringes disappearing at the phase singularity. The detection of artificially created vortices with heterodyne and homodyne interferometric techniques was demonstrated respectively by Inouye et al. (2001) and Chevy et al. (2001). In the former experiment, performed in a double-well system where one unperturbed condensate was used as local oscillator for the interferometer, vortices appeared as single dislocations. Instead in the latter experiment vortices were visible as pairs of dislocations in the interference pattern, originating from slightly separated copies of the same condensate.

Our interferometer is based on homodyne detection: we obtain coherent copies of the BEC using optically induced *Bragg diffraction*, following the scheme described by Kozuma et al. (1999). This two-photon Raman process is triggered by shining the atoms with Bragg pulses using two off-resonance laser beams. These beams are aligned with a relative angle of $\vartheta_B = 110°$ and propagate along the vertical plane passing through the symmetry axis of the trap, with a linear polarization along the same axis. The diffracted atoms acquire a velocity equal to

$$v_B = 2\sin\left(\frac{\vartheta_B}{2}\right) v_{rec} \simeq 4.8\,\mathrm{cm\,s^{-1}}\,, \tag{4.2}$$

with $v_{rec} = 2.9\,\mathrm{cm\,s^{-1}}$ being the recoil velocity of sodium atoms at the wavelength of the D_2 transition. In our conditions the relative light detuning between the beams, which is optimal for exciting the first-order Bragg diffraction, is $\Delta_B = 2\pi \times 67\,\mathrm{kHz}$.

The condition that must be verified to obtain a momentum transfer on half of the atomic population is $\Omega\tau \simeq \frac{\pi}{2}$, with τ the duration of the pulse, and Ω the Rabi frequency related to the optical dipole potential:

$$\Omega = \frac{I\,|\langle d\rangle|^2}{2c\varepsilon_0\hbar^2\Delta_B} \simeq 2\pi \times 25\,\mathrm{kHz}\,, \tag{4.3}$$

where $|\langle d \rangle| = 3.0 \times 10^{-29}\,\mathrm{C\,m}$ is the matrix element of the electric dipole moment for the D_2 transition, $I = 12\,\mathrm{mW\,cm^{-2}}$ the intensity of each optical beam, c the speed of light, and ε_0 the dielectric constant. Therefore, in order to split the condensate into almost equal parts, we perform $\frac{\pi}{2}$-pulses of duration $\tau = 8\,\mathrm{ms}$.

The experimental sequence implemented for our open-type interferometer, sketched in figure 4.7, is based on two $\frac{\pi}{2}$-pulses.

1. The first $\frac{\pi}{2}$-pulse coherently splits the condensate into two copies after a time $t_1 = 20\,\mathrm{ms}$ from the release of the trap, with one copy traveling along the direction of the transferred momentum, the other remaining at rest. This initial expansion is needed in order to reduce the atomic density and consequently the interaction effects between the copies of the condensate.

2. The second $\frac{\pi}{2}$-pulse is applied after a time $t_2 = 1.5\,\mathrm{ms}$, when the two copies of the condensate are separated by

$$d_B = v_B t_2 \simeq 72\,\mu\mathrm{m}\,. \tag{4.4}$$

3. After the two Bragg pulses, we obtain four equally populated copies of the original condensate, two of them at rest (output *A*), the other two traveling at velocity v_B (output *B*).

4. We take a picture of the system with standard absorption imaging along the horizontal radial direction after a time $t_3 = 98.5\,\mathrm{ms}$, when the copies with different velocities are well separated. The total expansion time is therefore $t_{TOF} = t_1 + t_2 + t_3 = 120\,\mathrm{ms}$.

At the end of the interferometer sequence the copies of the condensate with equal velocities partially overlap in space, being slightly separated by the distance d_B. The resulting density profiles show interference patterns with a fringe spacing of

$$\lambda = \frac{h t_3}{m d_B} \simeq 25\,\mu\mathrm{m}\,, \tag{4.5}$$

well above the imaging resolution of about $5\,\mu\mathrm{m}$.

In figure 4.8a we report the two outputs of the interferometer in the presence of a solitonic vortex, i. e., with the atomic flow rotating clockwise while looking at the picture, following the definition previously proposed. The atomic density modulation caused by the presence of the defect is partially preserved in output *A*, while the corresponding interference pattern can be better appreciated from output *B*. The density dip of the vortex core, where the solitonic plane twists, can be associated to a pair of fringe dislocations as expected for vortices within the homodyne detection method (Bolda et al., 1998; Chevy et al., 2001). Moreover a qualitative agreement can be observed with the interference pattern calculated for a solitonic vortex from the 2D numerical simulations that will be described in the next section 4.3. In

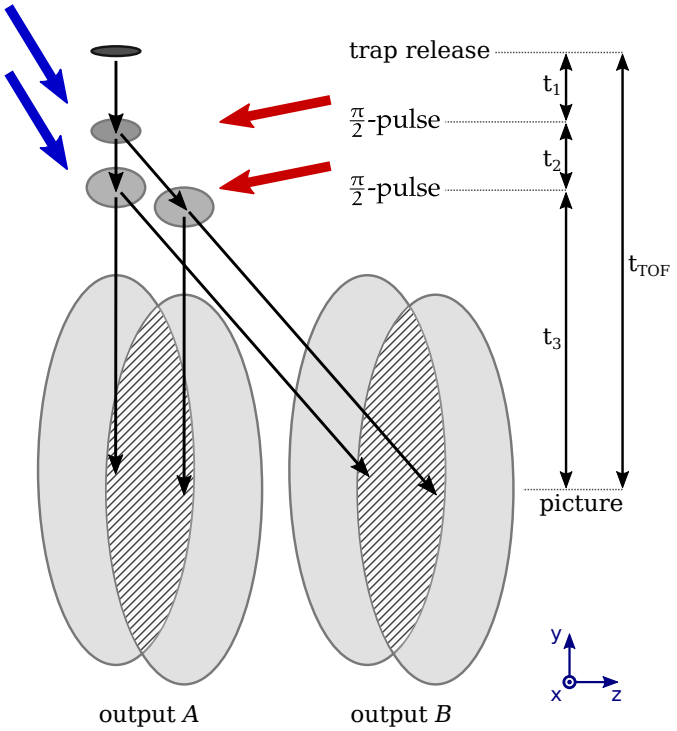

Figure 4.7: Temporal sequence for the Bragg interferometer. After a time t_1 from the trap release we perform two $\frac{\pi}{2}$-pulses separated by a time t_2. Each pulse splits the condensate into equal parts. After a time t_3 we image the two outputs of the interferometer, one at rest (A), the other moving at the Bragg velocity v_B (B). Interference fringes originate in the density profiles of the overlapping and slightly separated copies of the condensate.

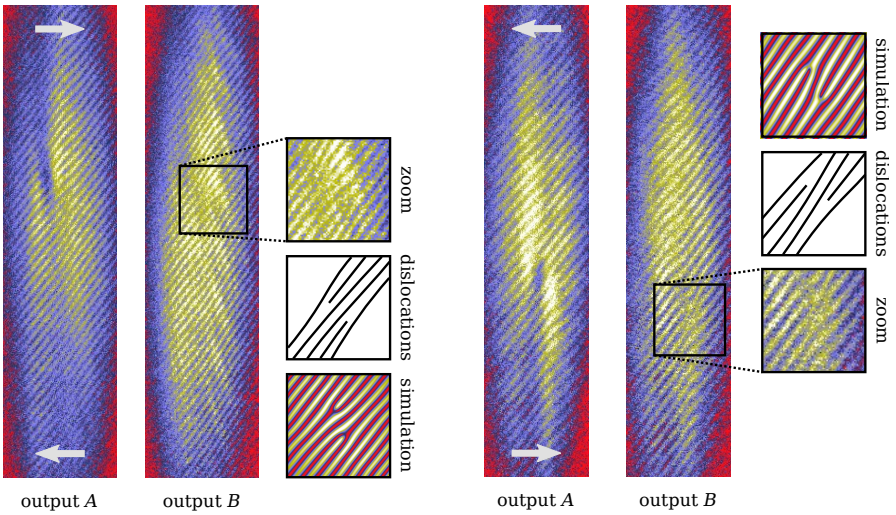

(a) Solitonic vortex. **(b)** Solitonic anti-vortex.

Figure 4.8: The two outputs of the Bragg interferometer in presence of a solitonic vortex (left) and anti-vortex (right). In each case the pair of fringe dislocations associated to the vortex core is magnified and sketched for simplicity. The experimental fringe patterns are compared with 2D GPE simulations.

figure 4.8b we report the interferometer outputs for a solitonic anti-vortex, i. e., with counterclockwise circulation: a pair of dislocations is present also in this case, but showing a chiral mirror image in relation to the previous case.

These observations confirm that the twist in the depleted plane of a defect observed in the radial density profile of a condensate is associated to phase circulation, and that therefore we are actually observing solitonic vortices. Moreover we demonstrate that the sign of vorticity can be assigned directly from the observation of the twist direction in absorption images of BECs after free expansion.

4.3 NUMERICAL SIMULATIONS OF SOLITONIC VORTICES

In order to further support our experimental evidences we performed numerical calculations for the density distribution of a SV in a BEC, both in trap and after free expansion, the latter to be compared with the experimental images taken after TOFs. More technical details on the simulation methods, performed by solving the GPE introduced in equation (1.37), can be found in our article on the topic (Tylutki et al., 2015).

The initial condition for the simulations is a trapped stationary state, whose phase pattern is imprinted with a SV. As a first step

we characterize the *in-trap* properties of the SV by varying the aspect ratio $AR = \omega_\perp/\omega_\parallel$ and the chemical potential μ of the condensate, both for 2D and 3D simulations. For each condition we extract the in-trap atomic densities n_a and n_b at half of the Thomas–Fermi radii, respectively along axial and radial directions. The ratio n_b/n_a represents a measure for the contrast of the radial depletion, being 1 when the system is isotropic and 0 when the transverse plane is completely depleted.

The results for n_b/n_a as a function of the inverse aspect ratio AR^{-1} are reported in figure 4.9, considering the range going from the limit of a spherical trap, with $\omega_\parallel/\omega_\perp = 1$, to the limit of a quasi-1D system, with $\omega_\parallel/\omega_\perp \ll 1$. We can distinguish three regimes.

- The bulk regime, where the solitonic vortex becomes an *isotropic vortex* and the density distribution is symmetric around the core, with $n_b/n_a \simeq 1$.
- Going to elongated systems we enter in a *crossover* regime, where the solitonic plane appears in the transverse direction passing through the vortex core, with $0 < n_b/n_a < 1$.
- The effective 1D regime, where the defect becomes a *dark soliton*, with a maximum contrast and $n_b/n_a \simeq 0$.

When the same data are plotted as a function of confinement parameter γ, defined in equation (1.50), all the points belonging to different series collapse on the same curve, confirming that γ is the quantity which is relevant for the nature of defects.

We also performed simulations of defects *after free expansion*, integrating the GPE in time after setting the trapping potential to zero. The results show that, considering a soliton as initial state, the planar density depletion maintains its shape in time. As it can be deduced from the definition of the healing length reported in equation (1.38), during the expansion the soliton becomes wider as a consequence of the decreasing density. Conversely, when the initial state contains a solitonic vortex, the solitonic plane becomes visible while expanding, twisting as a consequence of the atomic flow circulating around the vortex core. This phenomenon can be observed from figure 4.10, where the 2D density profile of the SV is reported at different values of the expansion time. The rotation of the solitonic plane saturates when the mean-field interaction stops to play a role and the expansion becomes ballistic.

The free expansion of a solitonic vortex has been characterized with 3D simulations, performed considering an aspect ratio of the trap $AR = 10$, as in our experimental conditions, and a confinement parameter $\gamma = 10$. This value of γ is smaller than the experimental one, which is about 27, since we considered a lower chemical potential in order to speed up the simulations. In figure 4.11 the ratio n_b/n_a is

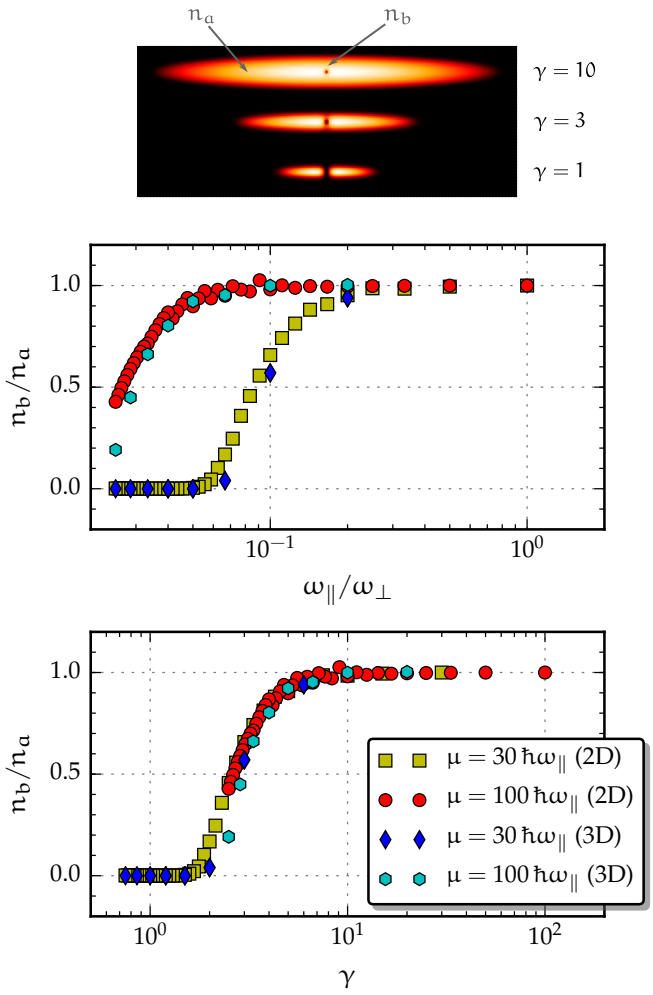

Figure 4.9: Ratio between the atomic density in the solitonic plane and along the symmetry axis, for a SV imprinted in a trapped BEC. In the first graph the results for 2D and 3D numerical simulations are plotted as a function of the inverse aspect ratio, also considering different values of the chemical potential. As it can be seen from the plot in the bottom, the effective variable setting the defect geometry is the confinement parameter γ. The density profile of the condensate is reported in the upper part for different values of γ.

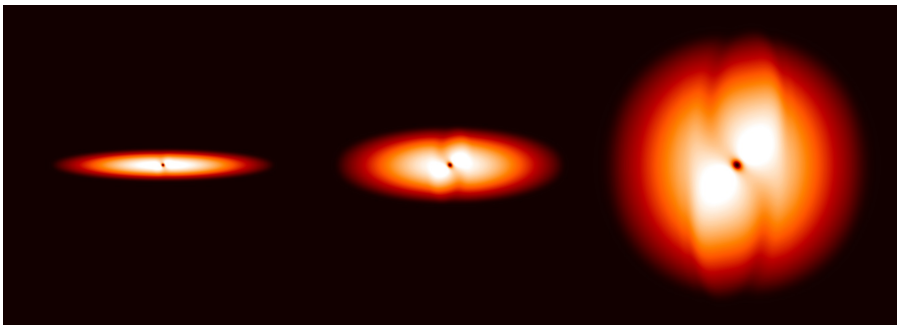

$t_{TOF} = \frac{1}{\omega_\perp}$ $t_{TOF} = \frac{3}{\omega_\perp}$ $t_{TOF} = \frac{10}{\omega_\perp}$

Figure 4.10: Density profile simulated for an expanding 2D BEC containing a solitonic vortex, calculated at different values of the expansion time t_{TOF}. The confinement parameter is $\gamma = 10$. The depleted solitonic plane appears during expansion, increasing its contrast and twisting around the vortex core as a consequence of the atomic circulation.

plotted as a function of the expansion time, where n_a and n_b are defined respectively as the maximum and minimum densities at half of the axial and radial radii of the expanded condensate. These results show that a SV in the trapped BEC appears essentially as an isotropic vortex, with a negligible solitonic plane and $n_b/n_a \simeq 1$ for $t_{TOF} = 0$. Conversely the transverse depletion appears after the trap release, becoming deeper while increasing the expansion time, as it can be seen from the decreasing ratio n_b/n_a for $t_{TOF} > 0$. Therefore the peculiar shape of the solitonic vortex becomes particularly visible after long expansions.

The 3D simulation of a condensate containing a solitonic vortex, i. e., with clockwise phase circulation, is reported in figure 4.12, where the density profile is integrated along radial and axial directions after an expansion of 120 ms. We observe a good qualitative agreement with the analogous experimental images of figure 4.5a. In the simulation the defect appears wider as a consequence of the bigger healing length, since the chemical potential considered for the calculations is about 1/3 of the experimental one.

The interference pattern calculated for a 2D solitonic vortex after expansion was already reported in figure 4.8a while discussing the results of the Bragg interferometry. Also in that case we find a qualitative agreement between the simulation and the experimental counterpart, with a pair of dislocations observed in correspondence to the vortex core. The analogous simulation of figure 4.8b considering a solitonic anti-vortex confirms the previous considerations about the relation between the vorticity sign and the observation of the twist in the solitonic plane.

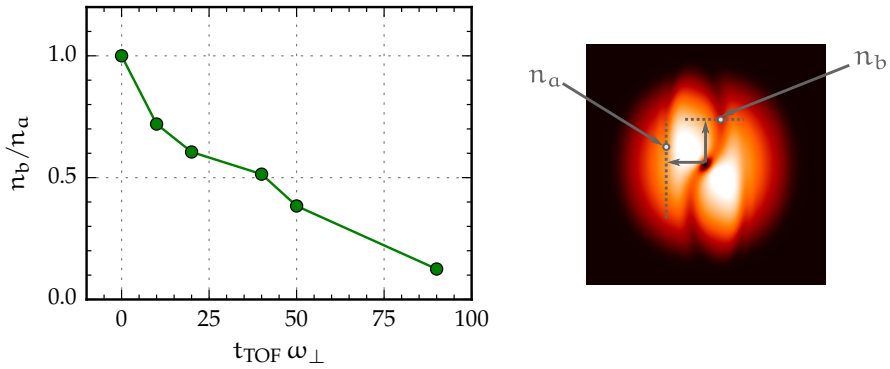

Figure 4.11: Evolution of the contrast of the transverse depletion for a solitonic vortex simulated in an expanding condensate. Before the release from the trap the density is essentially isotropic around the core, hence $n_b/n_a \simeq 1$. During the expansion n_b/n_a decreases, meaning that the solitonic plane appears in the radial direction with an increasing contrast.

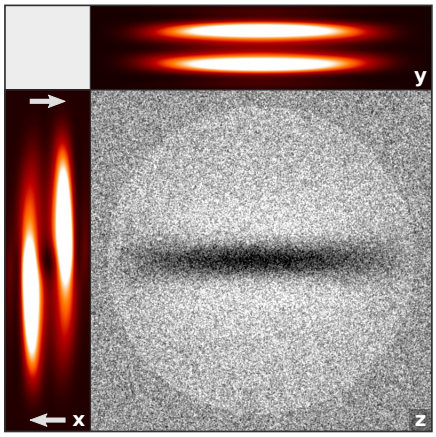

Figure 4.12: Density profile simulated for a solitonic vortex in a condensate after an expansion of 120 ms, with a confinement parameter $\gamma = 10$. Some white noise is added in the axial profile, for a natural comparison with the experimental residuals in figure 4.5a. Here the density depletion is thicker: in order to speed up the calculations the chemical potential is lower than the experimental one, hence leading to a larger healing length.

4.4 EVOLUTION OF A SOLITONIC VORTEX

The identification of defects as solitonic vortices allows us to explain the long defect lifetime observed while studying the KZM, since they are energetically stable and topologically protected in elongated 3D systems. However the details of the defect formation remain unclear. In particular it is unknown if solitonic vortices arise directly from the merging of random phase domains formed via the KZM, or if solitons are actually created after the transition crossing as suggested by Zurek (2009) for cigar-shaped condensates. In the latter possibility the solitons may eventually decay into less energetic structures on a timescale of the order of the transverse oscillation period, as studied by Becker et al. (2013). These two hypothesis cannot be easily distinguished in our experiments, since at the first instants after the BEC transition the condensate is not well-formed and defects cannot be directly observed. We can only probe the final products of the defect formation process, which are long living solitonic vortices, i. e., the excitations with lowest energy for elongated systems such ours (Brand et al., 2002; Komineas et al., 2003; Mateo et al., 2014).

In order to explore the possible *defect evolution* we measure the average number of defects as a function of the time t_e from the BEC transition. We follow a procedure which is similar to the one exploited for the measurement of the defect lifetime presented in section 3.5, but extending the explored temporal interval to instants closer to the critical point. We consider a constant RF evaporation rate of $320\,\mathrm{kHz\,s^{-1}}$ across the transition. We obtain almost pure condensates at 1.22 MHz, which is 25 kHz above the trap bottom. The quench ramp ends about 400 ms after the transition, occurring around 1.34 MHz. Following the sketch reported in the upper part of figure 4.13, when considering short evolution times we interrupt the evaporation ramp before reaching its end. Conversely, while exploring longer evolutions, we add a constant RF shield in order to maintain the temperature the atomic sample. This measurement has been repeated also by stopping the evaporation ramp always at 1.32 MHz, just after the transition point, where the temperature is about 650 nK.

The measurements of the defect lifetime, reported in figure 4.13, show that the defect number is significantly higher before the ramp completion. Moreover the results suggest the presence of *two defect decay timescales*. The fastest one is limited to a short interval after the BEC transition, where for the two series we measure an average decay time $\tau = 105(25)\,\mathrm{ms}$, obtained by fitting an exponential curve with offset to the data with $t_e \lesssim 400\,\mathrm{ms}$. After such a time the average number of defects becomes of the order of 1.

One may argue that this initial decay could be a spurious effect related to the undergoing evaporative cooling, since for the series with lower final frequency the points with a short evolution time refer to

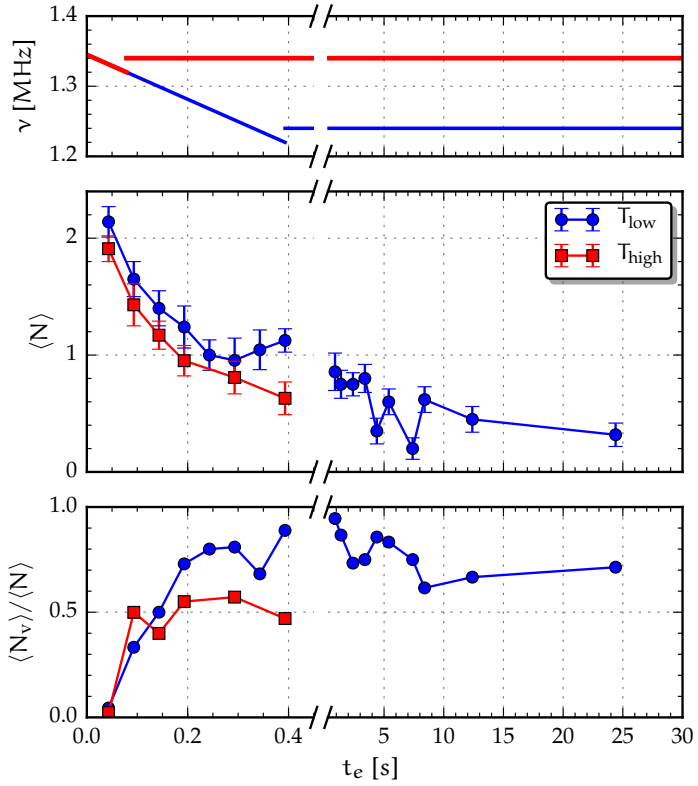

Figure 4.13: Average number of defects plotted as a function of the evolution time from the transition point. The two series refer to different final frequencies of the RF evaporation ramp, as sketched on the top. The bottom plot reports the fraction of the total counted defects that we can identify with reliability as vortices (the big error bars are omitted here).

uncompleted ramps. However a similar behavior is observed also in the data set at higher temperature, where the ramp is interrupted at $t_e \simeq 70\,ms$: this allows us to exclude that the evaporation plays a direct role in the time interval considered for these measurements. The defects which survive to the first fast decay can live for a very long time, with a sizable fraction of defects being still present 25 s after the transition. This long lifetime for solitonic vortices is consistent with the observations reported in chapter 3 and in our article on the KZ scaling (Lamporesi et al., 2013b).

Figure 4.13 also reports the ratio between the number of defects that we clearly identify as solitonic vortices $\langle N_v \rangle$, i. e., where we observe a vortex line along the axial direction or a twist in the radial images, and the total number of defects $\langle N \rangle$, i. e., possibly including all other kinds of defects, such as solitons. The data set at lower temperature shows that the probability of identifying a defect as a SV increases from 0 to almost 1, which means that after a long evolution we identify essentially all defects as vortices. However we cannot find an unambiguous connection between this observation and possible defect evolution paths. In fact this behavior is also related to the finite signal-to-noise ratio, which increases as the evaporation ramp removes atoms from the thermal fraction. This hypothesis can be supported observing the series at higher temperature, where, apart from the first point, $\langle N_v \rangle / \langle N \rangle$ is lower and it does not increase with time, as one would expect considering that, in such case, the evaporation ramp is interrupted at a higher frequency. The signal-to-noise ratio sets also the limit for short evolutions, since the interpretation of images for $t_e \lesssim 50\,ms$ is not possible.

The results for the defect lifetime discussed here suggest the presence of decay processes happening on different timescales, but clear indications about the defect evolution can be hardly extracted. In fact these measurements are based on the averaging of the defect counts over many independent experimental sequences. In order to overcome some of these limits, as described in the article on the SV dynamics (Serafini et al., 2015), we also implemented a non-destructive imaging of the condensate, which allowed us to track the position of single defects during their evolution in time. Those measurements opened for the possibility of a quantitative study of the defect decay, whose possible role on the KZ scaling will be discussed in the following chapter 5. One limit of the non-destructive imagining technique that we implemented is that it is functional for the observation defects only in almost pure condensates. In particular it does not allow to study the defects near to the phase transition, whose dynamics should be further investigated.

5 CHARACTERIZATION OF THE DEFECT NUMBER SCALING

In chapter 3 I described the spontaneous formation of phase defects in elongated gases after temperature quenches across the BEC transition, whose number scales as a power law of the quench time, as predicted by the KZM. Those defects were in the first instance interpreted as solitons. As I discussed in chapter 4, the observation of an unexpectedly long defect lifetime suggested us to study deeper the nature of the defects produced in our system: experimental and numerical investigations allowed us to identify them as solitonic vortices rather than solitons. In this chapter I will present some further measurements that were suggested by such observations.

In order to properly consider the finite lifetime of defects, in section 5.1 I will discuss a new procedure for the temperature quench ramps, and I will also recall the role of dimensionality in the KZM with a possible approach for its study. The results for the defect number scaling measured using this new method are presented in section 5.2. The measurements evidenced the presence of an unexpected saturation in the defect counts for fast quenches, that will be discussed in the following section 5.3. The possible dependence of the defect number scaling on the confinement regime will be finally discussed in section 5.4.

5.1 NEW APPROACH TO MEASURING THE KZM

5.1.1 Quench method and defect decay

Regarding the number of defects that are spontaneously produced in our condensates, an exponential decay happening on a timescale of the order of 1 s was already reported in our first article on the KZM (Lamporesi et al., 2013b). A similar long lifetime was also confirmed in our subsequent work on solitonic vortices (Donadello et al., 2014), and the decay dynamics was afterward investigated with a real-time imaging technique (Serafini et al., 2015). As introduced in section 1.2, the KZM predicts the scaling laws for the number of defects produced after a quench. It must be noted that the theory deals with the density of topological defects at their creation, assuming that they have a stable nature and not considering their evolution after the quench. In the presence of *post-quench dynamics* the link between the power law of equation (1.25) and the actually measured defect number must be further investigated. In particular, in an experiment involving defect

counting, the defects might change their nature or decay from their formation, before they are observed.

In order to take into account these effects related to the finite defect lifetime, the instant of the defect creation should be known. Following the KZM simplified scheme including the adiabatic-frozen-adiabatic representation, one can argue that the freeze-out time $\hat{t}$ of equation (1.15) is the right time, before the transition, that should be considered for the determination of the number of defects originally formed in the system. However, in order to observe those defects, the critical point must be crossed such that the order parameter becomes macroscopically occupied.

Moreover $\hat{t}$ is hard to estimate in experiments for several reasons: its definition depends on microscopic parameters that are not well defined in the theory, such as the time τ_0 setting the relaxation timescale for the order parameter. Even if for dilute gases one may speculate τ_0 to be of the order of the collisional time, a numeric factor should also be considered in the definition of $\hat{t}$, reflecting the effective size $f\hat{\xi}$ of the phase domains formed after the quench, with the value of f depending on the specific model (del Campo et al., 2014). Finally it must be noted that a finite time is needed for the actual formation of defects from an arbitrary phase pattern, i. e., the system has to relax and reach a metastable state.

The impossibility to unambiguously identify the instant of defect creation suggests us to take the *transition point* as a reference for the defect evolution: occurring in the middle of the frozen interval relevant for the KZM, the critical point seems to be a plausible approximation for the defect formation. Moreover, from a practical point of view, the transition point is experimentally identifiable in a clear way, as it can be seen from the example of figure 5.1.

As described in chapter 3, our first approach to measurements on the KZM was based on temperature quenches performed while keeping the initial and final temperatures constant, in order to produce almost pure condensates for any given quench rate. This was aimed to the optimization of the visibility of defects: the possible presence of a big thermal atomic fraction introduces a broad background signal with a Gaussian profile in absorption images, reducing the contrast of the optical density depletion associated to a defect. Following the sketch in figure 3.4, within that quench method the evaporation ramps used for the preparation of the BECs were all equivalent except for the slope of the portion around the transition: the RF limits were kept fixed while the timing was changed, hence resulting in ramps with different durations for different quench rates. This procedure was used for our first measurements on the defect number scaling (Lamporesi et al., 2013b), where we changed the length of the ramps from 140 ms (fastest ramps) up to more than 2 s (slowest ramps). Such a variation in the experimental sequence duration can be relevant on

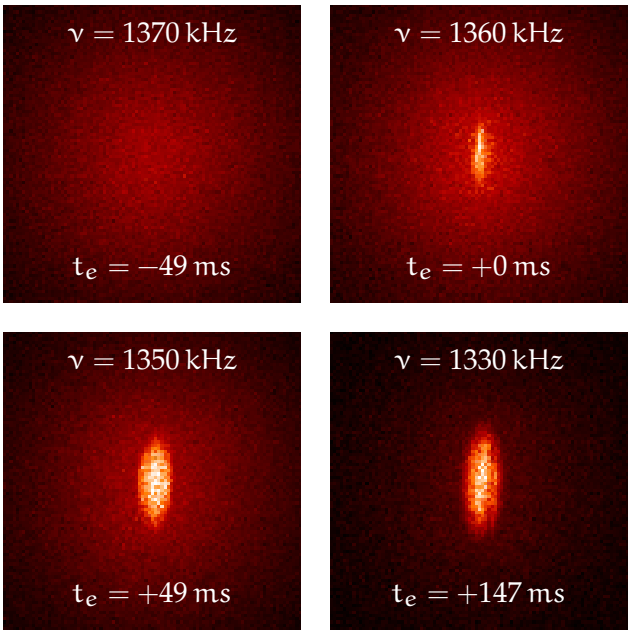

Figure 5.1: Sequence of experimental absorption images of atomic samples around the BEC transition, occurring at $\nu_c \simeq 1360\,\mathrm{kHz}$ for a RF ramp of $203\,\mathrm{kHz\,s^{-1}}$ with $AR = 10.1$. These radial pictures are taken after a TOF of 50 ms. The timescale is relative to the transition point: at $t_e = 0\,\mathrm{ms}$ a small condensate fraction of about 1 % of the total sample appears in the cloud, and it grows for $t_e > 0\,\mathrm{ms}$. In the last picture the condensate is well defined above the thermal background, and a defect is also visible in the density profile. In general for $t_e \lesssim 100\,\mathrm{ms}$ defects are hardly detectable with this imaging technique.

the scale of the defect lifetime, and may eventually alter the measurement of the KZ scaling.

In the new set of measurements that are presented in this chapter we considered a different quench method, where the defect number is measured after a *constant evolution time* t_e from the transition point. In order to apply this new procedure, for each experimental condition we need to precisely determine the critical evaporation frequency ν_c and temperature T_c where the BEC transition occurs. Given an arbitrarily chosen evolution time t_e starting at the transition, the quench ramps have to be modified consequently to the determination of ν_c.

SLOW RAMPS If t_e is reached before the end of the quench ramp the evaporation is interrupted before its completion, the atoms are released from the trap and imaged after TOF. A sizable fraction of atoms will remain in the non-condensed state.

FAST RAMPS If the given t_e ends after the ramp completion a waiting time is added in the sequence before taking the picture. During the waiting time we keep a constant evaporation threshold in order to prevent any heating of the atomic sample. This RF shield does not participate to the dynamics of the quench, since its frequency is well above the limits of the quench ramp.

A very small evolution time would be ideal since it would reduce the influence of the decay of defects on measurements. However, at the very early instants after the transition the condensate fraction is small, and the visibility of defects is limited by the low signal-to-noise ratio in absorption images taken after TOF. Therefore a compromise must be found between defect visibility and minimization of t_e. Different probing methods, not implemented here, may partially overcome these problems, such as the measurement of the phase correlation function of the condensate (Navon et al., 2015). Anyhow it should be noted that the KZ model focuses only on the scaling of the defect density, and it is not meant to provide a quantitative prediction of the absolute values of the defect number.

The speed of the quench is described by the quench time τ_Q that was defined while discussing the KZ theory in section 1.2.1. For a linear temperature quench with a constant time derivative $\dot{T}$, the reduced control parameter of the transition can be expressed as

$$\varepsilon(t) = \frac{T_c - T(t)}{T_c} = 1 - \frac{t\,\dot{T}}{T_c}\,, \tag{5.1}$$

whose derivative defines the quench rate*:

$$\dot{\varepsilon} = -\dot{T}\frac{1}{T_c} = \frac{\partial T}{\partial t}\frac{1}{T_c}\,. \tag{5.2}$$

* For simplicity $\frac{\partial T}{\partial t}$ and $\frac{\partial \nu}{\partial t}$ are defined positive. Therefore, considering a reduction of the control parameter in time, we have $\frac{\partial T}{\partial t} = -\dot{T}$ and $\frac{\partial \nu}{\partial t} = -\dot{\nu}$.

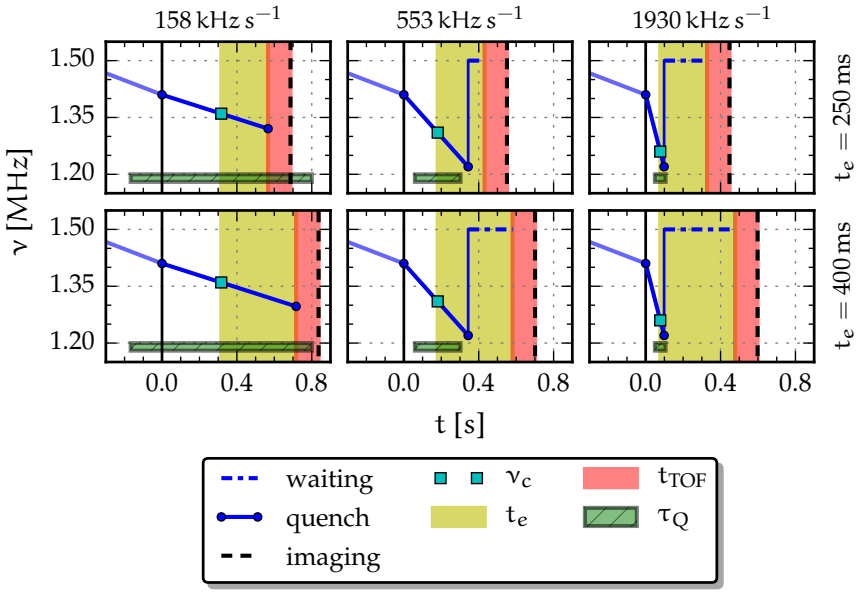

Figure 5.2: Experimental quench sequence for three ramp speed examples (columns) and two different values of evolution time (rows), relative to the measurements with aspect ratio AR = 10.1. The evaporation frequency ν is plotted as a function of time relative to the start of the final quench ramp (solid blue). Negative times refer to the RF evaporative cooling for the preparation of the samples, common to all quenches and omitted here. The critical point ν_c of the BEC transition is reported for each quench ramp (cyan squares). The evolution time t_e is kept constant relative to the transition (shadowed in yellow). After a time t_e the sample is released, let expand for a fixed TOF of 120 ms (shadowed in red), and finally observed with absorption imaging (dashed). For faster quenches a waiting time is eventually added keeping a constant RF shield (dot-dashed blue). The extent of the quench time τ_Q is reported for comparison (green).

Experimentally the speed of the temperature quench $\frac{\partial T}{\partial t}$ is controlled with the slope of the RF evaporation ramp $\frac{\partial \nu}{\partial t}$. Therefore, following its definition given in equation (1.12), the *quench time* can be calculated from the critical temperature T_c and the proportionality factor $\frac{\partial T}{\partial \nu}$ between temperature and evaporation frequency around the transition:

$$\tau_Q = \frac{1}{\dot{\varepsilon}} = \frac{T_c}{\frac{\partial T}{\partial t}} = \frac{T_c}{\frac{\partial T}{\partial \nu}\frac{\partial \nu}{\partial t}} \,. \tag{5.3}$$

It should be noted that this definition of the quench time slightly differs from the one given in chapter 3 accordingly with our article on the KZM (Lamporesi et al., 2013b), where τ_Q was defined in a simpler way as $\tau_Q \propto (\partial\nu/\partial t)^{-1}$. The quench procedure adopted for the measurements on the KZ scaling presented in this chapter is sketched in figure 5.2, considering different values of τ_Q and t_e.

5.1.2 Changing the dimensionality

Following the discussion of section 1.2.3 on the KZ theory, the exponent α of the power law describing the defect number scaling and defined in equation (1.26) is proportional to $(D - d)$, i. e., the difference between system and defect dimensions. The *dimensionality* of a condensate depends on the confinement regime, that, for axially symmetric harmonic potentials, is described by the dimensionless parameter γ, defined in equation (1.50) while discussing the stability of phase defects. Even if in our experiments we produce condensates in an elongated trap, our cigar-shaped system can be considered 3D, therefore with $D = 3$, since in our standard conditions we have $\gamma \gg 1$.

Regarding the defect dimensionality, initially the defects were interpreted as solitons (Lamporesi et al., 2013b), having a planar geometry in 3D systems, hence with $d = 2$. However, as described in chapter 4, we subsequently identified those defects as solitonic vortices (Donadello et al., 2014). This kind of defect has a nontrivial structure, showing characteristics in common with solitons and vortices: however, from a geometrical point of view, a SV is a vortical filament in an elongated system, and therefore in first approximation one may assume that $d = 1$. This evolution in the comprehension of the defect nature suggests us to better investigate the role of dimensionality in the KZM.

As introduced in section 1.3.2, theoretical studies show that the confinement regime determines the type of stable defects in condensates (Brand et al., 2002; Komineas et al., 2003; Mateo et al., 2014): when the confinement parameter γ is small compared to unity solitons are expected to be stable, while the SV becomes the least energetic state for bigger values of γ. Here we are going to deal with the influence of dimensionality on the defect number scaling: in particular, considering the dependence of γ on the radial trapping frequency, we want to understand what happens to the measurements while changing the transverse confinement.

The values of the power-law exponent α predicted by the KZ theory in different conditions were reported in table 1.1 considering the critical exponents from the F-model (Hohenberg et al., 1977). Starting from our supposed situation of vortices in an inhomogeneous 3D system, i. e., with $(D - d) = 2$, equation (1.26b) predicts $\alpha = \frac{7}{3}$. Increasing the radial confinement one may expect reduction of a factor of 2 in the power-law exponent, since the system should tend to the regime where γ is small and solitons are stable, i. e., with $(D - d) = 1$ and $\alpha = \frac{7}{6}$.

A tighter radial confinement reflects into a more elongated shape of the BEC, which, in an axially symmetric trap, can be described with the *aspect ratio*. This quantity is defined as

$$AR = \frac{R_{\parallel}}{R_{\perp}} = \frac{\omega_{\perp}}{\omega_{\parallel}}, \tag{5.4}$$

where, for a given axis i, R_i is the Thomas–Fermi radius of the condensate defined in equation (1.44), and $\frac{\omega_i}{2\pi}$ is the respective trapping frequency. Here we take AR as a convenient measure of the confinement condition.

The aspect ratio of a cigar-shaped Ioffe–Pritchard trap like our can be easily changed through the magnitude of the magnetic field bias B_0, which is aligned in the direction of the symmetry axis and sets the bottom of the trap potential (Ketterle et al., 1999). In fact the strength of the magnetic field in the harmonic approximation can be expressed in cylindrical coordinates as

$$B(r,z) \simeq B_0 + \frac{1}{2}\left(\frac{B'^2}{B_0} - \frac{B''}{2}\right) r^2 + \frac{1}{2} B'' z^2, \tag{5.5}$$

with $r^2 = x^2 + y^2$, B' the field gradient, and B'' the field curvature. The squared radial and axial trapping frequencies of the resulting magnetic potential are respectively

$$\omega_{\perp}^2 = \frac{m_F g_F \mu_B}{m}\left(\frac{B'^2}{B_0} - \frac{B''}{2}\right) \tag{5.6a}$$

$$\omega_{\parallel}^2 = \frac{m_F g_F \mu_B}{m} B'', \tag{5.6b}$$

with m the atomic mass, m_F the Zeeman sub-level of trapped atoms, g_F the hyperfine Landé g-factor, and μ_B the Bohr magneton. Therefore with B_0 we can change the radial confinement while leaving the axial trapping frequency constant, hence varying the aspect ratio of the condensate.

The bias field B_0 in our setup is controlled using a pair of secondary coils, where a continuous current of the order of few hundreds of mA can be precisely programmed through the digital control system described in chapter 2. In practice we vary the bias current in order to find the condition where, using an evaporation ramp with a given final frequency ν_0, the BEC atoms are completely evaporated, which means that the resonance of the RF coupling reached the minimum of the trapping potential:

$$B_0 = \frac{h\nu_0}{\mu_B m_F g_F}. \tag{5.7}$$

For this reason the *trap bottom* can be conveniently expressed in frequency units. For each value of ν_0 we measure the radial trapping frequency $\omega_{\perp}$ by exciting the dipole oscillatory mode of a trapped condensate with a pulse of a uniform magnetic field.

Table 5.1: Aspect ratio calculated from the trapping frequencies, measured for the different radial confinement regimes considered in this chapter. The frequency at the trap bottom ν_0 and the limits of the evaporation quench ramp ν_2 and ν_1 are reported for each aspect ratio. The TOF considered for the absorption imaging procedure is also reported.

AR	$\omega_\perp/2\pi$ [Hz]	$\omega_\parallel/2\pi$ [Hz]	ν_0 [kHz]	ν_1 [kHz]	ν_2 [kHz]	t_{TOF} [ms]
5.8(2)	76.3(1)	13.0(5)	3500	3525	3700	150
10.1(4)	131.4(1)	13.0(5)	1195	1220	1410	120
13.4(5)	173.8(1)	13.0(5)	650	690	920	100
16.5(6)	214.1(1)	13.0(5)	450	510	770	80

The measurements presented in the previous chapters were performed with a constant aspect ratio of about 10. Within the new measurements that we are going to present here the aspect ratio is varied between 5.8 and 16.5, as reported in table 5.1 and figure 5.3. We are not able to explore higher AR values because of the presence in our setup of electrical noise in the spectral region $\lesssim 400\,\mathrm{kHz}$, hence setting a lower limit for the trap bottom. Since we are mainly interested in the physics of elongated systems, we do not explore lower aspect ratio values.

Table 5.1 also reports the evaporation frequency limits ν_2 and ν_1 of the linear quench ramps, fixed for each aspect ratio, which are varied accordingly to the trap bottom ν_0 in order to always include the transition point ν_c and to produce almost pure condensates at the ramp completion. The expansion time considered during the imaging procedure is reported in the same table. We change the TOF duration in order to keep a constant defect visibility for the different AR values, since during the free expansion a cigar-shaped condensate inverts its aspect ratio turning into pancake-shaped, with the speed of the radial expansion depending on the transverse confinement (Castin et al., 1996; Ernst et al., 1998).

5.1.3 Characterization of the BEC transition

In order to control the defect evolution time we need to precisely characterize the BEC *transition point*, whose properties depend on the experimental parameters, such as the confinement regime, the quench rate, and the atom number. For each value of aspect ratio AR and evaporation speed $\frac{\partial \nu}{\partial t}$ we image the system at different points of the RF ramp, determining the threshold value ν_c for the observation of the condensate as in figure 5.1. The temperature and atom number

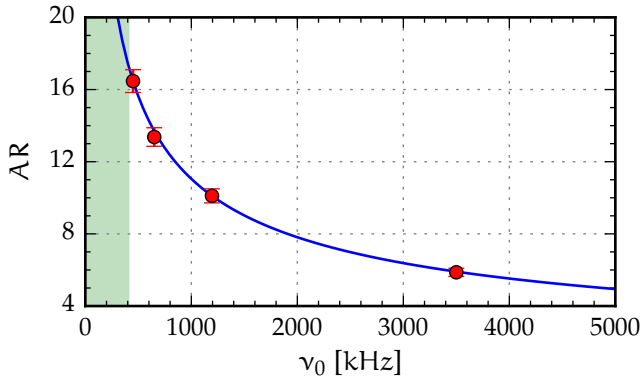

Figure 5.3: Aspect ratio at different values of the trap bottom, varied with the magnitude of the magnetic field bias. The solid line represents the theoretical behavior. The aspect ratio is calculated from the trapping frequencies measured in the different conditions. The shadowed interval refers to values of ν_0 which are not accessible in our setup because of electrical noise.

around the transition are measured from the atomic distribution after ballistic expansion: as an example, the characterization of $T(\nu)$ for a series of quench rates with $AR = 5.8$ is reported in figure 5.4. In order to compare measurements taken in different experimental conditions, we keep the atom number at the transition constant by controlling the loading of the MOT during the initial stages of the experimental procedure, obtaining on average $N_c = 27(1) \times 10^6$ atoms.

The values of the critical frequency ν_c, relative to the trap bottom ν_0, are plotted in figure 5.5 as a function of the evaporation speed for the different values of AR. With faster quenches the transition occurs at lower RF values, i. e., deeper in the trapping potential. This may be explained with a lower cooling efficiency when the cut in thermal distribution introduced by the forced evaporation is more abrupt, reflecting also in a lower number of atoms in the condensed fraction after the quench procedure. In fact, from figure 5.6 we can observe that, even if the number of atoms at the transition N_c is kept almost constant, the number of atoms in the final condensate N_0 varies significantly with the quench rate, both because of the reduced cooling efficiency for fast ramps and the incomplete evaporation for slow ramps.

Following the definition of τ_Q given in equation (5.3), the knowledge of T_c and $\frac{\partial T}{\partial \nu}$ is needed case-by-case for the determination of the quench time. As it can be observed from figure 5.7, the critical temperature T_c is higher for higher aspect ratios and it decreases with the ramp speed as a consequence of the behavior of ν_c. The value of $\frac{\partial T}{\partial \nu}$ is determined as the slope of the linear function fitting the temperature measured around T_c, as in the example of figure 5.4 for the characterization of $T(\nu)$. The results for $\frac{\partial T}{\partial \nu}$, plotted in figure 5.8 as

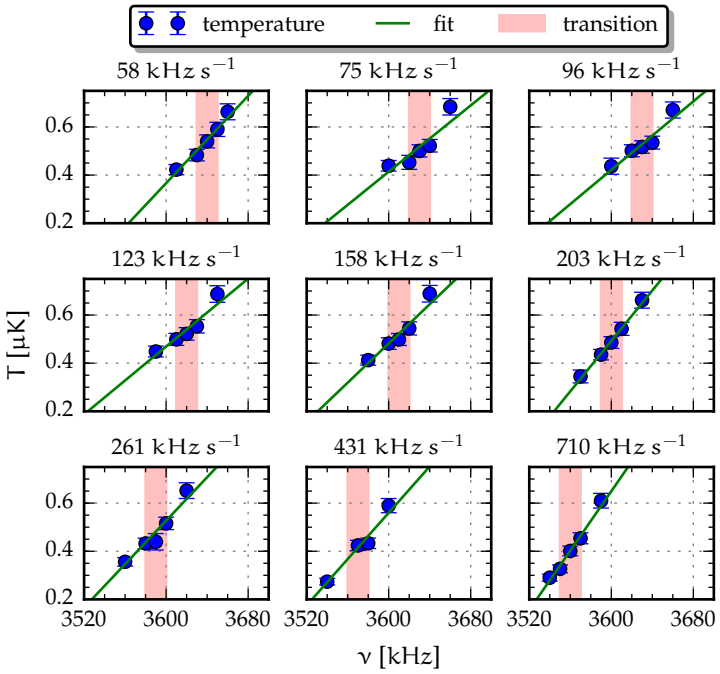

Figure 5.4: Characterization of the temperature around the BEC transition, plotted as a function of the evaporation frequency for different values of the evaporation rate. Each point is the average over a couple of shots taken after 50 ms of TOF with magnetic levitation. This set of plots refers to the series with AR = 5.8. The BEC transition occurs in the shadowed region. Each ramp is fitted with a linear function, and the fit parameters are used to determine T_c and $\frac{\partial T}{\partial \nu}$.

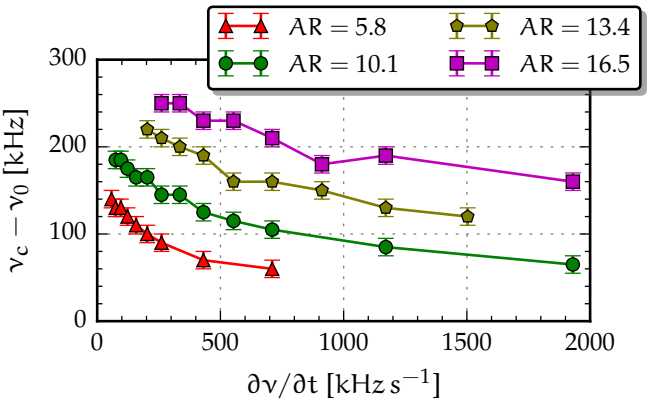

Figure 5.5: Evaporation frequency at the BEC transition point plotted as a function of the ramp speed for different aspect ratios. The RF is relative to the trap bottom.

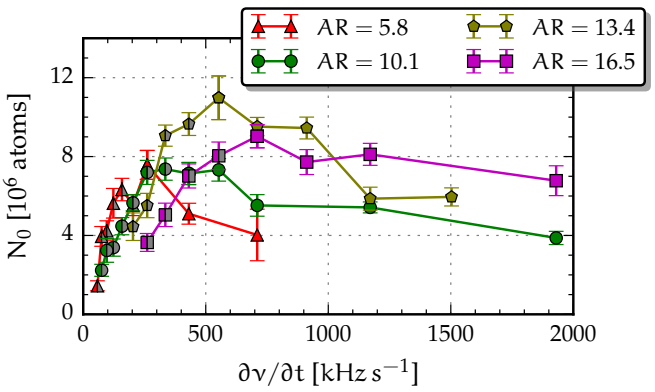

Figure 5.6: Final number of atoms in the condensed fraction at the end of the quench ramp, plotted as a function of the evaporation speed for different aspect ratios and considering an evolution time $t_e = 250\,\mathrm{ms}$. The atoms are fewer for fastest ramps because of the reduced evaporative cooling efficiency, and for slowest ramps because in those cases t_e ends before obtaining pure condensates. The half-filled points refer to the uncompleted ramps.

a function of $\frac{\partial\nu}{\partial t}$ and AR, do not show any evident trend with the experimental parameters. Therefore, while applying the definition of τ_Q, we consider its average value $\frac{\partial T}{\partial \nu} = 4.5(9)\,\mathrm{nK\,kHz^{-1}}$. From this measurement we can estimate the evaporative truncation parameter (Ketterle et al., 1996a) for our system as

$$\eta = \left(\frac{k_B}{h}\frac{\partial T}{\partial \nu}\right)^{-1} = 11(2)\,. \tag{5.8}$$

5.1.4 Defect number counting

Once the quench procedure has been completed, the atomic cloud is released from the trap and let to expand in the presence of a levitating magnetic field gradient. After TOF the atomic distribution is probed with absorption imaging. As it can be understood from the sketch in figure 5.2, for a given evolution time t_e the slowest evaporation ramps can end when a fraction of atoms is still in the non-condensed state, possibly reducing the contrast of defect signals in the experimental pictures. However, using the triaxial imaging described in section 4.2.1, we can identify the defects with reliability even in the presence of a sizable thermal fraction, without the need of the tomographic technique described in section 3.2 and used for the first KZM measurements. Moreover, in order to improve the contrast of defects, we apply the image processing method introduced for the characterization of solitonic vortices, hence observing the residuals of a suitable function fitting the experimental axial images. The defect visibility is also enhanced by reducing the shot noise of pictures

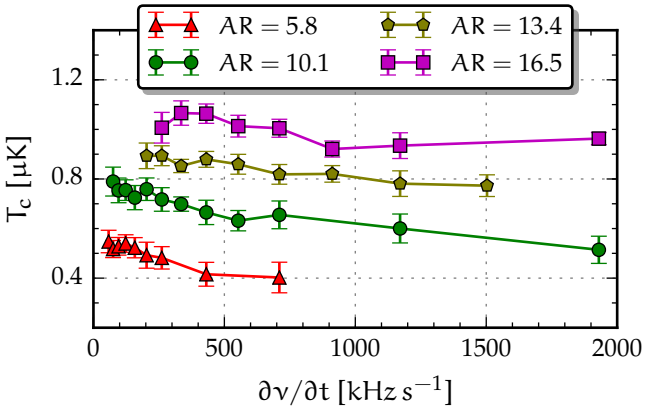

Figure 5.7: Critical temperature at the BEC transition as a function of the cooling speed and aspect ratio. The temperature is measured from the Gaussian width of the thermal atomic distribution after TOF at the critical evaporation frequency ν_c.

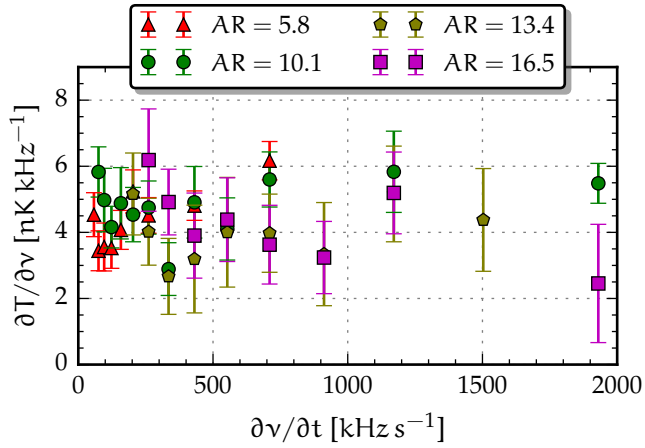

Figure 5.8: Proportionality factor between temperature and evaporation frequency, whose value is extracted from the characterization of $T(\nu)$ around the BEC transition, as in the example of figure 5.4. Apparently any unambiguous trend of $\frac{\partial T}{\partial \nu}$ with the ramp speed and the aspect ratio can be extracted from these results, since each point is consistent with others within the error bars.

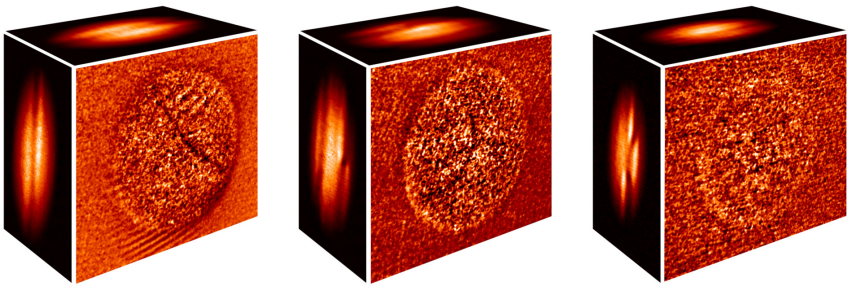

Figure 5.9: Observation of the condensate after 120 ms of expansion, with the absorption images taken along the three orthogonal axes of the trap and referring to the series with $AR = 10.1$. In the first picture we clearly observe a single SV with a tilted nodal line. In each other image we count 2 defects. The defect counting is not always unambiguous, especially when more than 3 defects are present or when the thermal fraction is big. Often the comparison between the observations along all the three imaging axes is necessary to assign the defect number to an experimental run.

with Gaussian filtering. Samples of 3D reconstructions of condensates containing solitonic vortices are reported in figure 5.9.

We tried to implement an automatic technique for defect counting via software analysis of the experimental images. The first attempt was based on pattern recognition algorithms. This method was abandoned since it resulted to be complex and unreliable for the identification of defects with very different shapes as in our case, which often need the human interpretation in order to disambiguate the pattern. The second approach that we followed was based on the analysis of the total fit residuals of images. Also in this case the results were inconclusive, since it was not possible to find a direct connection between the number of defects and the image residuals, whose sum strongly depends on the image noise and on the shape of defects, varying shot-to-shot. Therefore the easiest and most reliable method for measuring the defect number resulted to be the human counting of the depleted structures in the BEC, even if this approach can be affected by a small variability due to subjective interpretation.

For each experimental image we determine the single-shot defect number N. Similarly to the previous measurements presented in chapter 3, we repeat the procedure M times in order to extract the *average defect number* $\langle N \rangle$ for each experimental condition. The error bars over $\langle N \rangle$ are calculated as the quadratic sum between the standard error of the mean δN, defined in equation (3.3), and a resolution term $M^{-1/2}$, whose value decreases with the number of shots:

$$\Delta N = \sqrt{\delta N^2 + \frac{1}{M}}\,. \tag{5.9}$$

It must be noted that here the resolution error is different from the one considered in the first KZM measurements and reported in equa-

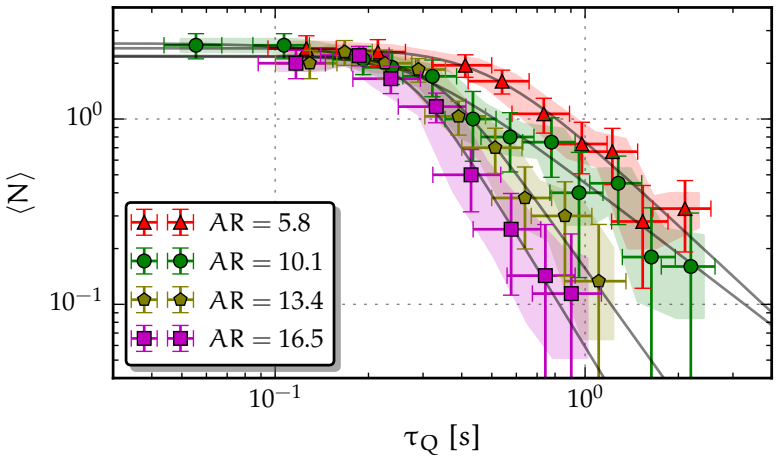

Figure 5.10: Average number of defects measured for different aspect ratios, plotted in log-log scale as a function of the quench time defined in equation (5.3). Each point is averaged over some tens of shots: a larger number of measurements is performed in the case of lower occurrence in order reduce the relative resolution error. The data are fitted with equation (5.10), following a power law for big τ_Q values while saturating when τ_Q is small. The colored shadows highlight the connections between points in the same series considering half of the error bars.

tion (3.4), where, following our article on the topic (Lamporesi et al., 2013b), it was underestimated as M^{-1}. Typically the number of defects counted in each shot varies between $N = 0$ and $N = 4$. In order to get good statistical samples with similar resolutions within the series, for each experimental point we average over a variable number of shots, e. g., $M \sim 10$ when $\langle N \rangle \gtrsim 2$, and $M \sim 70$ when $\langle N \rangle \lesssim 0.2$.

5.2 NEW RESULTS FOR THE DEFECT NUMBER SCALING

The measurements of the average defect number $\langle N \rangle$ as a function of the quench time τ_Q for *different aspect ratios* AR are reported in figure 5.10. For these series we consider an evolution time $t_e = 250\,\mathrm{ms}$, which allows for a good defect visibility also considering the residual thermal fraction for slowest quenches. The results clearly show two distinct regimes within each AR value: for large values of τ_Q we observe a *power-law scaling* of $\langle N \rangle$, whereas for fast quenches with $\tau_Q \lesssim 0.2\,\mathrm{s}$ the average defect number *saturates*, forming a *plateau* where $\langle N \rangle$ remains almost constant independently of τ_Q.

Since the behavior of $\langle N \rangle$ deviates from the simple power-law scaling predicted by the KZM in equation (1.25), we extract the power-law exponent α in the region of big τ_Q and the average defect number

Table 5.2: Parameters of equation (5.10) fitting the data of figure 5.10 for different values of the aspect ratio AR: the average number of defects in the saturated region N_s, the crossover time τ_Q^*, and the power-law exponent α.

AR	N_s	τ_Q^* [s]	α
5.8	2.4(3)	0.49(13)	1.6(4)
10.1	2.6(3)	0.26(8)	1.3(3)
13.4	2.2(3)	0.32(8)	2.3(8)
16.5	2.2(3)	0.27(6)	2.8(9)

N_s in the saturated interval by fitting the experimental data with the following function:

$$N(\tau_Q) = N_s \sqrt{\frac{1}{1 + (\tau_Q/\tau_Q^*)^{2\alpha}}}\,. \tag{5.10}$$

This expression is suitable for the description of our data since it tends to a constant value N_s for $\tau_Q \to 0$, while it decreases as a power law with exponent α for $\tau_Q \to +\infty$. The crossover between the two regimes occurs at the quench time τ_Q^*. The fit results for the series with different aspect ratios of figure 5.10 are reported in table 5.2. We can observe that, whereas α varies by about a factor 2 in the considered range of AR, the level of the plateau N_s is essentially not affected by the aspect ratio, hence suggesting that this saturation phenomenon is intrinsically related to the defect number.

In order to investigate the effects of evolution time on the defect number scaling, we repeat the measurements also for different values of t_e while keeping the aspect ratio fixed to AR = 10.1. In particular we consider *longer evolutions*, since for $t_e < 250\,\mathrm{ms}$ the defect visibility is suppressed for the reasons already explained before. The results are reported in figure 5.11. We can observe that in the region where τ_Q is big the points for the different values of t_e are consistent within their error bars. In particular the exponent α of the power law fitting the data with $\tau_Q \gtrsim 0.2\,\mathrm{s}$ looks insensitive to the evolution time t_e, leading to an average exponent $\alpha = 1.1(2)$. This essentially confirms the robustness of the new quench procedure that has been adopted. The saturated region instead shows a dependence on t_e: qualitatively we can observe that for longer evolutions the saturation occurs at lower values of N_s. This may suggest that some kind of defect decay happens for fast quenches, hence altering the power-law scaling at small τ_Q values.

The defect number saturation and the possible dependence of the exponent α on the aspect ratio will be discussed respectively in the following sections 5.3 and 5.4. Here we only note that for the series with AR = 10.1 of figure 5.10 we measure $\alpha = 1.3(3)$, which is con-

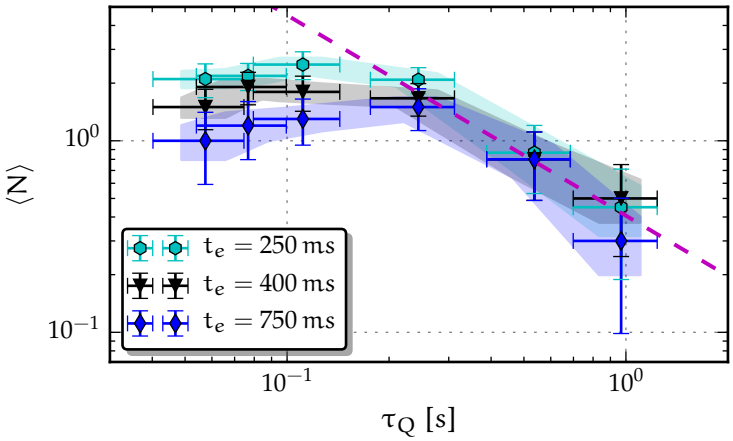

Figure 5.11: This plot is analogous to the one of figure 5.10, but here the different series refer to different evolution times, while the aspect ratio is fixed to AR = 10.1. The power-law behavior at big τ_Q values seems to be uninfluenced by t_e. The dashed line is the power law fitting all the points in the region with $\tau_Q \gtrsim 0.2$ s.

sistent with the value $\alpha = 1.38(6)$ that we formerly measured for the data in figure 3.6†, where the aspect ratio was the same (Lamporesi et al., 2013b). Our first measurements presented in chapter 3 are therefore confirmed, even with the different quench procedure and the different definition for τ_Q that we are considering here. Previously the defect number saturation was not observed in a such clear way, probably because τ_Q was limited at about the threshold value for observing the plateau.

5.3 DEFECT NUMBER SATURATION

5.3.1 Observations for fast quenches

Following the discussion of section 5.1.1, the duration of the quench procedure for the fastest evaporation rates is dominated by the waiting time, added at the end of the evaporation ramp in order to obtain a given evolution time t_e from the transition. One may argue that, even with the implementation of the RF shield, the atomic sample may heat during this long waiting time of the order of t_e. Therefore a possible explanation for the defect number saturation described in the previous section 5.2 would be the increased *thermal effects*, causing a faster decay of defects when τ_Q is smaller.

† The error bars over α are bigger in the new measurements because these include also the uncertainty over τ_Q, not considered in the first ones. Moreover previously we underestimated the defect number resolution error and we considered only the asymptotic standard error.

To explore this possibility we measure the temperature as a function of t_e after a very fast quench with $\tau_Q = 55\,\mathrm{ms}$. In order to precisely determine the temperature we do not finalize the evaporation ramp down to its usual frequency limit of 1.22 MHz, as we do for the series with $AR = 10.1$ to obtain almost pure condensates. Conversely here we interrupt the ramp at 1.24 MHz, hence leaving a fraction of atoms in the non-condensed state. From the results reported in figure 5.12a we can observe that, once the thermal equilibrium is reached some tens of ms after the quench, the temperature remains constant over a long timescale. This allows us to exclude any heating process occurring during the waiting time with the RF shield, and consequently to exclude a role of thermal effects on the defect number saturation.

While acquiring the temperature measurements just presented, we also noted that the apparent aspect ratio‡ of the expanded condensate after a given TOF was changing with the evolution time t_e. The ratio between the radii R'_z and R'_y of the 2D parabola fitting the condensed fraction cloud, respectively along axial and radial directions, is plotted as a function of t_e in figure 5.12b. We observe a damped oscillation of R'_z/R'_y, with a damping constant of 0.30(7) s. The oscillation frequency of about 19.5(2) Hz is consistent with the prediction of $\sqrt{5/2}\,\omega_{\parallel} = 2\pi \times 20.5(8)$ Hz for the breathing mode of a bosonic gas in a cigar-shaped harmonic trap (De Rosi et al., 2015). This collective oscillation is likely triggered with the fast evaporative quench, which introduces an abrupt cut in the thermal distribution. In order to avoid possible spurious effects not considered within the KZM framework, very fast quenches like this one should be avoided while studying the defect number scaling.

Another approach to the study of the defect number saturation can be a statistical analysis. Due to the stochastic nature of the KZM, the integer number of defects N counted in each shot is random and independent. Therefore, as it was discussed in section 3.3.2, a *Poisson statistics* is expected for the defect counts, whose probability distribution is defined as

$$P(N) = \frac{\lambda^k}{k!} e^{-\lambda} \qquad k = 0, 1, 2 \ldots \tag{5.11}$$

with the parameter λ coinciding with the distribution mean. Let us take the experimental data of figure 5.10 in an aggregated way, independently of τ_Q and AR, and group the points according to different intervals of $\langle N \rangle$: this is equivalent to apply data binning along the vertical direction. Since each experimental point is the average over M shots, for each bin we consider the ensemble of the single measurements contributing to $\langle N \rangle$, that is expected to follow the Poisson

‡ The aspect ratio R'_z/R'_y considered here is the one of the condensate after expansion, not the in-trap aspect ratio AR defined in equation (5.4).

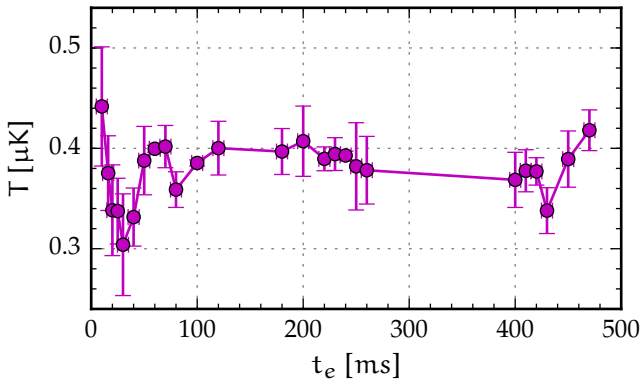

(a) Temperature measured in the non-condensed fraction.

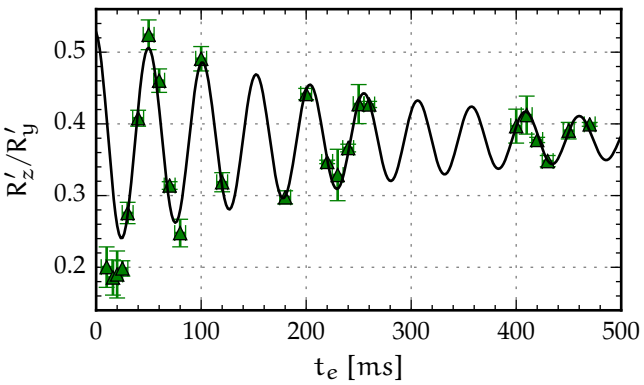

(b) Apparent aspect ratio of the expanded condensate.

Figure 5.12: Characterization the atomic sample after a fast quench with $\tau_Q = 55\,\mathrm{ms}$, obtained with a RF ramp of $\frac{\partial\nu}{\partial t} \simeq 2\,\mathrm{MHz\,s^{-1}}$ for an aspect ratio $AR = 10.1$. The atomic sample is let to evolve for a variable time t_e and imaged after 50 ms of TOF with levitation. The measurements of the temperature (upper plot) show that, after a thermalization transient for $t_e \lesssim 50\,\mathrm{ms}$, the temperature remains substantially stable. The aspect ratio of the condensate after free expansion (lower plot), which must not be confounded with the in-trap AR, shows a damped oscillation corresponding to the breathing mode excited by the abrupt quench.

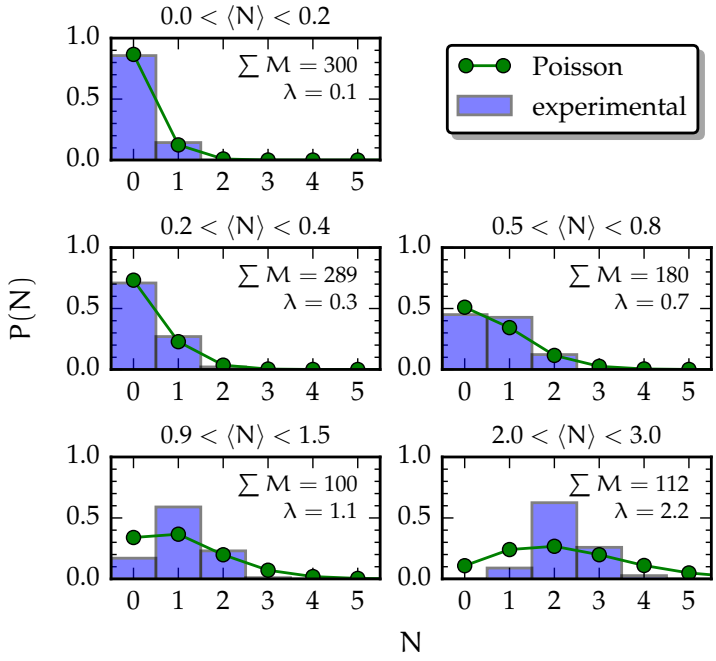

Figure 5.13: Defect counting statistics. A vertical binning in $\langle N \rangle$ has been performed for the data of figure 5.10, independently of AR and τ_Q. Each normalized histogram refers to the occurrence within a bin of the defect number N counted in the single shots. The average number of defects λ and the total number of single-shot measurements $\sum M$ contributing to each histogram are also reported. The experimental histograms are compared with the Poisson distribution calculated using equation (5.11) with mean λ: the agreement with the experimental data is good only for small values of $\langle N \rangle$, i. e., in the non-saturated regime.

statistics being the sum of Poisson-distributed ensembles with similar mean values.

Each histogram of figure 5.13 represents the occurrence distribution of the single-shot defect number N for a given data bin. We can observe that for the bins corresponding to the power-law regime, where $\langle N \rangle \lesssim 1$, there is a good agreement between the experimental data and the Poisson distribution with the same mean value λ. Instead the points relative to the saturated regime, where $\langle N \rangle \gtrsim 1$, clearly do not follow a Poisson statistics. This could be the signature of some additional process that alters the defect counting for fast quenches, i. e., when $\langle N \rangle$ is big.

From the previous observations one may argue that defects decay in different ways for different quench rates. To clarify this point we measure the *lifetime* of defects produced in different conditions: we consider a fast quench in the saturated regime and a slow quench in the power-law interval, with quench time $\tau_{Q_1} = 63(20)\,\mathrm{ms}$ and $\tau_{Q_2} = 0.59(11)\,\mathrm{s}$ respectively. Similarly to the measurements reported

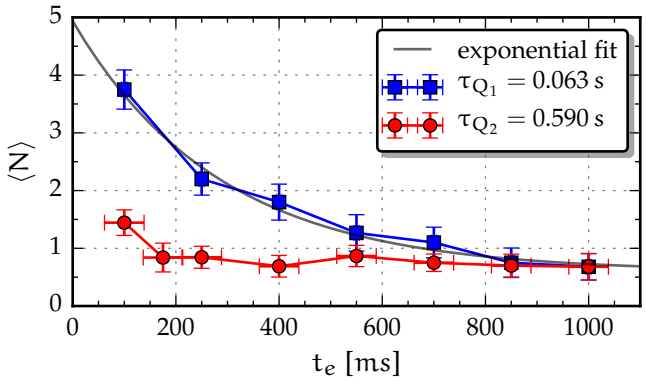

Figure 5.14: Average defect number as a function of the evolution time spent in trap after fast and slow quenches. The measurements are taken with $AR = 10.1$. Within the explored temporal range, an exponential decay in the defect number is evident only for the fast quench (gray line), while both the series present an offset in the defect number.

in sections 3.5 and 4.4, the defect number is measured after a variable evolution time with $AR = 10.1$. From the results reported in figure 5.14 we can observe that the decay plays an important role for the fast ramp, where we observe a *fast decay* for the defect number with an exponential time constant $\tau_1 = 0.29(9)$ s. Conversely for the slow quench the number of defects remains almost constant in time. Both series do not go to zero in the considered range of time, showing an offset of $0.7(2)$ long living defects.

All these observations seem to suggest the presence of *different decay mechanisms* happening on different timescales. In particular the defect number saturation might be explained with a faster decay happening for faster quenches. Such an interpretation can be supported observing the results of figure 5.11, where the fitting power law with $\alpha = 1.1(2)$, extrapolated at $\tau_Q = \tau_{Q_1}$, would give $7(5)$ defects. This value is consistent with the extrapolation of the exponential decay of figure 5.14 for the τ_{Q_1} series, which at $t_e = 0$ ms gives $4.9(7)$ defects. Therefore we can speculate that with a hypothetical zero evolution time, i. e., without the effects of defect decay, the defect number at small τ_Q values would be much higher than what is experimentally measured, whereas in the power-law region $\langle N \rangle$ would be only slightly different.

5.3.2 Effects of the defect decay

The saturation in the defect number scaling discussed in section 5.2 is not contemplated by the KZ theory. Moreover the finite defect lifetime reported in the present chapter and in our previous works (Lamporesi et al., 2013b; Donadello et al., 2014; Serafini et al., 2015) suggests that

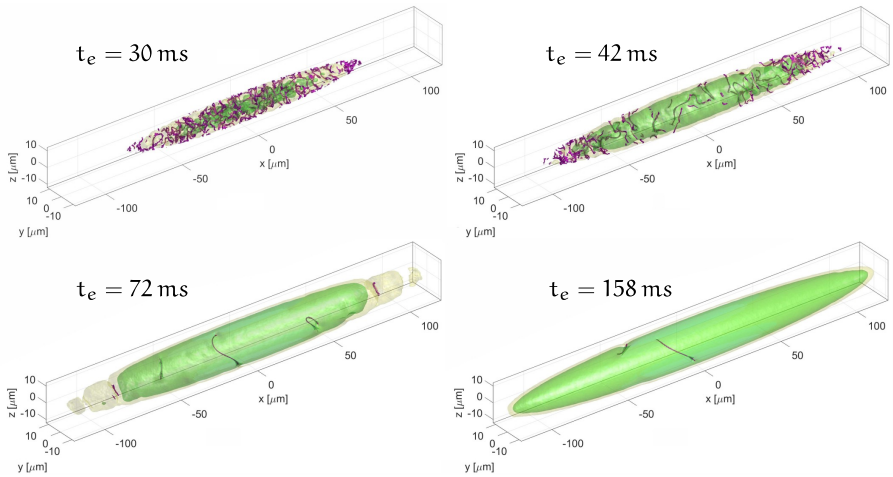

Figure 5.15: Preliminary simulations for an elongated gas quenched across the BEC transition, based on the resolution of the stochastic GPE at different evolution times from the transition point (Liu et al., 2015). The numerical results show the presence of many phase defects (purple) in the growing condensate (green). After the completion of the fast quench, i. e., for $t_e > 42\,ms$, the chaotic system rapidly relaxes to a configuration where the condensate contains only few long living solitonic vortices.

the dynamics happening after the quench may alter the defect counting, since the condensate can be imaged only many tens of ms after the BEC transition, as discussed in section 5.1.1.

Furthermore, recent simulations[§] based on the temporal resolution of the stochastic GPE suggest that in the early moments after the quench the system is highly *turbulent*, with the presence of many vortical lines in the order of tens for a system with parameters similar to our experimental ones (Liu et al., 2015). As it can be observed from the indicative results of figure 5.15, the numerical simulations show a rapid relaxation of the system in the instants following a fast quench, with a fast decay of the defect number down to the order of units. This picture is consistent with our experimental observations, possibly explaining why we hardly count more than 3 solitonic vortices, even for fast quenches. In particular these numerical results confirm that the *post-quench dynamics* must be taken into account for the interpretation of the defect number scaling, and can give important indications about the origin of defect number plateau that we measure after a finite evolution time.

The dynamics for solitonic vortices in our condensates has been experimentally studied using a non-destructive imaging technique which allows to follow single defects while evolving in time, as described in the article on the topic (Serafini et al., 2015). A remarkable result of those measurements was the observation of different decay

§ The unpublished results of the GPE simulations introduced here are prepared by I.-K. Liu (Ph.D. student of S.-C. Gou) and N. P. Proukakis.

rates for different initial defect numbers. In particular, starting from a condition with 3 defects, we measured a faster decay compared to the cases with 2 and 1 defects at the beginning, with exponential decay constants $\tau_3 = 0.49(10)\,s$, $\tau_2 = 1.05(10)\,s$ and $\tau_1 = 0.91(10)\,s$ respectively. These differences in the evolution path were interpreted as the effects of turbulent interactions occurring between 3 defects, whereas for lower defect numbers only the thermal decay should be present. The defect evolution for an initial condition with 4 or more defects was not studied because of the limited statistics, since the occurrence for those cases is low.

The observation of a *defect lifetime* which is dependent on the initial defect number suggests an interpretation for the *saturation* in the average defect number scaling visible in figures 5.10 and 5.11. This would also confirm the hypotheses proposed while discussing the results for the defect number statistics and the defect lifetime, referring to figures 5.13 and 5.14 respectively. In order to understand if the defect evolution can effectively explain our observations, we simulated the effects of defect decay on the defect number scaling at different times from the transition.

As already discussed in the previous sections 3.3.2 and 5.3.1, due to the stochastic nature of the KZM the defect number N at the defect formation follows Poisson statistics. Starting from this assumption, the average defect number after a given time can be predicted by applying independent decay paths separately to the fractions with $N = 1$, $N = 2$ and $N = 3$ of the Poisson distribution with a given mean λ, defined in equation (5.11). With this simple model we are introducing a cut-off for 4 or more defects, since the correspondent lifetimes are unknown, i. e., the cases with $N > 3$ are assumed to decay at the very beginning. Such a speculation is suggested by the faster decay measured for $N = 3$. As it can be evinced from figure 5.16, this approximation becomes stronger when the average defect number $\langle N \rangle$ increases and the probability to find such high values of N is not negligible.

The results for the defect number scaling simulated in the presence of defect decay are reported in figure 5.17, which must be compared with the measurements of figure 5.11. The calculations are performed applying the following steps.

1. We start considering the power law with average exponent $\alpha = 1.1$, fitting the experimental data of figure 5.11 for $\tau_Q \gtrsim 0.2\,s$.

2. The values of $\langle N \rangle$ are extrapolated from this power law over a broad interval in τ_Q, also where the experimental points would saturate. The corresponding Poisson distributions with $\lambda = \langle N \rangle$ are calculated point-by-point, as in the examples of figure 5.16.

3. We take the fractions with $0 < N \leqslant 3$ of these hypothetical distributions as the starting points for the exponential decay

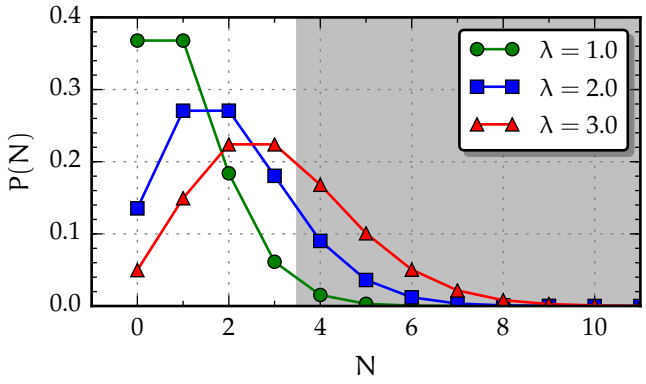

Figure 5.16: Poisson distribution for different mean values. The defect counts with average $\langle N \rangle = \lambda$ are expected to follow this statistics. The shadowed interval represents the fraction of the distribution that is not considered within the calculations for the defect number scaling after defect decay, as described in the text. This cut-off in the distribution represents only the 2 % for $\lambda = 1$, but the neglected probability is much more important, the 35 %, for $\lambda = 3$.

described in the previous paragraphs, hence considering the respective lifetimes τ_1, τ_2 and τ_3 measured while studying the defect dynamics (Serafini et al., 2015). A cut-off for the fractions with $N \geqslant 4$ is introduced in the distributions.

4. For comparison with the experimental data, the final defect number scaling is calculated after the same values of t_e considered for the series of figure 5.11.

5. Finally we normalize the initial power law by an arbitrary constant to overlap the simulated and experimental curves, hence compensating a posteriori the unknown decay that is intrinsically present in the measurements.

From the comparison between figures 5.11 and 5.17 we observe a good qualitative agreement for the series at different evolution times, with an evident deviation from the power-law behavior in the region where τ_Q is small. In particular the plateau scales with t_e similarly in the experimental data and in the simulations, while the power-law scaling shifts rigidly keeping the same exponent α. Moreover, for the curves predicted with our simple model we find values for the crossover time τ_Q^* and the saturated defect number N_s that are compatible with the measurements. Even if the assumptions that we have made are strong and should be supported by extended future measurements, going beyond the qualitative analysis presented here, the defect lifetime can be proposed as a possible explanation for the saturation that we observe in the KZ scaling.

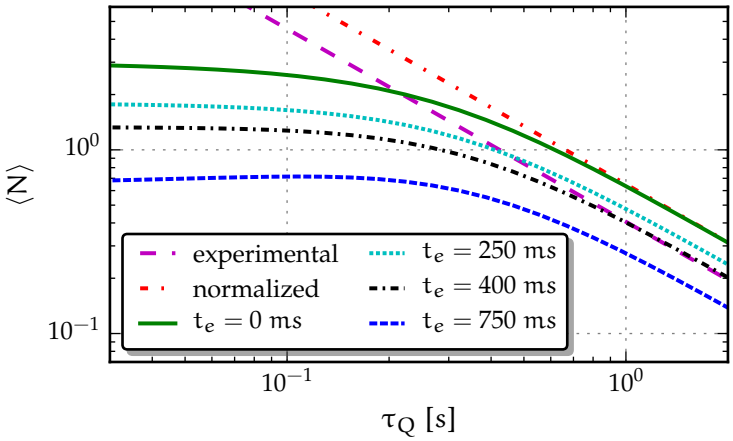

Figure 5.17: Predictions for the defect number scaling including the effects of defect decay, in analogy with the experimental measurements of figure 5.11 after analogous evolution times. The power law fitting the experimental data (dashed purple) is reported also after the arbitrary normalization considered for the calculations (dot-dashed red). For each τ_Q we introduce a cut-off for $N \geqslant 4$ in the probability distribution at $t_e = 0$ ms (solid green), and we calculate the defect number scaling for different values of t_e: we apply an exponential decay to the fractions with different values of N, using the time constants reported in our article on the defect dynamics (Serafini et al., 2015).

5.4 ROLE OF THE DIMENSIONALITY

In section 5.1.2 we discussed the possibility to study the defect number scaling in different confinement regimes in order to test the predictions of the KZ theory. In particular we hypothesized that the power-law exponent α should decrease for a tighter radial confinement, i. e., a *higher aspect ratio*, as a consequence of a possible change in the defect dimensionality and reflecting the spontaneous production of solitons instead of solitonic vortices. In figure 5.18 we report the power-law exponent measured for different values of AR, in relation to the data of figure 5.10 and already reported in table 5.2. The exponent α seems to increase with AR: this behavior is not in agreement with the hypothesis that we initially proposed. Even if we cannot suggest a clear explanation for these results, we can make some observations.

First of all, considering the large experimental error bars we cannot completely exclude that the increasing trend of α is only apparent, since the points are essentially consistent even with a constant behavior. A reduction of the uncertainties would be desirable, however this is not a trivial task: one would need a more precise and reliable method for the characterization of the BEC transition and for the determination of τ_Q. Moreover from equation (5.9) it should be

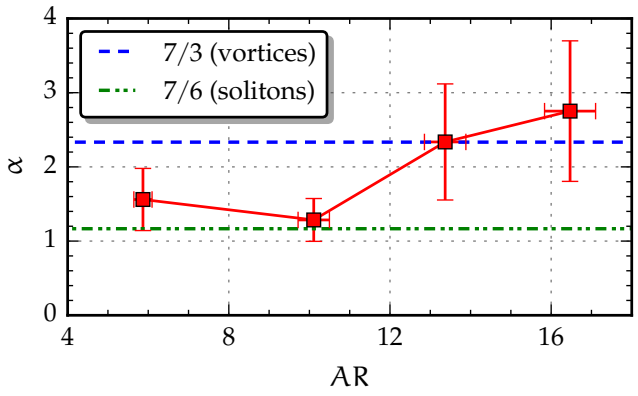

Figure 5.18: Power-law exponents fitting the experimental series of figure 5.10 for different aspect ratios. The predictions of the KZ theory for solitons and vortices in a harmonic 3D regime are plotted for comparison, taking the critical exponents from the F-model (Hohenberg et al., 1977) as in table 1.1.

noted that the resolution error term over $\langle N \rangle$ scales as $\sqrt{1/M}$, with M the number of observations. As an example, to halve an error bar we would have to repeat 4 times the number of experimental runs to average: for an error bar of $\Delta N = 0.1$ this would translate in an addition of about 10 hours of experiments in stable conditions, just for a single experimental point and neglecting the statistical error term δN.

Another aspect that should be considered while interpreting the results for α is that the idea of studying the KZ scaling while changing the aspect ratio was suggested by the discussion on the *confinement parameter* γ in section 5.1.2. From its definition in equation (1.50), this dimensionless parameter is the ratio between the BEC chemical potential and the transverse harmonic oscillator energy. For a harmonically trapped condensate the chemical potential μ can be calculated from the number of condensed atoms N_0 and the trapping frequencies, using the Thomas–Fermi expression of equation (1.45):

$$\mu = \frac{\hbar\omega_{ho}}{2}\left(\frac{15N_0 a}{a_{ho}}\right)^{2/5} . \tag{5.12}$$

Here a_{ho} is the harmonic oscillator length defined in equation (1.41), and ω_{ho} is the geometric mean of the trapping frequencies introduced in equation (3.16). Therefore γ can be expressed as

$$\gamma = \frac{\mu}{\hbar\omega_\perp} = \frac{1}{2}\left(\frac{15^2 m a^2}{\hbar}\frac{\omega_\parallel^2}{\omega_\perp}N_0^2\right)^{1/5} . \tag{5.13}$$

The experimental values of γ relative to the measurements of the defect number scaling are reported in figure 5.19. We can observe that γ varies by about a factor 2 with τ_Q within each data set at constant AR: this is a consequence of the variation of the number of atoms

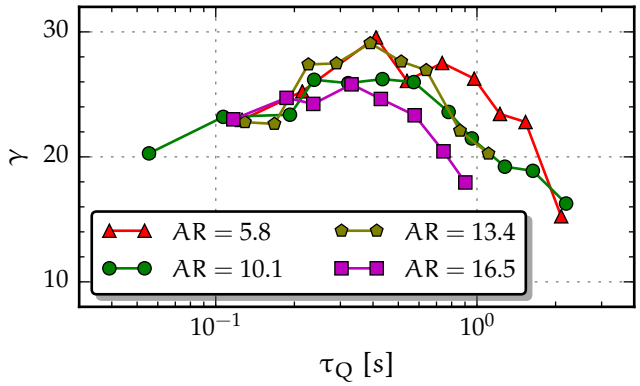

Figure 5.19: Confinement parameter γ calculated with equation (5.13) as a function of the quench time for different aspect ratios. The big error bars are omitted here. As discussed in previous chapters, this dimensionless parameter defines the nature of stable defects in the condensate and, consequently, their dimensionality.

in the final condensate N_0, plotted in figure 5.6. In principle we cannot exclude that this trend of γ may affect the defect dimensionality in a nontrivial way. Conversely we do not observe an unambiguous correlation between γ and AR as we intended to do, and we never approach to the values of γ predicted for the crossover between the different confinement regimes. In fact solitons are expected for smaller values of the confinement parameter, i. e., for γ of the order of unity (Brand et al., 2002; Komineas et al., 2003; Mateo et al., 2014).

Following the observations presented in this section, we conclude that a quantitative comparison between the measurements of power-law exponent α and the predictions for the KZM is not straightforward. A deeper comprehension on the relation between the defect number scaling and the confinement regime is needed in order to explain our experimental data. Finally, our approach for the study of the dimensionality, based on the variation of the aspect ratio, does not seem to be effective for this task. This might suggest future measurements with different methods, e. g., with the implementation of procedures that allow to vary the quench time while keeping γ constant. Further theoretical and experimental studies are therefore required for understanding the role of dimensionality in the KZM.

CONCLUSION

In this thesis I have presented the principal results obtained during my doctorate at the laboratory of ultracold gases in Trento. These are mainly related to the study of the spontaneous formation of defects in harmonically trapped Bose–Einstein condensates, after temperature quenches across the phase transition. In particular, the measurement of the power-law scaling of the defect number with the quench time opened to the possibility of the quantitative study of the Kibble–Zurek mechanism in ultracold gases.

We reported experimental evidences for the identification of the defects spontaneously produced in our condensates as solitonic vortices, providing the first experimental observation and characterization of their phase and density profiles with three-dimensional imaging and matter interferometry after time of flight. Solitonic vortices appear as long lived excitations of the condensate thanks to their topological nature, and they set a link between vortices in bulk systems and solitons in the effective one-dimensional regime. Further studies may be needed to understand how do these defects form at the phase transition, also exploring the interplay between the confinement regime and the defect dimensionality in experiments.

Following the observations on solitonic vortices, we extended the measurements on the defect number scaling proposing a quench procedure that keeps into account of the finite defect lifetime. Our results at constant evolution time showed an unexpected deviation from the simple power-law scaling predicted by the Kibble–Zurek mechanism, with the number of defects saturating at faster quenches. We proposed an interpretation for these observations in terms of the post-quench evolution of defects. However, in order to provide a clear picture, the turbulent dynamics in the presence of many defects needs to be studied in closer detail, both theoretically and experimentally.

The other topic that we addressed is the dependence of the defect number scaling on the radial confinement of our elongated harmonic trap. Even if we observed a possible dependence of the power-law exponent on the condensate aspect ratio, a better understanding of the role of dimensionality on the Kibble–Zurek mechanism is needed for interpreting these results, as well as the effects of thermal dissipation and of temperature inhomogeneities in the gas.

Our observations demonstrate that ultracold gases are promising systems for exploring the critical phenomena occurring at phase transitions, and they inspired subsequent studies for systems in different geometries and confinement regimes. In addition we showed that the production of solitonic vortices via the Kibble–Zurek mechanism

in elongated Bose–Einstein condensates represents a powerful tool for the experimental study of vortex-vortex interactions. This is currently a challenging open problem both in theoretical and experimental physics, with fundamental implications in many domains of condensed matter physics.

PUBLICATIONS

G. Lamporesi, S. Donadello, S. Serafini, and G. Ferrari (2013a). "Compact high-flux source of cold sodium atoms". In: *Rev. Sci. Instrum.* 84.6, p. 063102.

G. Lamporesi, S. Donadello, S. Serafini, F. Dalfovo, and G. Ferrari (2013b). "Spontaneous creation of Kibble–Zurek solitons in a Bose–Einstein condensate". In: *Nature Phys.* 9.10, pp. 656–660.

S. Donadello, S. Serafini, M. Tylutki, L. P. Pitaevskii, F. Dalfovo, G. Lamporesi, and G. Ferrari (2014). "Observation of Solitonic Vortices in Bose–Einstein Condensates". In: *Phys. Rev. Lett.* 113 (6), p. 065302.

M. Tylutki, S. Donadello, S. Serafini, L. P. Pitaevskii, F. Dalfovo, G. Lamporesi, and G. Ferrari (2015). "Solitonic vortices in Bose–Einstein condensates". In: *Eur. Phys. J. Special Topics* 224.3, pp. 577–583.

S. Serafini, M. Barbiero, M. Debortoli, S. Donadello, F. Larcher, F. Dalfovo, G. Lamporesi, and G. Ferrari (2015). "Dynamics and interaction of vortex lines in an elongated Bose–Einstein condensate". In: *Phys. Rev. Lett.* 115.17, p. 170402.

BIBLIOGRAPHY

B. P. Anderson, P. C. Haljan, C. A. Regal, D. L. Feder, L. A. Collins, C. W. Clark, and E. A. Cornell (2001). "Watching Dark Solitons Decay into Vortex Rings in a Bose–Einstein Condensate". In: *Phys. Rev. Lett.* 86 (14), pp. 2926–2929 (cit. on pp. 25, 71, 73).

M. H. Anderson, J. R. Ensher, M. R. Matthews, C. E. Wieman, and E. A. Cornell (1995). "Observation of Bose–Einstein condensation in a dilute atomic vapor". In: *Science* 269.5221, pp. 198–201 (cit. on pp. 19, 29).

M. Arndt, M. B. Dahan, D. Guéry-Odelin, M. Reynolds, and J. Dalibard (1997). "Observation of a zero-energy resonance in Cs-Cs collisions". In: *Phys. Rev. Lett.* 79.4, p. 625 (cit. on p. 65).

C. Bäuerle, Y. M. Bunkov, S. N. Fisher, H. Godfrin, and G. R. Pickett (1996). "Laboratory simulation of cosmic string formation in the early Universe using superfluid ^{3}He". In: *Nature* 382, pp. 332–334 (cit. on pp. 1, 16, 17).

C. Becker, K. Sengstock, P. Schmelcher, P. G. Kevrekidis, and R. Carretero-González (2013). "Inelastic collisions of solitary waves in anisotropic Bose–Einstein condensates: sling-shot events and expanding collision bubbles". In: *New J. Phys.* 15.11, p. 113028 (cit. on pp. 27, 75, 89).

V. Berezinskii (1971). "Destruction of long-range order in one-dimensional and two-dimensional systems having a continuous symmetry group I. classical systems". In: *Sov. Phys. JETP* 32.3, pp. 493–500 (cit. on p. 5).

E. L. Bolda and D. F. Walls (1998). "Detection of Vorticity in Bose–Einstein Condensed Gases by Matter-Wave Interference". In: *Phys. Rev. Lett.* 81 (25), pp. 5477–5480 (cit. on pp. 81, 82).

J. Brand and W. P. Reinhardt (2001). "Generating ring currents, solitons and svortices by stirring a Bose–Einstein condensate in a toroidal trap". In: *J. Phys. B* 34.4, p. L113 (cit. on p. 26).

J. Brand and W. P. Reinhardt (2002). "Solitonic vortices and the fundamental modes of the snake instability: Possibility of observation in the gaseous Bose–Einstein condensate". In: *Phys. Rev. A* 65 (4), p. 043612 (cit. on pp. 26, 27, 71, 74, 75, 89, 98, 118).

S. Braun, M. Friesdorf, S. S. Hodgman, M. Schreiber, J. P. Ronzheimer, A. Riera, M. del Rey, I. Bloch, J. Eisert, and U. Schneider (2015). "Emergence of coherence and the dynamics of quantum phase transitions". In: *Proc. Natl. Acad. Sci. USA* 112.12, pp. 3641–3646 (cit. on pp. 2, 17).

S. Burger, K. Bongs, S. Dettmer, W. Ertmer, K. Sengstock, A. Sanpera, G. V. Shlyapnikov, and M. Lewenstein (1999). "Dark Solitons in

Bose–Einstein Condensates". In: *Phys. Rev. Lett.* 83 (25), pp. 5198–5201 (cit. on pp. 24, 71, 73).

R. Carmi and E. Polturak (1999). "Search for spontaneous nucleation of magnetic flux during rapid cooling of $YBa_2Cu_3O_{7-\delta}$ films through T_c". In: *Phys. Rev. B* 60.10, p. 7595 (cit. on pp. 2, 16).

R. Carmi, E. Polturak, and G. Koren (2000). "Observation of spontaneous flux generation in a multi-Josephson-junction loop". In: *Phys. Rev. Lett.* 84.21, p. 4966 (cit. on pp. 2, 17).

Y. Castin and R. Dum (1996). "Bose–Einstein Condensates in Time Dependent Traps". In: *Phys. Rev. Lett.* 77 (27), pp. 5315–5319 (cit. on pp. 55, 77, 100).

J. Catani, P. Maioli, L. De Sarlo, F. Minardi, and M. Inguscio (2006). "Intense slow beams of bosonic potassium isotopes". In: *Phys. Rev. A* 73 (3), p. 033415 (cit. on p. 30).

A. Cetoli, J. Brand, R. G. Scott, F. Dalfovo, and L. P. Pitaevskii (2013). "Snake instability of dark solitons in fermionic superfluids". In: *Phys. Rev. A* 88 (4), p. 043639 (cit. on p. 25).

S. Chae, N. Lee, Y. Horibe, M. Tanimura, S. Mori, B. Gao, S. Carr, and S.-W. Cheong (2012). "Direct observation of the proliferation of ferroelectric loop domains and vortex-antivortex pairs". In: *Phys. Rev. Lett.* 108.16, p. 167603 (cit. on pp. 2, 17).

D. Chen, M. White, C. Borries, and B. DeMarco (2011). "Quantum quench of an atomic Mott insulator". In: *Phys. Rev. Lett.* 106 (23), p. 235304 (cit. on pp. 2, 17).

F. Chevy, K. W. Madison, V. Bretin, and J. Dalibard (2001). "Interferometric detection of a single vortex in a dilute Bose–Einstein condensate". In: *Phys. Rev. A* 64 (3), p. 031601 (cit. on pp. 81, 82).

L. Chomaz, L. Corman, T. Bienaimé, R. Desbuquois, C. Weitenberg, S. Nascimbène, J. Beugnon, and J. Dalibard (2015). "Emergence of coherence via transverse condensation in a uniform quasi-two-dimensional Bose gas". In: *Nat. Commun.* 6 (cit. on pp. 2, 14, 62).

I. Chuang, R. Durrer, N. Turok, and B. Yurke (1991). "Cosmology in the Laboratory: Defect Dynamics in Liquid Crystals". In: *Science* 251.4999, pp. 1336–1342 (cit. on pp. 14, 15).

C. Cohen-Tannoudji and D. Guéry-Odelin (2011). *Advances in Atomic Physics*. World Scientific (cit. on pp. 19, 33, 39).

F. Dalfovo, S. Giorgini, L. P. Pitaevskii, and S. Stringari (1999). "Theory of Bose–Einstein condensation in trapped gases". In: *Rev. Mod. Phys.* 71 (3), pp. 463–512 (cit. on p. 21).

K. B. Davis, M. O. Mewes, M. R. Andrews, N. J. van Druten, D. S. Durfee, D. M. Kurn, and W. Ketterle (1995). "Bose–Einstein Condensation in a Gas of Sodium Atoms". In: *Phys. Rev. Lett.* 75 (22), pp. 3969–3973 (cit. on pp. 19, 29).

G. De Rosi and S. Stringari (2015). "Collective oscillations of a trapped quantum gas in low dimensions". In: *Phys. Rev. A* 92.5, p. 053617 (cit. on p. 109).

A. del Campo, T. Kibble, and W. Zurek (2013). "Causality and non-equilibrium second-order phase transitions in inhomogeneous systems". In: *J. Phys.* 25.40, p. 404210 (cit. on pp. 1, 11).

A. del Campo, A. Retzker, and M. B. Plenio (2011). "The inhomogeneous Kibble–Zurek mechanism: vortex nucleation during Bose–Einstein condensation". In: *New J. Phys.* 13.8, p. 083022 (cit. on pp. 2, 11, 55).

A. del Campo and W. H. Zurek (2014). "Universality of phase transition dynamics: Topological defects from symmetry breaking". In: *Int. J. Mod. Phys. A* 29.08, p. 1430018 (cit. on pp. 1, 8, 11, 14, 15, 94).

J. Denschlag, J. E. Simsarian, D. L. Feder, C. W. Clark, L. A. Collins, J. Cubizolles, L. Deng, E. W. Hagley, K. Helmerson, W. P. Reinhardt, S. L. Rolston, B. I. Schneider, and W. D. Phillips (2000). "Generating Solitons by Phase Engineering of a Bose–Einstein Condensate". In: *Science* 287.5450, pp. 97–101 (cit. on pp. 24, 71, 73).

K. Dieckmann, R. J. C. Spreeuw, M. Weidemüller, and J. T. M. Walraven (1998). "Two-dimensional magneto-optical trap as a source of slow atoms". In: *Phys. Rev. A* 58 (5), pp. 3891–3895 (cit. on p. 30).

M. E. Dodd, P. C. Hendry, N. S. Lawson, P. V. E. McClintock, and C. D. H. Williams (1998). "Nonappearance of Vortices in Fast Mechanical Expansions of Liquid ^{4}He through the Lambda Transition". In: *Phys. Rev. Lett.* 81 (17), pp. 3703–3706 (cit. on p. 16).

S. Donadello (2012). "A compact high-flux source of cold sodium atoms". MA thesis. Università degli Studi di Trento (cit. on pp. 31, 48).

S. Donadello, S. Serafini, M. Tylutki, L. P. Pitaevskii, F. Dalfovo, G. Lamporesi, and G. Ferrari (2014). "Observation of Solitonic Vortices in Bose–Einstein Condensates". In: *Phys. Rev. Lett.* 113 (6), p. 065302 (cit. on pp. 3, 27, 72, 75, 93, 98, 112).

T. Donner, S. Ritter, T. Bourdel, A. Öttl, M. Köhl, and T. Esslinger (2007). "Critical behavior of a trapped interacting Bose gas". In: *Science* 315.5818, pp. 1556–1558 (cit. on pp. 14, 62).

S. Ducci, P. L. Ramazza, W. González-Viñas, and F. Arecchi (1999). "Order parameter fragmentation after a symmetry-breaking transition". In: *Phys. Rev. Lett.* 83.25, p. 5210 (cit. on pp. 2, 16).

J. Dziarmaga and W. H. Zurek (2014). "Quench in the 1D Bose–Hubbard model: Topological defects and excitations from the Kosterlitz–Thouless phase transition dynamics". In: *Sci. Rep.* 4 (cit. on p. 8).

U. Ernst, J. Schuster, F. Schreck, A. Marte, A. Kuhn, and G. Rempe (1998). "Free expansion of a Bose–Einstein condensate from an Ioffe–Pritchard magnetic trap". In: *Appl. Phys. B* 67.6, pp. 719–722 (cit. on pp. 55, 77, 100).

D. L. Feder, M. S. Pindzola, L. A. Collins, B. I. Schneider, and C. W. Clark (2000). "Dark-soliton states of Bose–Einstein condensates in anisotropic traps". In: *Phys. Rev. A* 62 (5), p. 053606 (cit. on p. 73).

D. Frantzeskakis (2010). "Dark solitons in atomic Bose–Einstein condensates: from theory to experiments". In: *J. Phys. A* 43.21, p. 213001 (cit. on p. 24).

A. Görlitz, J. Vogels, A. Leanhardt, C. Raman, T. Gustavson, J. Abo-Shaeer, A. Chikkatur, S. Gupta, S. Inouye, T. Rosenband, et al. (2001). "Realization of Bose–Einstein condensates in lower dimensions". In: *Phys. Rev. Lett.* 87.13, p. 130402 (cit. on p. 23).

R. Grimm, M. Weidemüller, and Y. B. Ovchinnikov (2000). "Optical Dipole Traps for Neutral Atoms". In: *Adv. At., Mol., Opt. Phys.* 42, pp. 95–170 (cit. on p. 34).

P. C. Hendry, N. S. Lawson, R. A. M. Lee, P. V. E. McClintock, and C. D. H. Williams (1994). "Generation of defects in superfluid ^{4}He as an analogue of the formation of cosmic strings". In: *Nature* 368, pp. 315–317 (cit. on p. 16).

P. C. Hohenberg and B. I. Halperin (1977). "Theory of dynamic critical phenomena". In: *Rev. Mod. Phys.* 49.3, p. 435 (cit. on pp. 13, 14, 64, 98, 117).

K. Huang (1987). *Statistical mechanics*. Wiley (cit. on p. 5).

S. Inouye, S. Gupta, T. Rosenband, A. P. Chikkatur, A. Görlitz, T. L. Gustavson, A. E. Leanhardt, D. E. Pritchard, and W. Ketterle (2001). "Observation of Vortex Phase Singularities in Bose–Einstein Condensates". In: *Phys. Rev. Lett.* 87 (8), p. 080402 (cit. on p. 81).

A. Jelić and L. F. Cugliandolo (2011). "Quench dynamics of the 2d XY model". In: *J. Stat. Mech. Theor. Exp.* 2011.02, P02032 (cit. on p. 8).

K. Kasamastu and M. Tsubota (2009). "Quantised Vortices in Atomic Bose–Einsten Condensates". In: *Prog. Low Temp. Phys.* 16, pp. 351–403 (cit. on p. 25).

W. Ketterle, K. Davis, M. Joffe, A. Martin, and D. Pritchard (1993). "High densities of cold atoms in a dark spontaneous-force optical trap". In: *Phys. Rev. Lett.* 70.15, pp. 2253–2256 (cit. on p. 36).

W. Ketterle and N. van Druten (1996a). "Evaporative cooling of trapped atoms". In: *Adv. At., Mol., Opt. Phys.* 37, pp. 181–236 (cit. on pp. 38, 65, 103).

W. Ketterle, D. Durfee, and D. Stamper-Kurn (1999). "Making, probing and understanding Bose–Einstein condensates". In: *Proceedings of the International School of Physics "Enrico Fermi"*. Vol. CXL. IOS, pp. 67–176 (cit. on pp. 19, 20, 36, 42, 65, 68, 99).

W. Ketterle and N. Van Druten (1996b). "Bose–Einstein condensation of a finite number of particles trapped in one or three dimensions". In: *Phys. Rev. A* 54.1, p. 656 (cit. on p. 11).

T. W. B. Kibble (1976). "Topology of cosmic domains and strings". In: *J. Phys. A* 9.8, p. 1387 (cit. on pp. 1, 7).

T. W. B. Kibble (2007). "Phase-transition dynamics in the lab and the universe". In: *Physics Today* 60.9, p. 47 (cit. on pp. 2, 14, 18, 55).

J. Kirtley, C. Tsuei, and F. Tafuri (2003). "Thermally activated spontaneous fluxoid formation in superconducting thin film rings". In: *Phys. Rev. Lett.* 90.25, p. 257001 (cit. on pp. 2, 16).

S. Komineas and N. Papanicolaou (2003). "Solitons, solitonic vortices, and vortex rings in a confined Bose–Einstein condensate". In: *Phys. Rev. A* 68 (4), p. 043617 (cit. on pp. 26, 27, 71, 74, 75, 89, 98, 118).

J. M. Kosterlitz and D. J. Thouless (1973). "Ordering, metastability and phase transitions in two-dimensional systems". In: *J. Phys. C* 6.7, p. 1181 (cit. on p. 5).

M. Kozuma, L. Deng, E. W. Hagley, J. Wen, R. Lutwak, K. Helmerson, S. L. Rolston, and W. D. Phillips (1999). "Coherent Splitting of Bose–Einstein Condensed Atoms with Optically Induced Bragg Diffraction". In: *Phys. Rev. Lett.* 82 (5), pp. 871–875 (cit. on p. 81).

M. J. H. Ku, W. Ji, B. Mukherjee, E. Guardado-Sanchez, L. W. Cheuk, T. Yefsah, and M. W. Zwierlein (2014). "Motion of a Solitonic Vortex in the BEC-BCS Crossover". In: *Phys. Rev. Lett.* 113 (6), p. 065301 (cit. on p. 75).

G. Lamporesi, S. Donadello, S. Serafini, and G. Ferrari (2013a). "Compact high-flux source of cold sodium atoms". In: *Rev. Sci. Instrum.* 84.6, p. 063102 (cit. on pp. 3, 31).

G. Lamporesi, S. Donadello, S. Serafini, F. Dalfovo, and G. Ferrari (2013b). "Spontaneous creation of Kibble–Zurek solitons in a Bose–Einstein condensate". In: *Nature Phys.* 9.10, pp. 656–660 (cit. on pp. 3, 19, 27, 55, 61, 64, 72, 73, 91, 93, 94, 97, 98, 106, 108, 112).

P. D. Lett, R. N. Watts, C. I. Westbrook, W. D. Phillips, P. L. Gould, and H. J. Metcalf (1988). "Observation of Atoms Laser Cooled below the Doppler Limit". In: *Phys. Rev. Lett.* 61 (2), pp. 169–172 (cit. on p. 36).

I.-K. Liu, G. Lamporesi, S. Donadello, F. Dalfovo, G. Ferrari, S.-C. Gou, and N. P. Proukakis (2015). "Quenched Solitonic Vortex Generation in Elongated Trapped Bose Gases". In: *FINESS 2015 Book of Abstracts* (cit. on p. 113).

K. W. Madison, F. Chevy, W. Wohlleben, and J. Dalibard (2000). "Vortex Formation in a Stirred Bose–Einstein Condensate". In: *Phys. Rev. Lett.* 84 (5), pp. 806–809 (cit. on p. 26).

A. M. Mateo and J. Brand (2014). "Chladni solitons and the onset of the snaking instability for dark solitons in confined superfluids". In: *Phys. Rev. Lett.* 113.25, p. 255302 (cit. on pp. 27, 28, 89, 98, 118).

M. R. Matthews, B. P. Anderson, P. C. Haljan, D. S. Hall, C. E. Wieman, and E. A. Cornell (1999). "Vortices in a Bose–Einstein Condensate". In: *Phys. Rev. Lett.* 83 (13), pp. 2498–2501 (cit. on p. 26).

R. Monaco, J. Mygind, M. Aaroe, R. J. Rivers, and V. P. Koshelets (2006). "Zurek-Kibble Mechanism for the Spontaneous Vortex For-

mation in Nb-Al/Al_{ox}/Nb Josephson Tunnel Junctions: New Theory and Experiment". In: *Phys. Rev. Lett.* 96 (18), p. 180604 (cit. on pp. 2, 17).

N. Navon, A. L. Gaunt, R. P. Smith, and Z. Hadzibabic (2015). "Critical dynamics of spontaneous symmetry breaking in a homogeneous Bose gas". In: *Science* 347.6218, pp. 167–170 (cit. on pp. 2, 14, 62, 96).

W. D. Phillips and H. Metcalf (1982). "Laser Deceleration of an Atomic Beam". In: *Phys. Rev. Lett.* 48 (9), pp. 596–599 (cit. on p. 30).

L. Pitaevskii and S. Stringari (2016). *Bose–Einstein Condensation and Superfluidity*. Oxford University Press (cit. on pp. 20, 24, 25, 66, 70).

D. E. Pritchard (1983). "Cooling Neutral Atoms in a Magnetic Trap for Precision Spectroscopy". In: *Phys. Rev. Lett.* 51 (15), pp. 1336–1339 (cit. on p. 36).

K. Pyka, J. Keller, H. Partner, R. Nigmatullin, T. Burgermeister, D. Meier, K. Kuhlmann, A. Retzker, M. Plenio, W. Zurek, et al. (2013). "Topological defect formation and spontaneous symmetry breaking in ion Coulomb crystals". In: *Nat. Commun.* 4 (cit. on pp. 2, 17).

L. Ricci, M. Weidemüller, T. Esslinger, A. Hemmerich, C. Zimmermann, V. Vuletic, W. König, and T. W. Hänsch (1995). "A compact grating-stabilized diode laser system for atomic physics". In: *Opt. Commun.* 117.5, pp. 541–549 (cit. on p. 33).

V. M. H. Ruutu, V. B. Eltsov, A. J. Gill, T. W. B. Kibble, M. Krusius, Y. G. Makhlin, B. Placais, G. E. Volovik, and W. Xu (1996). "Vortex formation in neutron-irradiated superfluid ^{3}He as an analogue of cosmological defect formation". In: *Nature* 382.6589, pp. 334–336 (cit. on pp. 1, 16, 17).

L. Sadler, J. Higbie, S. Leslie, M. Vengalattore, and D. Stamper-Kurn (2006). "Spontaneous symmetry breaking in a quenched ferromagnetic spinor Bose–Einstein condensate". In: *Nature* 443.7109, pp. 312–315 (cit. on pp. 2, 17).

S. Serafini (2013). "Realization of a magnetic trap for the production of sodium Bose–Einstein Condensates". MA thesis. Università degli Studi di Trento (cit. on p. 38).

S. Serafini, M. Barbiero, M. Debortoli, S. Donadello, F. Larcher, F. Dalfovo, G. Lamporesi, and G. Ferrari (2015). "Dynamics and interaction of vortex lines in an elongated Bose–Einstein condensate". In: *Phys. Rev. Lett.* 115.17, p. 170402 (cit. on pp. 3, 40, 43, 47, 91, 93, 112, 113, 115, 116).

T. G. Tiecke, S. D. Gensemer, A. Ludewig, and J. T. M. Walraven (2009). "High-flux two-dimensional magneto-optical-trap source for cold lithium atoms". In: *Phys. Rev. A* 80.1, p. 013409 (cit. on p. 30).

A. Toffali (2013). "Production of ultracold Sodium and Potassium atomic mixture in an optical dipole trap". MA thesis. Università degli Studi di Trento (cit. on p. 31).

M. Tylutki, S. Donadello, S. Serafini, L. P. Pitaevskii, F. Dalfovo, G. Lamporesi, and G. Ferrari (2015). "Solitonic vortices in Bose–Einstein condensates". In: *Eur. Phys. J. Special Topics* 224.3, pp. 577–583 (cit. on pp. 3, 27, 75, 84).

S. Ulm, J. Roßnagel, G. Jacob, C. Degünther, S. Dawkins, U. Poschinger, R. Nigmatullin, A. Retzker, M. Plenio, F. Schmidt-Kaler, et al. (2013). "Observation of the Kibble–Zurek scaling law for defect formation in ion crystals". In: *Nat. Commun.* 4 (cit. on pp. 2, 17).

K. M. R. van der Stam, E. D. van Ooijen, R. Meppelink, J. M. Vogels, and P. van der Straten (2007). "Large atom number Bose–Einstein condensate of sodium". In: *Rev. Sci. Instrum.* 78.1, 013102, p. 013102 (cit. on p. 30).

C. N. Weiler, T. W. Neely, D. R. Scherer, A. S. Bradley, M. J. Davis, and B. P. Anderson (2008). "Spontaneous vortices in the formation of Bose–Einstein condensates". In: *Nature* 455, pp. 948–952 (cit. on pp. 2, 18, 26, 55).

T. Yefsah, A. T. Sommer, M. J. H. Ku, L. W. Cheuk, W. Ji, W. S. Bakr, and M. W. Zwierlein (2013). "Heavy solitons in a fermionic superfluid". In: *Nature* 499, p. 426 (cit. on p. 73).

J. Yu, J. Djemaa, P. Nosbaum, and P. Pillet (1994). "Funnel with orientated Cs atoms". In: *Opt. Commun.* 112.3, pp. 136–140 (cit. on p. 30).

W. H. Zurek (1985). "Cosmological experiments in superfluid liquid helium?" In: *Nature* 317, pp. 505–508 (cit. on pp. 1, 7, 14, 15).

W. H. Zurek (2009). "Causality in Condensates: Gray Solitons as Relics of BEC Formation". In: *Phys. Rev. Lett.* 102 (10), p. 105702 (cit. on pp. 2, 11, 13, 55, 57, 64, 66, 89).

W. H. Zurek, U. Dorner, and P. Zoller (2005). "Dynamics of a Quantum Phase Transition". In: *Phys. Rev. Lett.* 95 (10), p. 105701 (cit. on p. 1).